Title
High Fidelity Modeling Techniques for MEMS Resonators

Author
Schein, Stephen George

Publication Date
2023

Peer reviewed|Thesis/dissertation

UNIVERSITY OF CALIFORNIA

Los Angeles

High Fidelity Modeling Techniques for MEMS Resonators

A dissertation submitted in partial satisfaction

of the requirements for the degree

Doctor of Philosophy in Mechanical Engineering

by

Stephen Schein

2023

ABSTRACT OF THE DISSERTATION

High Fidelity Modeling Techniques for MEMS Resonators

by

Stephen Schein
Doctor of Philosophy in Mechanical Engineering
University of California, Los Angeles, 2023
Professor Robert T. M'Closkey, Chair

Prior resonator research is first over-viewed. Galerkin analysis applied to a perturbed thin ring yields intuition and motivation for the primary contributions, described below.

The first contribution is a fully fleshed novel method to derive the empirical frequency response by extracting a state space model from transient data through a Hankel matrix based approach. This method has the advantage of not containing feed-through parasitic capacitance present in frequency responses derived from conventional methods. Furthermore, a zoom method is described to reduce the computational cost associated with extracting the state space based model.

The second contribution is the use of the aforementioned empirical state space model to fit a second order mechanistic model that accurately predicts changes in resonator dynamics after a mass and/or stiffness perturbation has been applied. This model is a better alternative to older predictive models because it includes a stiffness energy component. In addition, this new model gives the added tool of a predictive system frequency response, which conventional models do not have. In general it is found that, especially as the modes are close to degenerate, using lower sensitivity point masses in the outermost ring layers

optimizes the predictive power of the new model. Furthermore, predicting for the effects of as few point masses as possible limits the model due to point mass variance and higher harmonic radial velocity components creating model prediction error.

The third contribution is in the design, building, and testing of a stiff, piezoelectric six degree of freedom force/torque transducer to measure and inform modeling techniques for coupling between a resonator and its base affixed center stem. A simple lightweight steel tuning fork attached to this transducer confirms the latter's efficacy.

The dissertation of Stephen Schein is approved.

Lieven Vandenberghe

T.C. Tsao

Tetsuya Iwasaki

Robert T. M'Closkey, Committee Chair

University of California, Los Angeles

2023

TABLE OF CONTENTS

List of Figures

List of Tables

ACKNOWLEDGMENTS

Foremost, I want to acknowledge my advisor Professor Robert M'Closkey for the continuous support of my research throughout the many years of my PhD tenure. His personability, genuine excitement for reasearch, and immense knowledge helped motivate me day in and day out. I am extremely grateful that Professor M'Closkey helped me flourish not only as a student and researcher, but also as a human being who strives to make a positive mark on the world, and no one knows the meaning of that more than him.

Besides my advisor, I would like to thank the rest of my thesis committee: Professor T.C. Tsao, Professor Tetsuya Iwasaki, and Professor Lieven Vandenberghe, for their support and insightful comments. I would like to thank other instructors and professors who made a notable impact during my time at UCLA, Dr. Vinay Goyal, Dr. Robert Kinsey, and Dr. Stephen Gibson. I am also grateful to the following university staff: Evgenia Grigorova, Benjamin Tan, Abel Lebon, Lance Kono, Marla Cooper, Amanda Gordillo, and Collin Llewellyn.

I want to express my thanks to the Mechanical and Aerospace Engineering department for the opportunity of being a Teaching Assistant for all my students in MAE 107 over the many quarters I had the chance to educate the next generation of engineers. The students always pushed me to be a better teacher and strengthened my love for teaching.

I want to note my supportive group of UCLA friends, built through the great efforts of Dr. Vinay Goyal, while also teaching MAE 261A: Elmer Wu, Abdiel Agramonte-Moreno, Fadhel AlSaffar, Rohan Shah, Yiran Tong, and Troy Story. I would also like to mention my friends in the UCLA EPRL that I was fortunate in becoming close with over the course of graduate school: Dr. Stephen Samples, Dr. Ani Thuppul, Dr. Peter Wright, McKenna Davis, Angelica Ottaviano, Mary Konopliv, Patrick Crandall, Dr. Adam Collins, and Dr. Gary Wan.

I also want to express my gratitude for all of the support that Dr. Ann Karagozian has given, along with her current and former lab members: Dr. Takeshi Shoji, Dr. Andrea Besnard, Dr. Elijah Harris, Dr. Miguel Plascencia, Dr. Andres Vargas, and David Ren for

giving me the opportunity to collaborate on and contribute to transverse jet experiments, and for providing financial support during summer quarters.

I also want to express my sincere gratitude for my current and past lab-mates: Dr. Amir Behbahani, Dr. Howard Ge, Dr. Michael Andonian, Kenny Pyle, David Hill, and Alessandro Bullita for creating the best work environment. They were the most supportive group I could ever hope for.

I want to briefly note my friends from Harvey Mudd College: Ryan Jones, you've taught me what it means to truly be a good teacher. Avi Thaker, you've given me confidence in myself as an academic that I didn't think I had through your belief in me. Caleb Eades, you helped me realize that success comes through hard work, preparation, and having the right mindset. Dr. Alec Dunton, you kept me going through this PhD process. There were times when I didn't know I had it in me, but you convinced me that I could really do it. Dr. Daryl Yong, your mentorship and unending support always helped me forward.

Finally, and most importantly, I want to thank my family: my mother Marikay Schein, my father Dr. David Schein, and my sisters Diana Hill and Victoria Lewis. My parents have always been supportive and have given me the opportunity to follow my passion, whatever it ended up being. During my time as a graduate student, their guidance helped me to persevere and build myself up through rough times, while also being able to appreciate successes. From the time we were all born together, my sisters have always been active in my life, have been the most supportive of my endeavors, and have been my closest friends. And so, I proudly dedicate this thesis to my family.

VITA

2012	B.S. (Engineering), Harvey Mudd College, Claremont, CA.
2012	B.S. (Mathematics), Harvey Mudd College, Claremont, CA.
2016-2023	Graduate Research Assistant, Mechanical and Aerospace Engineering Department, Dynamic Systems and Control Design Lab & Energy and Propulsion Research Lab, UCLA, Los Angeles, CA
2018-2022	Teaching Assistant, Mechanical and Aerospace Engineering Department, UCLA. MAE 107: Introduction to Modeling and Analysis of Dynamic Systems (12 times).
2019	M.S. (Mechanical Engineering), UCLA, Los Angeles, CA.

PUBLICATIONS AND PRESENTATIONS

E.W. Harris, S. Schein, D. Ren, A.R. Karagozian. Synchronization and dynamics of the axisymmetrically excited jet in crossflow. 2023

E.W. Harris, T. Shoji, A. Besnard, S. Schein, A.R. Karagozian, L. Coretellezi, R.T. M'Closkey. Effects of controlled vortex generation and interactions in transverse jets. Physical Review Fluids. 2022.

S. Schein, R.T. M'Closkey. Parametric Model Identification of Axisymmetric MEMS Resonators. 2021.

T. Shoji, E.W. Harris, A. Besnard, S. Schein, A.R. Karagozian. On the origins of tranverse jet shear layer instability transition. Journal of Fluid Mechanics. 2020.

T. Shoji, E.W. Harris, A. Besnard, S. Schein, A.R. Karagozian. Transverse jet lock-in and quasiperiodicity. Physical Review Fluids. 2020.

A. Besnard, T. Shoji, S. Schein, E.W. Harris, A.R. Karagozian. Exploration of Asymmetric Forcing on Mixing and Structural Characteristics for Transverse Jets. AIAA Scitech 2019 Forum. 2019.

S. Schein, T. Shoji, A. Karagozian, R. M'Closkey. An adaptive control process for the temporal shaping of a jet in cross flow. 70th APS DFD Meeting. 2017.

CHAPTER 1

Prior Research and Overview

Many different resonators configurations have been studied, including quadruple mass resonators [TPZ11] and hemispherical ([BBC13], [SMG14], [PZT11], [ZTS12], [KBK15], [TSH14]). [CGL14] shows the development of the disk resonator that shifts most of the pertinent work on resonators, and thus the focus of recent work and this current work is on ring-like disk resonator gyroscopes (DRGs).

For sensor application, there are a few important tests for quantifying rate sensor performance such as DRGs. The angle random walk (ARW) is a specification that shows the error of the sensor when angular rate is integrated. Bias instability is a specification that tell how much drift the sensor has from its mean output rate. Both can be measured via Allen Variance tests. From a long sequence of angular rate gyro measurements, the data is binned appropriately as a function of different sampling times, and the variance is calculated on a sample to sample basis. The deviation (square root of variance) is then plotted against the sampling times, and the minimum deviation is extracted as the bias instability. ARW is extracted by looking at the Allen Deviation at a sampling time of 1 s. This measurement is taken at the 1 s. sampling time because the error can then be extracted by multiplying the ARW by $\sqrt{t}$. These will not be touched upon in this current work but are vital in the use of the resonator as an angular rate sensor.

It is of great importance to remove frequency imbalances in a resonator to improve the signal to noise ratio (SNR) in the vibratory mode of interest. A high SNR for a particular mode implies a low ARW and low bias instability giving higher resonator performance.

[TLI13] showed that a tuned resonator can then be used to effectively measure angular rate. These gyroscopic sensors are used specifically in areas with clear need for accurate measurements of angular rate, such as for mobile phone, automotive, robotics and spacecraft uses [App84]. The work throughout this prospectus then focuses on effectively modeling the resonator dynamics and tuning the sensor.

This chapter summarizes prior relevant, foundational thin ring theory, the production and testing of the vibratory DRG (at both the micro and macro scale), discusses the pertinent prior research primarily concerning the modeling and modal pair tuning of ring-like resonators, and finally overviews the current work.

1.1 Prior Relevant Analytical Thin Ring Results

This section lays the groundwork for the analytical models studied thus far, extending from thin rings to ring-like DRGs. [Fox90] derives a theoretical framework for the study of frequency splitting in thin rings, relevant due to the resonators studied consistent of a series of concentric thin rings interconnected. To summarize, the equations relevant to a uniform thin ring with degenerate modes are derived for "mode n" with n modal diameters by defining a displacement ratio between the sinusoidal radial and tangential displacements. The max strain and kinetic energies are then formulated, and the Rayleigh-Ritz method is applied by setting the second derivative of natural frequency with respect to the displacement ratio equal to zero, from there backing out uniform ring modal equations.

Imperfect thin rings can then considered via the addition of small masses and radial or torsional springs. The effect of each type of perturbation is first independently analyzed in terms of the effect on kinetic and strain energies. The imperfect ring modal equations are then derived again via the use of the Rayleigh-Ritz method. With the general equations derived, specific cases of the single mass, single radial spring, and single torsional spring perturbations are observed. Finally, the single mode "trimming" or "tuning" problem, where

multiple masses are added to the uniform thin ring, is analyzed. [RMF01] takes this theory further to studying the trimming problem for multiple modes simultaneously. [BM17] then performs a perturbation analysis of the uniform ring when point masses and springs are introduced and compares these results to the former Rayleigh-Ritz analysis. The current work is motivated by obtaining a mechanical model parameters for "mode n" in thin rings, i.e. mass and stiffness matrices. The Galerkin method is the ideal numerical method for this purpose, applied to imperfect thin rings in Chapter 2.

1.2 Production and Testing of the MEM-DRG

The silicon MEM-DRG consists of etched concentric thin rings that are linked through alternating spokes to a central fixed disk. Electrodes surrounding the resonator can be used as input forcers and output vibration sensors by taking advantage of the small capacitive gaps between the two. This resonator has features that are generic to modally degenerate resonators commonly proposed for MEMS Coriolis vibratory gyroscopes. Details on its design, fabrication, and modal properties are given in [SKS15] and [CGL14]. Of interest are the changes to the radial displacement $U(\theta, t)$ as the resonator is actuated.

Figure 1.1 illustrates this configuration. 8 sense electrodes (S_1-S_8) are used as pick-off channels well spaced from one another to get a relatively complete sense of the resonator mode shapes. The pick-off electrodes are denoted S_1 through S_8 and the input electrodes are denoted D_1 and D_2 in Fig. 1.1. D_1 and D_2 are used to excite the $n = 2$ modes, the vibratory mode of interest in this research, as they are orthogonal from the perspective of that mode.

Differences between resonator configurations seen in [BKS17], [SKS15], and for [BM19] as well as this work are described. The axisymmetry of the resonator imparts modal degeneracy to the $n = 1, 2, 3$ pairs of modes where the "n^{th}" pair indicates the two modes whose radial displacements are expressed to first order as $\alpha \cos n\theta + \beta \sin n\theta$, for some α, β, where θ is the angle parameter in the figure. COMSOL renditions of a single mode sans electrodes in the

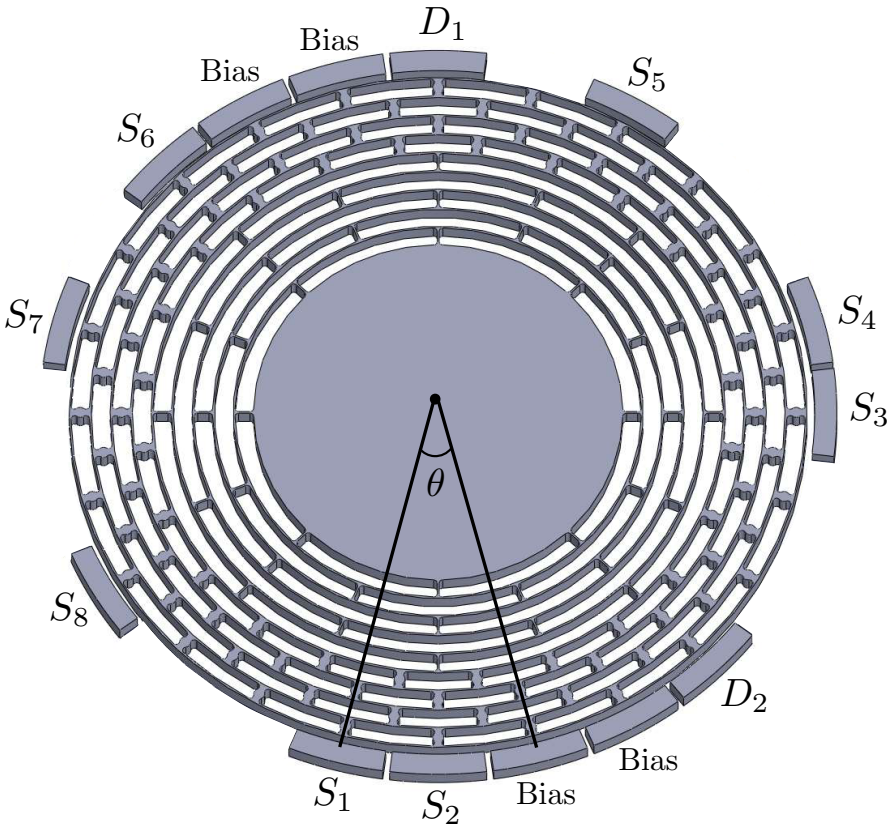

Figure 1.1: Ring resonator used in tests. The resonator is 1 cm in diameter with 24 peripheral electrodes (only those electrodes used in the tests are shown). Two electrodes, denoted D_1 and D_2, are configured as input channels, and eight electrodes, denoted S_1 through S_8, are configured as pickoffs. The electrodes labeled "Bias" are used to perturb the resonator dynamics by applying a potential V_{bias} relative to the resonator bias voltage. Unused electrodes (not shown) are grounded.

$n = 1, 2, 3$ pair of modes is seen in Figure 1.2 below.

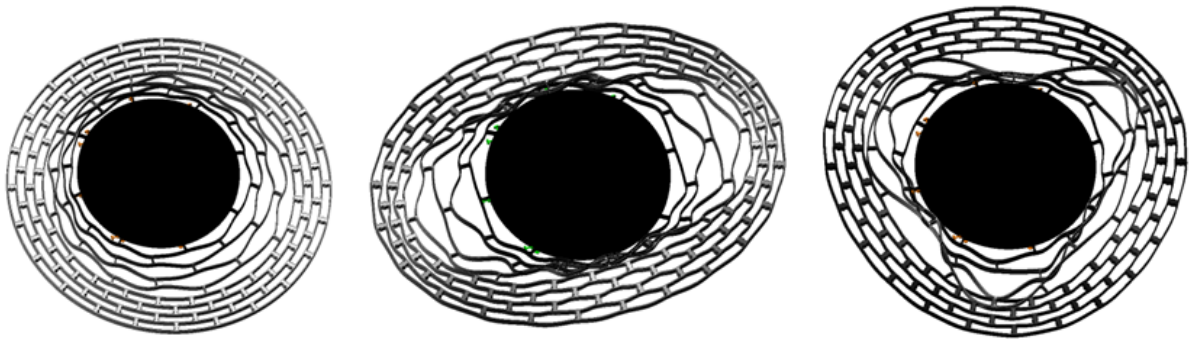

$n = 1$ $n = 2$ $n = 3$

Figure 1.2: A single mode for the $n = 1$ (left), $n = 2$ (middle), and $n = 3$ (right) pairs of modes in the MEM-DRG is shown. Displacements are exaggerated to highlight the mode-shapes.

Although the *relative* orientation of the modes within the n^{th} pair very closely subtend $90°/n$ for ring-type resonators [Fox90], their absolute orientations with respect to the excitation and pick-off electrodes are not known *a-priori*. Thus, multiple inputs and pick-offs are generally required to guarantee coupling to each mode with the relative orientation of the modes dictating the optimal electrode arrangement. The excitation electrode arrangement in Fig. 1.1 is ideal for exciting the $n = 2$ pair, however, these electrodes also collectively couple to the $n = 1, 3$ pairs. The pick-off electrode arrangement has enough spatial resolution to accurately determine the orientation of the modes in addition to not only (collectively) also detecting each mode in the $n = 1, 2, 3$ pairs.

The frequency response derived from a broadband stimulus of the resonator is shown in Fig. 1.3 and serves to illustrate the general location of the $n = 1, 2, 3$ pairs of modes near 6 kHz, 13.5 kHz and 24 kHz, respectively.

A potential, denoted V_{bias}, is applied to the "Bias" electrodes to perturb the dynamics of the resonator in certain experiments. The resonator is tested in a vacuum bell jar at an approximate pressure of 100 μTorr. There is no thermal regulation of the resonator. Some heating of the resonator occurs because the electrode buffer board is collocated with the resonator inside the vacuum chamber. A thirty minute warm-up period is allotted for the pressure and temperature to roughly stabilize. The resonator die is suspended from wire bonds which are attached to the buffer board and to the die's bond pads.

For the resonator in [SKS15], the outer layers of spokes have reservoirs for even finer tuning with silver ink. These resonators weren't used for the present studies due to the desire to explore the full range of point mass perturbations at all points of contact on the resonator. In [BKS17], there were no gold film disks, and resonator tuning was accomplished via etching to remove instead of add mass.

The present resonators, used to highlight the system identification method in Chapter 3, have a 1 μm thick, 130 μm diameter gold film disk deposited in all 96 "spoke" areas on the outer 4 ring layers. These are then targets for leaded and unleaded solder spheres of 75 and

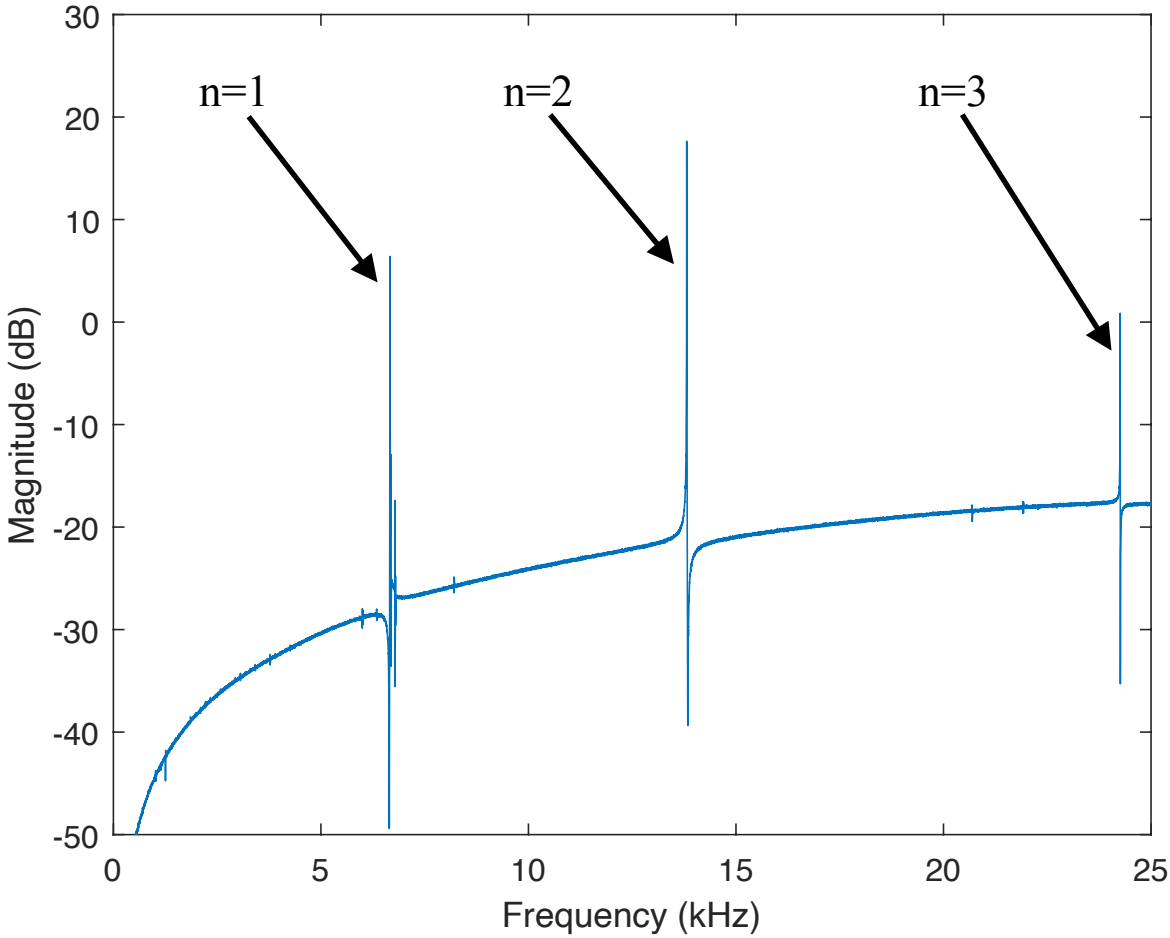

Figure 1.3: Broadband frequency response of the resonator obtained from one stimulus-pick-off electrode pair. The $n = 1, 2, 3$ pairs of modes are evident.

35 μm respectively used for the studies described in Chapter 4.

1.3 Unit Conversion for Resonator Pick-off Measurements

To get a realistic resonator electrode displacement instead of just using the raw voltage output, consider the model below for the circuit associated with electrode measurement resonator motion, with two Op-Amp buffer systems to help clean the signal up, a trans-impedance amplifier (TIA) followed by a low pass inverting amplifier. The input voltage is

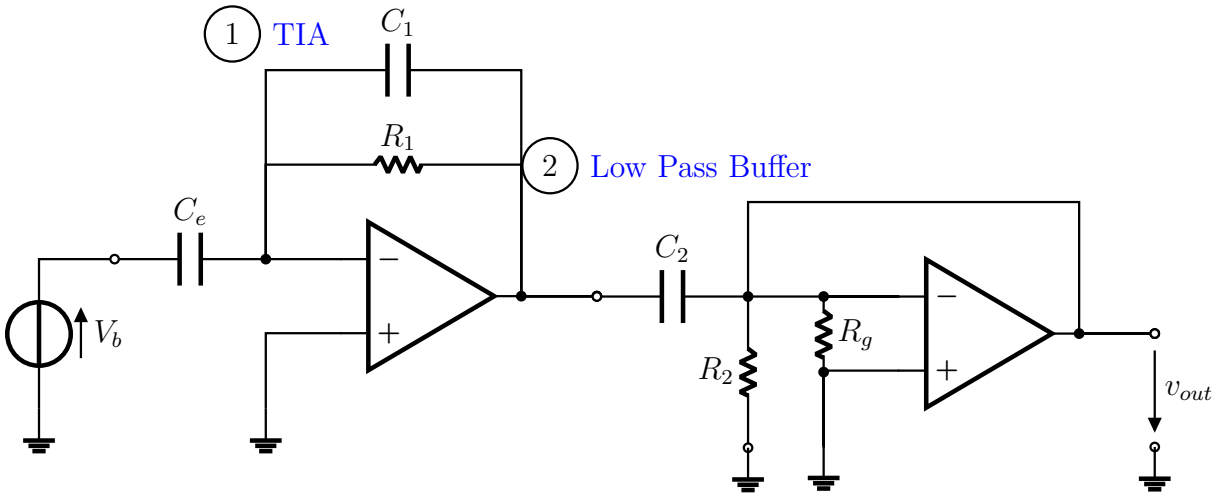

Figure 1.4: Op amp buffer network for sense/pick-off from resonator electrode. Capacitor C_e models the small oscillating gap electrode well. Resulting current with constant bias voltage yields an output voltage after moving through a trans-impedance amplifier and low pass buffer op amp circuit. Since V_{out} is measured, one can backtrack to approximate the electrode gap displacement as a function of frequency.

constant, i.e. $V_b = 50\ V$, $C_1 = 0.5\ pF$, $R_1 = 10\ M\Omega$, $C_2 = 1\ \mu F$, and $R_2 = 1\ k\Omega$. The capacitor C_e is a simple model of the measurement electrode, and has a sinusoidal varying gap, i.e. $C_e = \frac{\epsilon_0 A}{d_0 + d_g \cos(\omega t)}$, where the area is calculated assuming there are 24 electrodes surrounding the $\approx 1\ cm$ diameter resonator with thickness of 430 μm, or $A = 5.87 \times 10^{-7}\ m^2$, $\epsilon_0 = 8.854 \times 10^{-12}\ F/m$, $d_0 = 25\ \mu m$, and d_g is desired as a function of frequency.

As a first step, assume that $d_g << d_0$. Then $C_e \approx \frac{\epsilon_0 A}{d_0}(1 - \frac{d_g}{d_0} cos(\omega t))$. To determine the overall transfer function for the system, we have to consider the current through the TIA, denoted i_e. Since V_b is constant, $i_e = V_b \dot{C_e} = |i_e| \sin(\omega t) = \frac{V_b \epsilon_0 A}{d_0}(\frac{d_g}{d_0} \sin(\omega t))$. If we are interested in purely the magnitude of d_g, then $|d_g| = \frac{|i_e| d_0^2}{V_b \epsilon_0 A}$. The linearized current which is directly proportional to the electrode gap is treated at the input to the op amp system, with

the output being the measured voltage from the second op amp, V_{out} and V_{in} is the input signal sent to the resonator.

$$V_{out}(s)/i_e(s) = V_{out}(s)/V_{in}(s)/i_e(s)/V_{in}(s) = H(s) = \frac{R_1}{1+R_1C_1s}\frac{GR_2C_2s}{1+R_2C_2s},$$

where $R_g = 18.3\ k\Omega$, and so based on the op-amp used, $G = \frac{49.4k\Omega}{R_g} + 1 = 3.7$. From here it is straightforward to back out a frequency response for i_e/V_{in} and then, based on the scaling between i_e and d_g. To be clear,

$$d_g(j\omega)/V_{in}(j\omega) = \frac{d_0^2}{V_b\epsilon_0 A}\frac{1}{H(j\omega)}\underbrace{(V_{out}(j\omega)/V_{in}(j\omega))}_{measured}.$$

1.4 Prior Results on the DRG

This section lays out the groundwork made for the current research via prior pertinent work with various DRGs, mostly focused on work with micro-electro-mechanical disk resonator gyroscopes (MEM-DRGs) in the M'Closkey group. Methods to tune modal frequencies in the disk resonator include electrostatic tuning biases via specific electrodes which perturb the strain energy of the vibratory mode as well as adding or removing mass to perturb the kinetic energy of the mode. Specifically most of these results focus on tuning the $n = 2$ mode. This is the most common mode exploited in axisymmetric vibratory gyros. The resonator is typically mounted to a substrate, so the $n = 1$ mode is harder to measure. The higher modes are typically weaker in SNR and are also thus more difficult to measure and model effectively, however, the $n = 3$ modes are applicable to gyro use when two independent gyro angular rate measurements are desired.

A systematic method in [KM06] achieves electrostatic tuning in the $n = 2$ modes, at roughly 15 kHz, of a JPL-Boeing MEM-DRG. [ABS98], [YM96], [PHA03], [LC97], and [CFH94] also use electrostatic biases to tune resonators. The advantage to this tuning pro-

cess is in its real time nature. These tuning biases, allocated to specific electrodes, can be set to a desired value during testing. The system contains two orthogonal forcers and two sense channels that are antipodal to each of the forcers, as well as two orthogonal electrostatic bias tuning electrodes.

Empirical frequency responses are then measured for each input-output pairing, and a two degree of freedom mass-spring-damper model is assumed for the system localized to the $n = 2$ mode, where the damping contains a Coriolis coupling. This gives rise to constrained positive definite mass, spring, and damper matrices to fit the empirical frequency response data. In essence, the least squares error between the model and empirical frequency responses are minimized to fit the model parameters. Between experiments, the stiffness matrices are assumed to be the parameters that are adjusted as electrostatic biases are introduced. To tune the system, constant weights on the stiffness matrices, comprising the perturbations in stiffness due to each electrostatic bias electrode, are found such that the generalized eigenvalues between the stiffness matrix (with perturbations from the bias voltage electrodes) and mass matrix are equal. The results are limited in the sense that there were only two sense channels used for parameter fitting.

Electrostatic tuning of the resonant modes in real time is effective, however, it places strict requirement on the bias voltage stability used in tuning. This stability must be maintained over the operating environment, specifically due to potential and likely temperature variations. The important analytical contributions from this paper are related to the modeling procedure. Other important research then focuses on tuning resonator vibratory modes with permanent addition/removal of mass.

In [SKM09] tuning masses are applied on a Macro-DRG (roughly 12 mm in diameter) with the $n = 2$ modal frequencies centered at around 1.6 kHz. As seen in [KM06], the system is also 2 input/2 output and empirical frequency responses are fit to mass, stiffness, and damping matrices for each experiment. Each consists of measuring the empirical frequency responses in the nominal or perturbed cases (for various configurations of mass perturba-

tions). Assuming the applied mass perturbation is constant, via usage of a consistent magnet as a mass, mass perturbation matrices (denoted dM or Δ_M) are found experimentally as a function of position of the placed mass (θ). Optimal scaling factors on Δ_M matrices at two tuning positions are found by setting the generalized eigenvalues of the perturbed mass matrix (nominal plus the two scaled Δ_M matrices) and the stiffness matrix to be the same. This study is limited as well by its use of only the mass perturbation of the outermost ring on the resonator and in its use of one consistent magnetic mass for tuning, i.e. the mass perturbations are quantized, for only two tuning locations. The models used in the prior two works are referred to as the "mass matrix" or mechanistic model. Work going forward before the current studies deviate from this model to a simpler one more easily tuned for tuning.

In [SKS15], the n=2 modes located near 14 kHz (Q=50) for five MEM-DRGs are able to be tuned to within 80 mHz from a max frequency mismatch of 30 Hz via mass deposition. In terms of the electrodes, increasing the surface area will increase the capacitive effectiveness of the sensing or forcing. Thus, each I/O channel is a combination of 3 adjacent electrodes combined into a single electrode. The centroid of the two pick off channels, S_1 and S_2 subtend 45°, and the combined single electrodes that are D_1 and D_2 are antipodal to their respective sense channels. The trade off as mentioned earlier is that this method limits the degree of $n = 2$ mode shape able to be observed. Related to this work are the improvements that tuned resonators have on force-to-rebalance operation and angle random walks, shown in [KM14]. In [BM17] etching paper, wafer level etching is applied to systematically eliminate resonator frequency differences. Seven resonators on a wafer are tuned to below 100 mHz frequency difference in the $n = 2$ mode via selective ablation. The work done in [BM19] is the most recent work on the tuning of the MEM-DRG. The work outlines a method to simultaneously tune frequency differences in the $n = 2$ and $n = 3$ vibratory modes. Having two pairs of tuned modes gives two independent angular rate measurements. The result of this work is shown on two resonators. Both vibratory modes are tuned to below 200 mHz

from splits in the natural frequencies starting from 5-25 Hz. Once tuned, the $n = 2$ mode vibrates at 13.5 kHz and the $n = 3$ mode operates at 24 kHz. Section 4.3 expands on the kinetic energy only model used to predictively tune the resonators in these three studies in more detail and motivates the need for a revised model used in the present studies, inspired by the mechanistic or "mass matrix" models used in earlier papers.

1.5 Overview of Present Work

Chapter 2 lays the groundwork for primary contributions by analyzing the effect of width and mass perturbations on thin rings. Specifically, the analysis highlights the effect on a thin ring's vibratory modes and center of mass to linear order of perturbation. Chapter 3 details a novel method to deriving empirical frequency responses through means of extracting a state space model from resonator ring-down data. The state space models accurately show (potentially small) changes in the system due to mass/stiffness perturbations. For the system at hand, analysis is shown to prove that two spatially separated inputs are required to extract a balanced and modal coordinate model. These models are used in the Chapter 4 as empirical models because the error between the acquired transient data and the identified state space models is just the system noise. Chapter 4 then details the use of an updated model to more accurately predict sensor dynamics after a mass or stiffness perturbation is applied. This work derives analytical results pertinent to the new model and discusses experimental prediction results given this new model. Chapter 5 describes the design and calibration of a force/torque transducer to measure center stem coupling in resonators at the macro-scale motivated by measurements taken with the MEM-DRG. Results are presented that confirm the measurement efficacy of this transducer, and point mass perturbations are applied to two separately tested resonators mounted on the transducer in order to reduce the stem coupling: (1) a lightweight steel tuning fork with its tuning fork mode at ≈ 400 Hz and (2) a steel Macro-DRG with $n = 2$ modes at ≈ 1.6 kHz.

CHAPTER 2

Galerkin Analysis of Thin Rings

2.1 Introduction

Due to the ring resonator gyroscope being comprised of connected thin rings, the natural place to begin with analyzing the sensor is with a single thin ring. The figure below shows a uniform thin ring, which is the starting point for any such analysis.

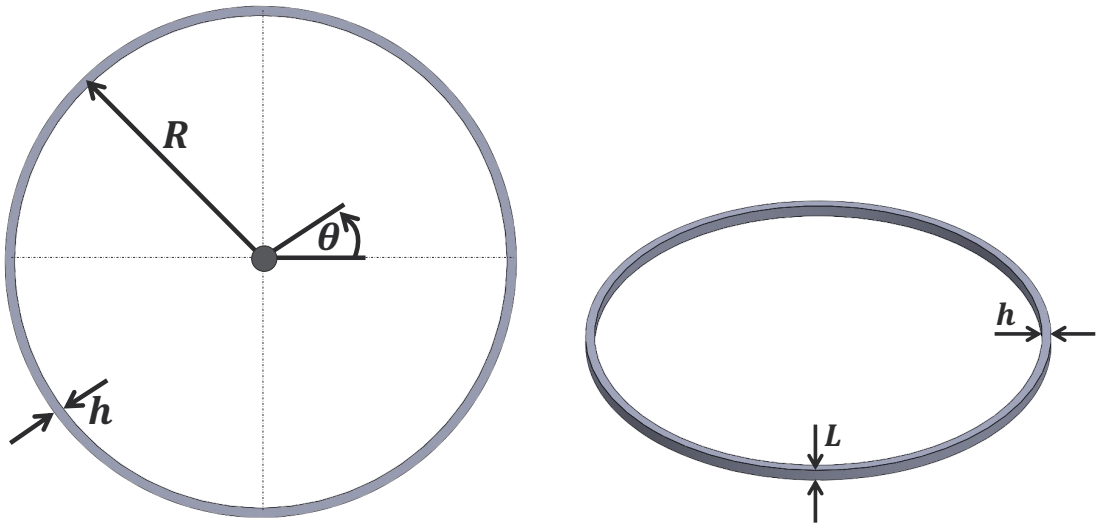

Figure 2.1: A uniform thin ring is shown in top (left) and isometric (right) views. The center of mass is highlighted, and is located at the ring center. Dashed lines fix a coordinate frame with the right hand side at 0°. Any perturbation analyzed is either a point mass or width perturbation applied to this uniform thin ring. The angular coordinate θ along the ring, the ring height L, the ring width h, and the ring radius R are depicted.

This chapter derives and highlights key results from the analysis of an imperfect thin ring, i.e. a uniform ring with mass and/or stiffness perturbations. The weak Galerkin method is used on a linear PDE describing thin ring vibration to gain key insights into the perturbations

to modal properties and to ring center of mass first generally and then focused on each vibrational mode in the $n = 2$ mode pair.

2.2 Galerkin Analysis for a thin ring

The equation of motion for a thin in-extensible ring with variable width takes the following form for the tangential displacement of a thin ring, denoted w:

$$R_m(\ddot{w}(\theta,t), h(\theta), \rho(\theta)) + R_s(w(\theta,t), h(\theta), \rho(\theta)) = 0,$$

where

$$\begin{aligned} R_m &= -\rho h L R \ddot{w} + \rho_{,\theta} h L R \ddot{w}_{,\theta} + \rho h_{,\theta} L R \ddot{w}_{,\theta} + \rho h L R \ddot{w}_{,2\theta} \\ R_s &= +\kappa\Big(w_{,\theta} + w_{,3\theta}\Big) g_{,3\theta} + 3\kappa\Big(w_{,2\theta} + w_{,4\theta}\Big) g_{,2\theta} \\ &\quad + \kappa\Big(w_{,\theta} + 4w_{,3\theta} + 3w_{,5\theta}\Big) g_{,\theta} + \kappa\Big(w_{,2\theta} + 2w_{,4\theta} + w_{,6\theta}\Big) g \end{aligned}$$

$g(\theta) := h^3$, $\kappa = \frac{EL}{12a^3}$, and $(\cdot)_{,n\theta}$ denotes the nth partial with respect to θ, as seen in [Beh18].

Thermoelastic damping is assumed to be negligible to simplify the analysis. Galerkin analysis of (2.2) can be used to estimate mass and stiffness matrices for the nth pair of modes, where the following basis functions are used:

$$f_1(\theta) = \cos(n\theta) \tag{2.1}$$

$$f_2(\theta) = \sin(n\theta) \tag{2.2}$$

$-u_{,\theta}(\theta,t) = w(\theta,t)$, and thus trial solutions for the θ component of the tangential *and radial*

displacements from earlier can be written as

$$W(\theta,t) = x_1(t)f_1(\theta) + x_2(t)f_2(\theta) \tag{2.3}$$

$$U(\theta,t) = x_2(t)f_1(\theta) - x_1(t)f_2(\theta) \tag{2.4}$$

2.2.1 Obtaining mass and stiffness matrices via Galerkin Analysis

Analysis with these basis functions yields the following oscillator model:

$$(M+\Delta_M)\ddot{x} + (K+\Delta_K)x = 0, \quad x(t) = \begin{bmatrix} x_1 & x_2 \end{bmatrix}^T, \tag{2.5}$$

Alternatively, and for sake of brevity, assume $x_1 = B_1 e^{j\omega t}, x_2 = B_2 e^{j\omega t}$, representing the frequency dependent amplitudes attached to the θ component in the tangential and radial displacements. These are then the components used in the Galerkin analysis.

The system of integral equations for the unknown constant basis weights B_1, B_2 are obtained from

$$\int_0^{2\pi} (R_m + R_s) f_1(\theta) d\theta = 0$$
$$\int_0^{2\pi} (R_m + R_s) f_2(\theta) d\theta = 0,$$

yielding a generalized eigenvalue equation that is obtained from these residual integral equations and are gathered as $(\mathcal{R}_m + \mathcal{R}_s)\mathbf{b} = 0$. $\mathbf{b}$ represents the vector of unknown basis function weights, i.e. $\mathbf{b} = \begin{bmatrix} B_1 & B_2 \end{bmatrix}^T$, corresponding to the the unknown amplitudes of the nth pair of vibrational modes. The residuals can be decomposed into mass and stiffness matrices, or $(\mathcal{R}_m + \mathcal{R}_s)\mathbf{b} = (-\mathcal{M}\omega^2 + \mathcal{K})\mathbf{b} = 0$,where $\mathcal{M} = M + \Delta_M$, and $\mathcal{K} = K + \Delta_K$.

The Galerkin method proceeds to obtain desired solution to the ring equation of motion as follows:

1. For R_m, substitute the radial displacement $U(\theta, t)$ appropriately as the de-facto solution because of the known relationship between W and U.

2. Integrate the resultant with respect to each basis function, denoted $\mathcal{R}_{1m}, \mathcal{R}_{2m}$.

3. The terms attached to B_1, B_2 for the resultant $\mathcal{R}_m$ makes up a scaled version of the total mass matrix, denoted $\mathcal{M}$.

4. Repeat the process for R_s to back out the total stiffness matrix, denoted $\mathcal{K}$.

There are allowed two mass perturbations and one width perturbation to capture the effect of one mass perturbation added to the nominal non-degenerate state in a thin ring, modeled with an aggregate small mass and stiffness perturbation.

The mass perturbation is added in the density term, and the stiffness perturbation is defined in terms of the ring width as

$$h(\theta) = h_0(1 + \epsilon_h \cos(p(\theta - \Psi_h)), \tag{2.6}$$

$$\rho(\theta) = \rho_0(1 + 2\pi(\epsilon_{m_1}\delta(\theta - \Psi_1) + \epsilon_{m_2}\delta(\theta - \Psi_2))). \tag{2.7}$$

Figure 2.2 highlights an example of a 1θ width perturbation with two point mass perturbations to help visualize Ψ_h, Ψ_1, and Ψ_2 relative to width and point mass perturbations to a thin ring.

Applying the Galerkin procedure after plugging in the perturbed h and ρ terms to the full differential equation yields mass and stiffness matrices with appropriate perturbed matrices. Isolating the $O(\epsilon)$ terms yields a first order approximation for Δ_M and Δ_K. Let $\Gamma =$

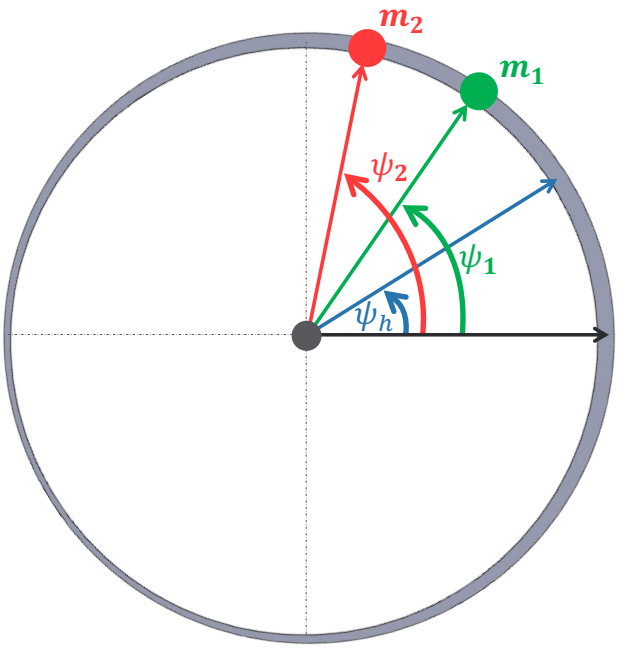

Figure 2.2: Imperfect ring with 1θ width perturbation with maximum thickness at $\theta = \psi_h$. $\theta = \Psi_1$ and $\theta = \Psi_2$ localize two point masses, denoted m_1 and m_2, with "weights" proportional to ϵ_{m_1} and ϵ_{m_2} respectively.

$nRh_0L\pi\rho_0$. Then,

$$\Delta_M = \Delta_{M_{m_1}} + \Delta_{M_{m_2}} + \Delta_{M_h},$$

$$\Delta_{M_{m_i}} = \frac{\Gamma\epsilon_{m_i}}{2n}[(n^2+1)I + (n^2-1)C(\Psi_i, n)], \quad i = 1, 2$$

$$\Delta_{M_h} = \begin{cases} \frac{\Gamma\epsilon_h(n^2-1)}{2n}C(\Psi_h, n) & p = 2n \\ 0 & p \neq 2n \end{cases},$$

$$\Delta_K = \begin{cases} \frac{3}{4}\epsilon_h n^2(n^2-1)^2\pi\kappa h_0^3 S(\Psi_h, n) & p = 2n \\ 0 & p \neq 2n \end{cases},$$

where $I \in \mathbb{R}$ is the identity matrix, and where

$$C(\theta, n) = \begin{bmatrix} \cos(2n\theta) & \sin(2n\theta) \\ \sin(2n\theta) & -\cos(2n\theta) \end{bmatrix},$$
$$S(\theta, n) = \begin{bmatrix} \sin(2n\theta_x) & \cos(2n\theta) \\ \cos(2n\theta) & -\sin(2n\theta) \end{bmatrix}.$$

The key takeaways from the Galerkin analysis with only linear perturbation dependencies, i.e. $O(\epsilon)$, are that in the perturbed ring containing stiffness, i.e. width, and mass, i.e. point mass, perturbations from a uniform thin ring, each point mass contributes an *additive* change in the mass matrix, and point masses do not contribute to changes in the stiffness matrix; only a width perturbation accomplishes this.

2.3 Mass/Stiffness Perturbation Matrices for $n = 2$ Modes with Point Mass Perturbations and $p = 1\theta, 2\theta, 3\theta, 4\theta$ Width Perturbations

For sake of brevity, and without loss of generality in how the results qualitatively extend to other vibrational mode pairs, the analysis is now focused exclusively to the $n = 2$ mode pair and on only linear dependencies in perturbation parameters. All width perturbations are also assumed fixed at $\Psi_h = 0$. The $n = 2$ mode pair mass and stiffness nominal and perturbation matrices pertinent to the point mass perturbation are then as follows:

$$M = \frac{5}{2}\Gamma I, \quad K = 36\pi h_0^3 \kappa I,$$
$$\Delta_M = \Delta_{M_{m_1}} + \Delta_{M_{m_2}} + \Delta_{M_h},$$
$$\Delta_{M_{m_i}} = \frac{\Gamma \epsilon_{m_i}}{4} \begin{bmatrix} 5 + 3\cos(4\Psi_i) & 3\sin(4\Psi_i) \\ 3\sin(4\Psi_i) & 5 - 3\cos(4\Psi_i) \end{bmatrix}, \quad i = 1, 2.$$

The $p = 1, 2, 3, 4$ ring width perturbations are exaggerated and visualized in Figure 2.3. The

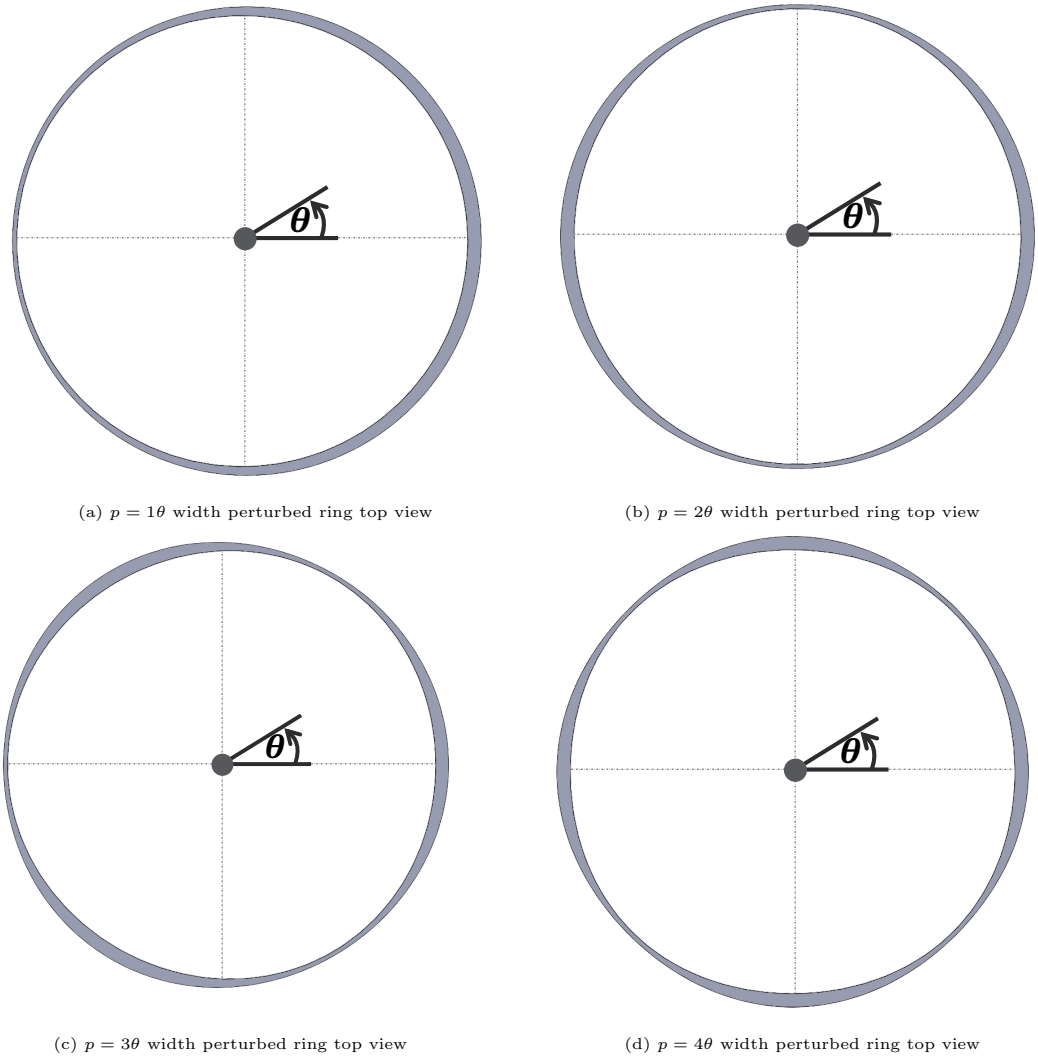

(a) $p = 1\theta$ width perturbed ring top view

(b) $p = 2\theta$ width perturbed ring top view

(c) $p = 3\theta$ width perturbed ring top view

(d) $p = 4\theta$ width perturbed ring top view

Figure 2.3: Exaggerated views of $p = 1\theta, 2\theta, 3\theta, 4\theta$ width perturbations.

effects of the width perturbations on the mass and stiffness matrices up to linear dependency are separately listed below to highlight that the only linear effect on the mass and stiffness matrices due to width perturbations for the $n = 2$ mode pair is with a 4θ ring width

perturbation.

$$\Delta_{M_h} = \begin{cases} \frac{3\Gamma\epsilon_h}{4} I & p = 4 \\ 0 & p \neq 4 \end{cases}, \tag{2.8}$$

$$\Delta_K = \begin{cases} 27\epsilon_h \pi \kappa h_0^3 \begin{bmatrix} 0 & 1 \\ 1 & 0 \end{bmatrix} & p = 4 \\ 0 & p \neq 4 \end{cases}. \tag{2.9}$$

Although perhaps uninteresting due to the fact that the $1\theta, 2\theta$, and 3θ width perturbations do not contribute to a change in the mass and stiffness matrices, it is necessary to be complete with usage of $p = 1, 2, 3, 4$ for the $p\theta$ width perturbations. As seen in the subsequent section, there are differences in how each width perturbation affects the *center of mass* in the structure, which is a vital portion of the analysis, yielding a simple sense as to where there may be energy losses in the structure if say the ring were held fixed to some base in the ring center.

2.4 Modal Center of Mass Motion

With infrastructure in place for the Galerkin analysis, the ring displacements can be separated into x and y coordinate components, denoted X_{ring} and Y_{ring}, respectively. These are defined as functions of θ, and are obtained by projecting the radial and tangential displacement components appropriately combined along with the nominal thin ring locations projected to x and y coordinates. Figure 2.4 highlights these component projections visually. Combining all projected components yields:

$$X_{ring}(\theta) = U(\theta)\cos(\theta) + W(\theta)\sin(\theta) + R\cos(\theta), \tag{2.10}$$

$$Y_{ring}(\theta) = W(\theta)\cos(\theta) + U(\theta)\sin(\theta) + R\sin(\theta). \tag{2.11}$$

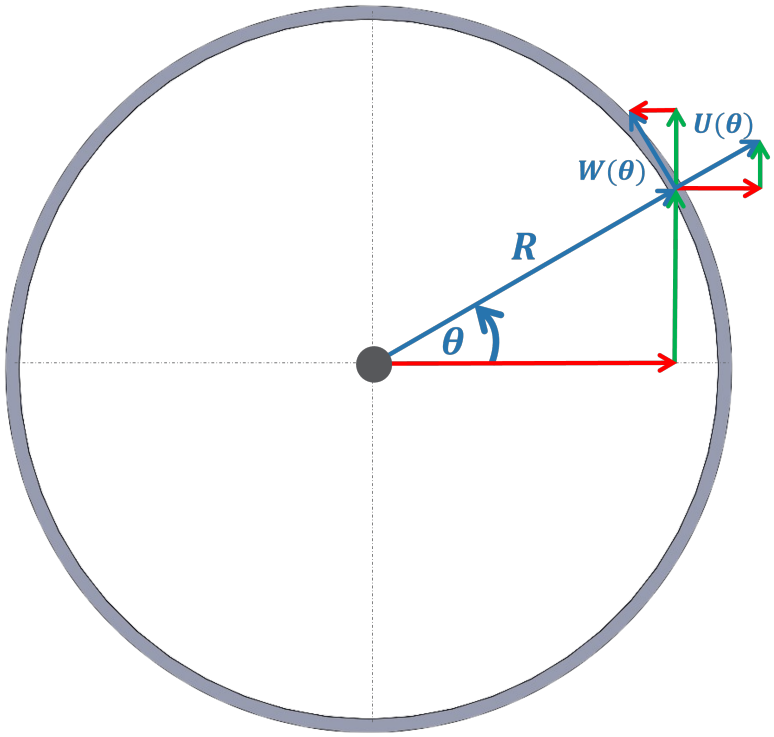

Figure 2.4: A uniform thin ring is shown along with its radial and tangential displacements at θ. Projecting the magnitude R vector from ring center to the ring angle of θ as well as $U(\theta)$ and $W(\theta)$ onto the x and y axes yields X_{ring} (red) and Y_{ring} (green).

To obtain the ring center of mass, denote M_x and M_y as the moments of inertia about the x-axis and y-axis, respectively, and denote m_{tot} as the total ring mass. Then,

$$\begin{aligned} m_{tot} &= \int_{\theta=0}^{2\pi} \rho(\theta) dV = La \int_{\theta=0}^{2\pi} \rho(\theta) d\theta, \\ M_x &= \int_{\theta=0}^{2\pi} X_{ring}(\theta)\rho(\theta) dV = La \int_{\theta=0}^{2\pi} X_{ring}(\theta)\rho(\theta) d\theta, \\ M_y &= \int_{\theta=0}^{2\pi} Y_{ring}(\theta)\rho(\theta) dV = La \int_{\theta=0}^{2\pi} Y_{ring}(\theta)\rho(\theta) d\theta, \end{aligned}$$

and thus the motion for the center of mass in x and y coordinates is defined by

$$X_{cm} = M_x/m_{tot},\ Y_{cm} = M_y/m_{tot}. \tag{2.12}$$

Splitting these into terms attached to B_1 and B_2 then yields the x and y components of the center of mass local to each *individual vibrational mode* defined by the $n\theta$ basis functions.

2.4.1 Center of Mass for $n = 2$ Modes with Point Mass Perturbations and $p = 1\theta, 2\theta, 3\theta$ Width Perturbations

Computing the center of mass for the point mass perturbations and any width perturbation yields $\begin{bmatrix} X_{cm} & Y_{cm} \end{bmatrix}^T = (C + \Delta_C)$. C depends on the width perturbation defined by p, and has the following form:

$$C = \begin{cases} \dfrac{\epsilon_h}{4} \begin{bmatrix} 0 & 1 \\ -1 & 0 \end{bmatrix} \mathbf{b} & p = 1 \\ 0 & p = 2 \cdot \\ \dfrac{3\epsilon_h}{4} \begin{bmatrix} 0 & 1 \\ 1 & 0 \end{bmatrix} \mathbf{b} & p = 3 \end{cases} \tag{2.13}$$

Δ_c is associated with the point mass perturbations, and has the following form

$$\Delta_C = \Delta_{C_{m_1}} + \Delta_{C_{m_2}}, \tag{2.14}$$

$$\Delta_{C_{m_i}} = \epsilon_{m_i} \left(\begin{bmatrix} a\cos(\psi_i) \\ a\sin(\psi_i) \end{bmatrix} + \begin{bmatrix} \cos(\psi_i) & \sin(\psi_i) \\ -\sin(\psi_i) & \cos(\psi_i) \end{bmatrix} \mathbf{b} \right), \quad i = 1, 2. \tag{2.15}$$

Again, $\mathbf{b}$ is the vector containing the unknown amplitudes of the nth vibrational modes, or $\mathbf{b} = \begin{bmatrix} B_1 & B_2 \end{bmatrix}^T$.

2.4.2 Effect of Point Mass Perturbations on Center of Mass for $n = 2$ Modes with 4θ Width Perturbation

To simplify the subsequent analysis, assume a $p = 4$ ring width perturbation is located at $\Psi_h = 45°$. For $n = 2$, the only width perturbation that has a linear dependency on

the perturbation parameter is when $p = 4$, however, unlike Δ_K in (2.8), due to the ring essentially being rotated by 45°, $\Delta_K = 27\epsilon_h \pi \kappa h_0^3 I$, where $I \in \mathbb{R}^{2x2}$ is the identity matrix. As seen in Figure 2.5, due to the axial symmetry of the width perturbation about the ring center, the center of mass nominally with the width perturbation is $C = 0$, however, crucially this width perturbation detunes the $n = 2$ mode pair. Δ_C is associated with the point mass perturbations, and is the same as in (2.14).

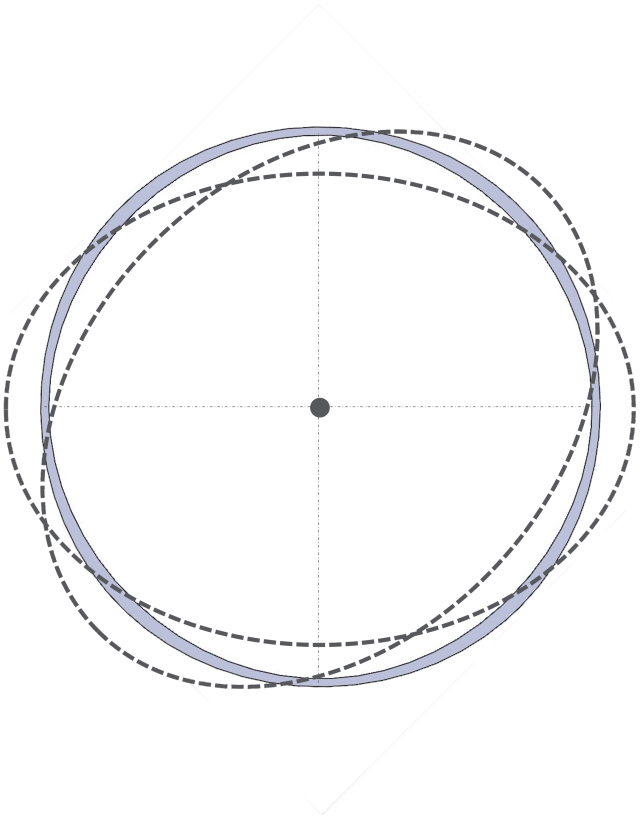

Figure 2.5: The 4θ width perturbation centered at 45° is shown. The $n = 2$ mode pair is detuned, and the perturbation fixes the mode pair at 0° and 45° in order of their vibrational frequencies, with mode shapes are shown in dashed gray. The perturbation maintains axial symmetry about the ring center and thus the center of mass remains fixed.

Conventional tuning techniques in the group, while restricting the number of point masses to two point masses, would without loss of generality place two point masses of perturbation amplitudes $\epsilon_{m_1} = \epsilon_{m_2} = \epsilon_m$, with ϵ_m accounting for the width perturbation detuning due with weight ϵ_h, at $\Psi_{1,2} = \pm 45°$ such that the $n = 2$ ring modes are tuned, as seen in Figures 2.6 and 2.7 below.

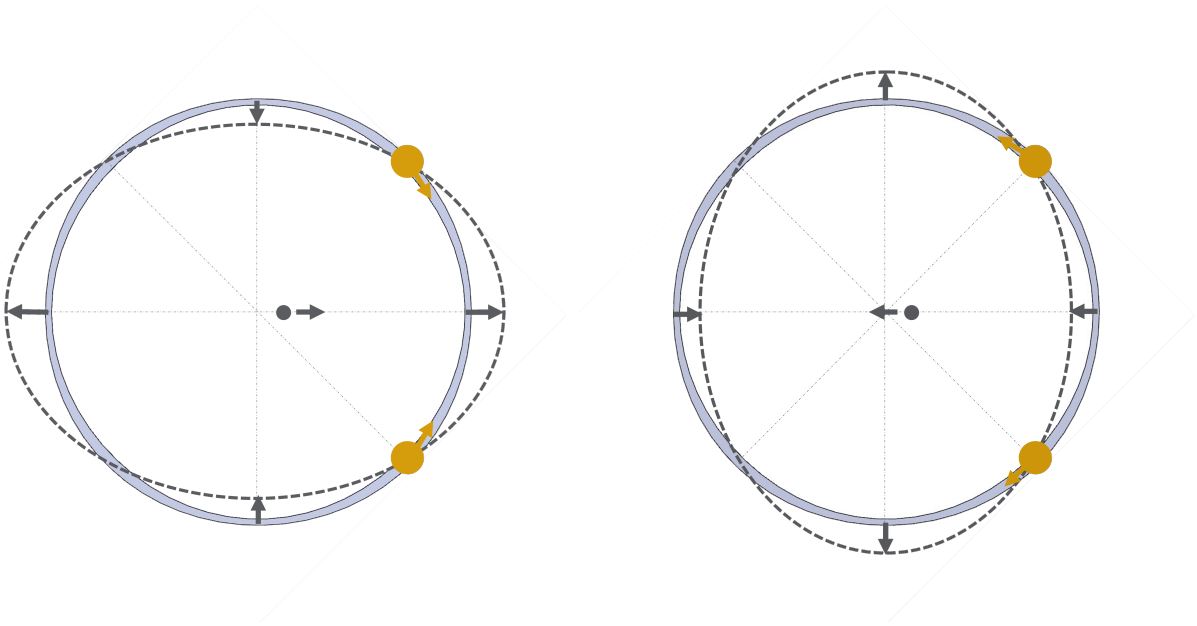

Figure 2.6: Snapshots of $n = 2$ mode located at 0° when two trimming point masses are placed at $\psi_{m_1,m_2} = \pm 45^\circ$, unbalancing the ring. With the mode, the masses also move with the ring and thus as a result, the center of mass is clearly displaced along the **x-axis**.

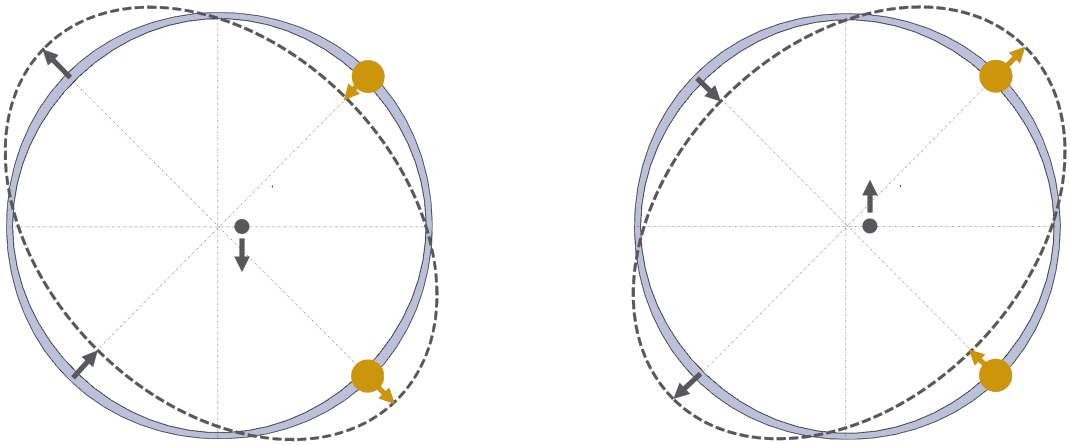

Figure 2.7: Snapshots of $n = 2$ mode located at $\theta = 45^\circ$ when two trimming point masses are placed at $\psi_{m_1,m_2} = \pm 45^\circ$, unbalancing the ring. In vibration, the masses also move with the ring and thus as a result, the center of mass is clearly displaced along the **y-axis**.

Although the n=2 modes are now tuned, the point masses perturb the center of mass such that the center of mass displacement to *linear perturbation order*, plugging in the correct

mass locations and equal weights, is

$$\Delta_C = \epsilon_m \left(\begin{bmatrix} \sqrt{2}a \\ 0 \end{bmatrix} + \begin{bmatrix} \sqrt{2} & 0 \\ 0 & \sqrt{(2)} \end{bmatrix} \mathbf{b} \right). \tag{2.16}$$

In other words, in general, the position of the point masses shifts the position of center of mass by $\sqrt{2}a\epsilon_m$ on the x-axis. For the initially lower frequency mode located at 0°, the center of mass oscillates with weight $\sqrt{2}\epsilon_m B_1$ on the x-axis, however, for the initially higher frequency mode located at 45°, the center of mass oscillates with weight $\sqrt{2}\epsilon_m B_2$ on the y-axis.

In a resonator with a fixed center disk (or center stem) connected to the coupled thin rings, any modal displacement in the center of mass requires a reaction force from the base holding the resonator fixed, not only coupling the resonator vibrational modes to the center stem, but also leading to energy losses in the resonator vibrational modes.

Now consider a slightly different set of four chosen tuning masses at ±45° and ±135°, such that the point mass weight, ϵ_m, for all four point masses is chosen, accounting for the width perturbation detuning with weight ϵ_h, in order to tune the $n = 2$ ring vibrational modes. With the knowledge that the effects of the point masses on the perturbed center of mass displacement are additive, it can quickly be shown that $\Delta_C = 0$, and thus the n=2 ring modes are now tuned without a change to the center of mass, i.e. there is no coupling between a fixed ring center and ring vibration, seen clearly below in Figure 2.8 and 2.9.

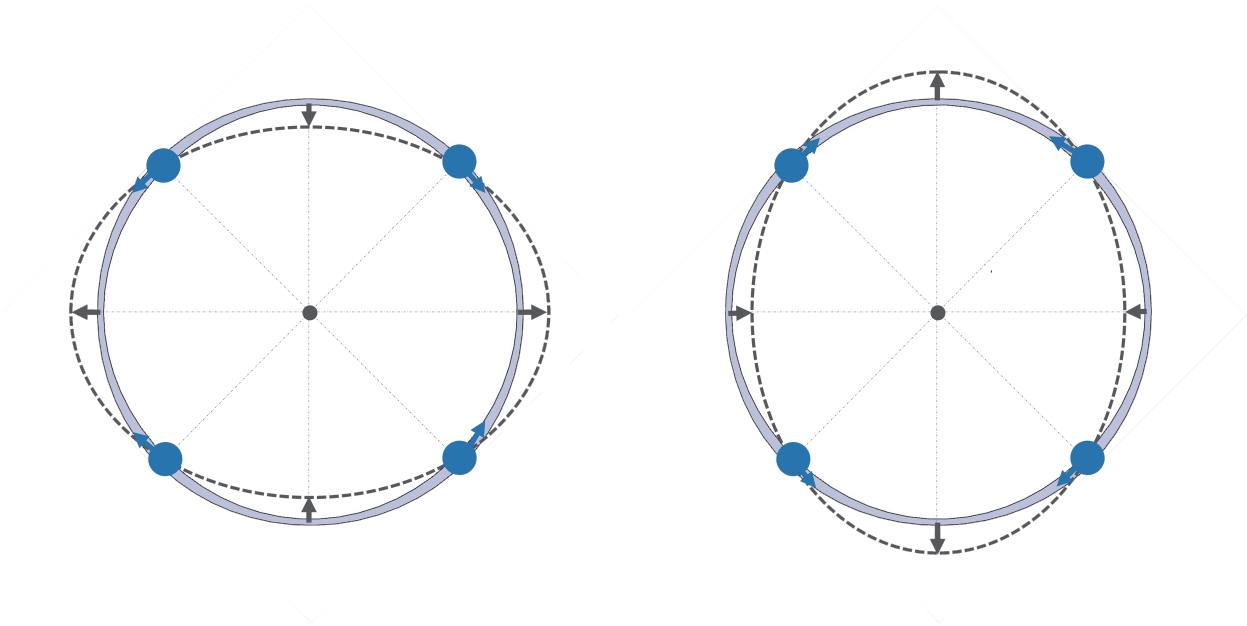

Figure 2.8: Snapshots of n=2 mode located at $\theta 0°$ when four trimming point masses are placed at $\psi_{m_1,m_2} = \pm 45°$ and $\psi_{m_3,m_4} = \pm 135°$, keeping the ring balanced. In vibration, although the masses move with the ring, the center of mass remains fixed at the ring center and is not displaced.

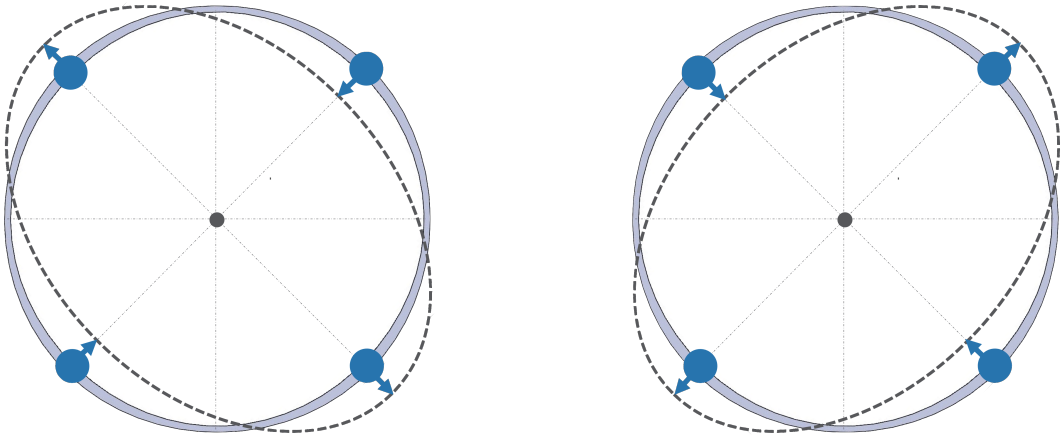

Figure 2.9: Snapshots of n=2 mode located at $\theta = 45°$ when four trimming point masses are placed at $\psi_{m_1,m_2} = \pm 45°$ and $\psi_{m_3,m_4} = \pm 135°$, keeping the ring balanced. In vibration, although the masses move with the ring, the center of mass remains fixed at the ring center and is not displaced.

2.5 Extension to Resonator System Measurement and Modeling

In essence the prior subsection lays out a simple toy example in the context of $n = 2$ ring modes with a $p = 4$ width perturbation, but crucially highlights that with knowledge of how point masses affect the coupling between resonator mode vibration and a fixed resonator stem would help inform potential methods of point mass placement to reduce that coupling while simultaneously tuning the vibratory modes if desired.

The results of the work in Chapter 5 extends the insight gained by analyzing a thin ring to the modeling, measurement, and mitigation of stem/resonator coupling through the design, construction, and testing of a six degree of freedom force/torque sensor to fully detect stem/resonator coupling for a simple oscillator, a lightweight steel tuning fork, with tuning fork modes that are already well modeled in terms of their resonator/fixed base interaction.

Before even arriving at this end goal, it was first crucial to accurately arrive at a model of the system of interest, whether that be an isolated resonator or a combined resonator/transducer system, localized from both of which extraction of modal information is required for any further physical modeling or analysis. This motivates the system identification technique in the following chapter.

CHAPTER 3

Hankel Matrix State Space ID from Ring-Down Data

Extracting modal properties localized to a certain vibratory mode is of crucial importance in the modeling and tuning of these sensors. A signal analyzer can generate an empirical set of frequency responses to extract a parametric model for the multi-input, multi-output (MIMO) system or simulations can generate frequency responses via applications such as COMSOL. Of note are the parametric models fit from empirical frequency responses in [SKS15], [KM06], and [SKM09]. The empirical frequency responses are generated via a signal analyzer that detects the system response in real time when a chirp signal (or a random white noise sequence) is used as the test input.

This chapter describes in detail analytical and experimental results for an alternative method (used in [BM19]) to better extract empirical frequency responses for a particular resonator mode. The advantage of this new method for deriving an empirical frequency response via ring-down data is in eliminating parasitic coupling and feed-through dynamics present in typical empirical frequency responses typically seen when measuring the motional frequency response during as the system sees an input stimulus. The chapter is organized as follows. Section 3.1 reviews conventional Hankel Matrix based state space model identification in great detail. Section 3.2 extends and customizes the technique to resonators via the use of burst chirp excitation, Section 3.3 highlights experimental results for the $n = 1, 2, 3$ vibratory mode pairs, and Section 3.4 rigorously discusses how the model captures the combined effect of the resonator and input/output smoothing and anti-alias filters as well as how the forcing scheme is necessary and sufficient for complete system model identification.

Section 3.5 derives a "zoom" method to reduce computational cost and shows results from the resonator that highlight the method's efficacy. Section 3.6 concludes the chapter and discusses potential applications of this modeling process, such as to fit the predictive model seen in Chapter 4.

3.1 State Space Resonator Model ID

The resonator is assumed to be modeled by a linear difference equation

$$x_{k+1} = Ax_k + Bu_k, \tag{3.1}$$

$$y_k = Cx_k, \tag{3.2}$$

where y_k represents the pick-off measurements in response to the applied stimulus u_k. The integer index k represents the sample number for the state, and input and output variables. It is assumed that a uniform sample period of t_s is used in an experiment and consequently, the model inherits this sample period. There are n_i input channels, n_o output channels, and state dimension n_s. Thus, $x_k \in \mathbb{R}_s^n$, $y_k \in \mathbb{R}_o^n$, $u_k \in \mathbb{R}_i^n$ $A \in \mathbb{R}^{n_s \times n_s}, B \in \mathbb{R}^{n_s \times n_i},$ and $C \in \mathbb{R}^{n_o \times n_s}$. Given input and output sequences $\{u_k\}$ and $\{y_k\}$, the objective is to determine $\{A, B, C\}$, the model matrices, based on the test data. If only the modal frequencies, time constants, and mode shapes are desired then it is only necessary to determine $\{A, C\}$. If the motional frequency response is further required, then it is necessary to also determine B for a complete input-output description of the resonator.

Such models arise when testing linear systems according to the block diagram in Figure 3.1, where H_{s}, H_{a} and H_{sys} represent smoothing filters, anti-alias filters, and the system under test, respectively. The input sequence is specified and implemented by the digital signal processing unit (DSP), and the DSP also samples the response to input stimulus. The DAC implements a zero-order hold on the discrete-time signal $\vec{u}$ and the ADC sam-

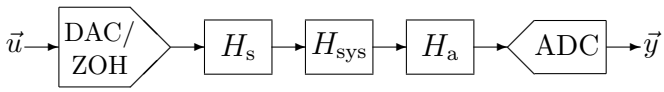

Figure 3.1: Block diagram for generating test data. The system under test, anti-alias filter, and smoothing filter are denoted H_{sys}, H_{a}, and H_{s}, respectively.

ples the continuous-time signals to yield the discrete-time signal $\vec{y}$. If all dynamic elements in the block diagram are linear, then the sampled data nature of the experiments calls for the discrete-time system described by (3.1) and (3.2) as a model for the resonator, which describes the relationship between the input-output samples and the state variable $\vec{x}$, e.g., [AW11]. The state variables include those of the system, smoothing filters, and anti-alias filters. The models are often denoted with the triplet $\{A, B, C\}$.

The modal frequencies and associated damping are determined from analysis of the eigenvalues of A: a resonator mode with frequency ω_0 and decay envelope $e^{-\alpha t}$, $\alpha > 0$, will produce an eigenvalue pair $e^{(-\alpha \pm j\omega_0)ts}$ of A. Mode shapes can be determined from analysis of C and the eigenvectors of A –more details are given in Section 3.2.3. The motional frequency response excluding the effects of parasitic forcer-pickoff coupling requires estimating B as well.

3.1.1 Ho-Kalman Procedure

The foundation of the system identification method is the Ho-Kalman algorithm [HK66]. The Ho-Kalman algorithm estimates $\{A, B, C\}$ based on the pulse response of the system. The pulse response is the matrix-valued sequence $\{Y_k\}$, $Y_k \in \mathbb{R}^{n_{\mathrm{o}} \times n_{\mathrm{i}}}$, where $Y_0 = 0$, $Y_k = CA^{k-1}B$, $k > 0$. $\mathbb{R}$ denotes the field of real numbers. The pulse response is generated by stimulating the system, starting from a state of rest ($\vec{x}_0 = 0$), to unit pulses that are sequentially applied to each of the n_i input channels. In other words, the l^{th} column of the pulse response represents the sequence of output vectors that are obtained when the l^{th} input channel is a unit pulse and all other input channels are zero. A realization of the system is obtained by analyzing the following block-Hankel matrices formed from the pulse response

data,

$$\mathcal{H}_0 = \begin{bmatrix} Y_1 & Y_2 & \cdots & Y_{n_c} \\ Y_2 & Y_3 & \cdots & Y_{n_c+1} \\ Y_3 & Y_4 & & \vdots \\ \vdots & \vdots & \ddots & \vdots \\ Y_{n_r} & Y_{n_r+1} & \cdots & Y_{n_r+n_c-1} \end{bmatrix}, \qquad \mathcal{H}_1 = \begin{bmatrix} Y_2 & Y_3 & \cdots & Y_{n_c+1} \\ Y_3 & Y_4 & \cdots & Y_{n_c+2} \\ Y_4 & Y_5 & & \vdots \\ \vdots & \vdots & \ddots & \vdots \\ Y_{n_r+1} & Y_{n_r+2} & \cdots & Y_{n_r+n_c} \end{bmatrix}, \tag{3.3}$$

where $\mathcal{H}_0, \mathcal{H}_1 \in \mathbb{R}^{n_o n_r \times n_i n_c}$. The column and row dimensions use n_c and n_r pulse response samples, respectively. The number of samples that are used to create these matrices is based on the expected model order as well as the need to accurately capture time constants associated with the decay rates. Based on the model generating the pulse response data, $\mathcal{H}_0$ is factored as a product,

$$\mathcal{H}_0 = \mathcal{O}\mathcal{C}, \tag{3.4}$$

where $\mathcal{O}$ and $\mathcal{C}$ are the observability and controllability matrices associated with the realization,

$$\mathcal{O} = \begin{bmatrix} C \\ CA \\ CA^2 \\ \vdots \\ CA^{n_r-1} \end{bmatrix} \in \mathbb{R}^{n_o n_r \times n_s}, \qquad \mathcal{C} = \begin{bmatrix} B & AB & A^2B & \cdots & A^{n_c-1}B \end{bmatrix} \in \mathbb{R}^{n_s \times n_i n_c}. \tag{3.5}$$

If the state space model defined by (3.1) and (3.2) is minimal, then the factorization shows that $\operatorname{rank}\mathcal{H}_0 = \operatorname{rank}\mathcal{O} = \operatorname{rank}\mathcal{C} = n_{\mathrm{s}}$ (the state dimension) when a sufficiently large number of pulse response points are used in forming $\mathcal{H}_0$ (typically, $n_{\mathrm{o}}n_r >> n_{\mathrm{s}}$ and $n_{\mathrm{i}}n_c >> n_{\mathrm{s}}$). In this manner C and B are obtained from $\mathcal{O}$ and $\mathcal{C}$, and since $\mathcal{H}_1 = \mathcal{O}A\mathcal{C}$, A is computed

$$A = \mathcal{O}^{\dagger}\mathcal{H}_1\mathcal{C}^{\dagger}, \tag{3.6}$$

where $\mathcal{O}^{\dagger}$ and $\mathcal{C}^{\dagger}$ represent left and right inverses of $\mathcal{O}$ and $\mathcal{C}$, respectively, i.e. $\mathcal{O}^{\dagger}\mathcal{O} = I$ and $\mathcal{C}\mathcal{C}^{\dagger} = I$, where I denotes the identity matrix.

In practice, a model of a to-be-determined order is extracted from pulse response measurements obtained in an experiment. In this case, $\mathcal{H}_0$ and $\mathcal{H}_1$ are still formed from the samples of the transient response. The measurement samples include buffer noise and effects of disturbances and consequently $\mathcal{H}_0$ is typically full rank, however, there are often a handful of dominant singular values that can be used to closely approximate $\mathcal{H}_0$ with a lower rank matrix that is then factored according to (3.4). Thus, the first step in analyzing $\mathcal{H}_0$ is to compute its singular values where the number of dominant singular values provides insight into an adequate model order. Suppose $U\Sigma V^T$ is a singular value decomposition (SVD) of $\mathcal{H}_0$, where U and V are orthogonal matrices, and $(\cdot)^T$ denotes transpose. If the first r singular values of $\mathcal{H}_0$ are dominant, i.e. $\sigma_r >> \sigma_{r+1}$, then $\mathcal{H}_0$ can be approximated by a rank r matrix $\mathcal{H}_{0,r} = U_r\Sigma_r V_r^T$ where U_r is a sub-matrix of U formed from its first r columns, V_r is a sub-matrix of V formed from its first r columns, and Σ_r is a diagonal matrix with diagonal elements $\{\sigma_1, \sigma_2, \ldots, \sigma_r\}$ (the first r singular values). Thus, $\mathcal{H}_0$ is replaced by a lower rank approximation which retains the dominant singular values and the corresponding left and right singular vectors. This approach was first proposed in [ZM74] as a variant of the basic Ho-Kalman algorithm. The results in this paper demonstrate that this approximation of $\mathcal{H}_0$ works quite well when the signal-to-noise ratio associated with the measurements is high. The factorization of $\mathcal{H}_{0,r}$ is not unique, however, other factorizations correspond to different

coordinate representations of an r-state realization with the same input-output behavior. One choice of factorization based on the SVD is $\mathcal{O} = U_r \Sigma_r^{\frac{1}{2}}$ and $\mathcal{C} = \Sigma_r^{\frac{1}{2}} V_r^T$. The state space C matrix is defined as the first n_o rows of $\mathcal{O}$, and B is defined as the first n_i columns of $\mathcal{C}$. The left and right inverses of the factors are $\mathcal{O}^\dagger = \Sigma_r^{-\frac{1}{2}} U_r^T$ and $\mathcal{C}^\dagger = V_r \Sigma_r^{-\frac{1}{2}}$ and the computation of A is given by (3.6).

3.2 Application to Resonators

The modeling approach proposed in this section can be applied to any MEMS resonator, however, the Ho-Kalman procedure will be adapted for determining models of the resonator schematic shown in Figure 1.1, where further resonator and experimental details are also described. The input and output electrode arrangement defines a 2-input, 8-output system ($n_o = 8$ and $n_i = 2$ in (3.1) and (3.2)). Although it is a relatively simple task to locate the modal frequencies to within a few Hz, this system identification technique extracts detailed information on the modal frequencies, damping, and mode orientations even when the frequencies within a given pair are essentially equal.

3.2.1 Transient Response Data

Models are separately developed for each pair of vibratory modes. The Ho-Kalman procedure is applied to measurements of the resonator's transient, unforced response. The input is not impulsive, however, because the energy density of a pulse is too small to evoke a measurable response due to physical limits on the pulse amplitude. Although it is possible to estimate the pulse response of a system using persistent excitation signals (for example, wideband random inputs), this approach may not be desirable in MEMS resonator applications. First, coupling between the excitation and pick-off electrodes can easily obscure the resonator's motional response, eg. [GBG18], and the use of persistent signals will always include effects of coupling due to the signal processing that is used to derive the pulse response estimate. Second,

the smoothing required to recover the pulse response from input-output data generated with persistent input signals is generally associated with long testing times in order to obtain accurate estimates of mean-square spectra or correlation functions. It is important that the resonator dynamics be time invariant during such tests, however, this may be difficult to achieve in some cases, e.g. modal frequency drift due to small changes in resonator temperature.

The proposed testing technique employs a periodic burst chirp signal applied to each input channel. The burst energy is constrained to be in a neighborhood of a pair of degenerate modes and, thus, produces a strong response from these modes. One period of the scalar-valued periodic burst chirp excitation signal v, written as a continuous-time function, is

$$v(t) = \begin{cases} 0, & t \in [0, \tau_p - \tau_b) \\ a\cos\big(2\pi f_{\text{ch}}(t)(t - \tau_p + \tau_b)\big), & t \in [\tau_p - \tau_b, \tau_p) \end{cases} \tag{3.7}$$

The time-dependent frequency of the burst is given by

$$f_{\text{ch}}(t) = \frac{1}{2\tau_b}(f_{\text{hi}} - f_{\text{low}})(t - \tau_p + \tau_b) + f_{\text{low}}. \tag{3.8}$$

The duration of the burst is τ_b seconds, τ_p is the signal period ($\tau_p > \tau_b$), and a is the amplitude of the burst. This signal concentrates its energy in the frequency band $[f_{\text{low}}, f_{\text{hi}}]$ Hz. The burst duration, amplitude, and the frequency band where its energy is concentrated are easily adjusted using parameters in the time-domain description of the function. The phase of burst is chosen so that the burst occurs at the *end* of the period. Both input channels are stimulated with the periodic burst chirp (3.7), however, a time delay equivalent to half a period is introduced between the bursts appearing in each channel, in other words, the resonator input is defined

$$\vec{u}(t) = \begin{bmatrix} v(t) \\ v(t - \tau_p/2) \end{bmatrix} \tag{3.9}$$

where $\tau_p/2 > \tau_b$ so that there is an input-free transient period between bursts. Discrete-time

versions of these signals are defined as $v_k = v(kt_s)$ and $\vec{u}_k = \vec{u}(kt_s)$,

$$v_k = 0, \quad k \in [0, N_p - N_b - 1]$$

and

$$v_k = a\cos\big(2\pi f_{\mathrm{ch},k}(k - N_p + N_b)t_s\big)$$
$$k \in [N_p - N_b, N_p - 1],$$

where $f_{\mathrm{ch},k} = f_{\mathrm{ch}}(kt_s)$ is an appropriate update of the frequency function in (3.8). The signal processing equipment implements the discrete-time signals such that there are N_p samples in one period and N_b samples in the burst portion of the signal ($N_p t_s = \tau_p$ and $N_b t_s = \tau_b$). It is also assumed that the number of points in one period is even (this simplifies notation in the analysis to follow and can be relaxed). The signal (3.9) is implemented as the input for all tests reported in this paper. The period and chirp frequency range are adjusted to suit the testing of a specific pair of modes. An example of $\vec{u}$ is shown in Figure 3.2 where $\tau_b = 1$ second and $\tau_p = 10$ seconds. The chirp frequency range is chosen to excite either the $n = 1$, $n = 2$ or $n = 3$ pair of modes, however, the sinusoidal oscillation of the chirp cannot be resolved on the displayed time scale. It is necessary to stagger the bursts as shown in (3.9) because simultaneously applying the same stimulus to each input channel is equivalent to exciting the resonator with a single "virtual" electrode –such a test may not adequately excite both modes in a degenerate pair (for example, the virtual electrode may be located near a radial node of the mode shape and therefore will weakly couple to that mode). A more rigorous explanation for this is shown in 3.4.2.

3.2.2 Defining the Hankel matrices

The transient data between bursts is used to form the block-Hankel matrices (3.3). Since $\vec{u} = 0$ in these intervals, there is no parasitic input-output coupling and so the resonator model built from this data will not feature this coupling. An example of measurements

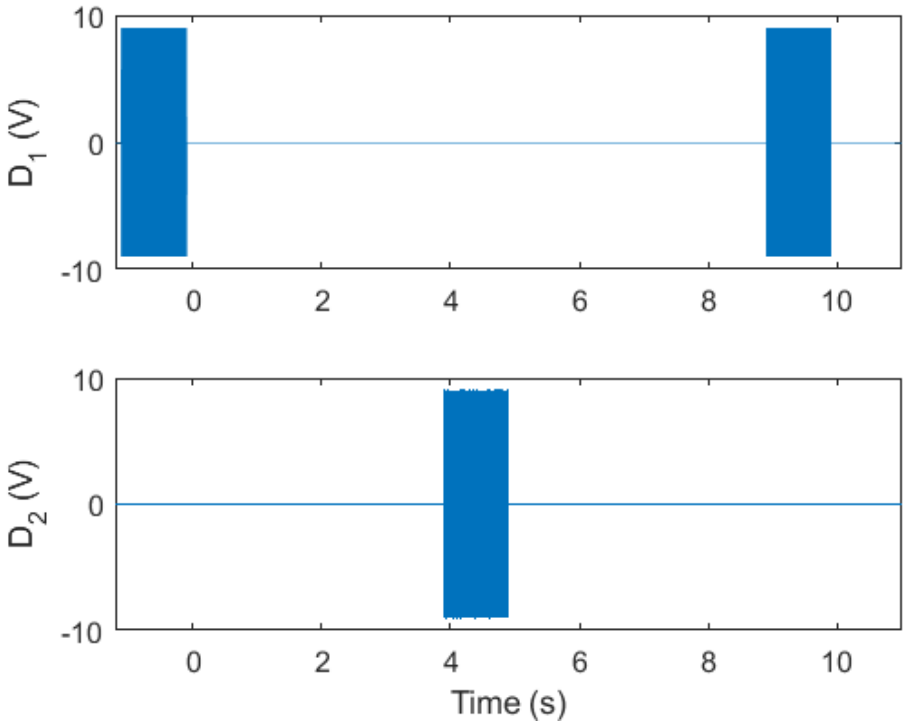

Figure 3.2: Burst chirp input (3.9) applied to the electrodes D_1 and D_2. The signals in each input channel are periodic ($\tau_p = 10$ seconds) and have identical bursts of duration $\tau_b = 1$ second, however, there is a 5 second delay ($\tau_p/2$) between the input channels. The interval between bursts generates input-free transient data from which the resonator model is developed.

when the bursts are designed to excite the $n = 1$ pair are shown in Figure 3.3. The data segment corresponding to $t \in [0, 3]$ (highlighted red) is used in lieu of the first column of the resonator's pulse response, and the data segment corresponding to $t \in [5, 8]$ (also highlighted red) is substituted for the second column of the resonator's pulse response. Since $t_s = 1/70000$ second, there are over 200k data points recorded from each each pick-off for each transient data segment. The data used for modeling the resonator is acquired in a time interval that is less than one period of the input and in essence provides a "snapshot" of the resonator dynamics that is less susceptible to temperature-induced drift.

In contrast to the traditional Ho-Kalman procedure, this analysis does not directly yield the state-space B matrix but instead identifies "initial conditions" for the model's state vector at the start of the two data segments (at $t = 0$ and $t = 5$ in Figure 3.3). Let $\vec{x}_{0,1}, \vec{x}_{0,2} \in \mathbb{R}^{n_s}$

correspond to the model state at $t = 0$ and $t = 5$, respectively. Define $X = \begin{bmatrix} \vec{x}_{0,1} & \vec{x}_{0,2} \end{bmatrix}$. The transient responses are assumed to be generated by $Y_k = CA^kX \in \mathbb{R}^{8\times 2}$, $k \geq 0$, where the index value $k = 0$ refers to the first data sample in both data segments. The Hankel matrices for this scenario are slightly modified with a shift in indices,

$$\mathcal{H}_0 = \begin{bmatrix} Y_0 & Y_1 & \cdots \\ Y_1 & Y_2 & \cdots \\ \vdots & \vdots & \ddots \end{bmatrix}, \quad \mathcal{H}_1 = \begin{bmatrix} Y_1 & Y_2 & \cdots \\ Y_2 & Y_3 & \cdots \\ \vdots & \vdots & \ddots \end{bmatrix}. \tag{3.10}$$

Note that

$$\mathcal{H}_0 = \mathcal{O}\mathcal{C}_X, \quad \mathcal{H}_1 = \mathcal{O}A\mathcal{C}_X, \tag{3.11}$$

where $\mathcal{O}$ is given in (3.5) and $\mathcal{C}_X$

$$\mathcal{C}_X = \begin{bmatrix} X & AX & A^2X & \cdots & A^{n_c-1}X \end{bmatrix} \in \mathbb{R}^{n_s \times n_i n_c}.$$

Thus, analysis of $\mathcal{H}_0$ and $\mathcal{H}_1$ yield A, C and X for the pair of modes under consideration.

The number of block-columns and block-rows in the Hankel matrices are denoted n_c and n_r. In general, one dimension must be large enough to accurately capture the time constants of the modes. A lower bound for the number of transient data points required in the analysis can be estimated. Suppose a resonant mode has modal frequency f Hz and time constant τ seconds. For standard sampling of the resonator transient response at least four samples per period of oscillation is desirable so $f_s > 4f$, where f_s is the sampling rate in Hz ($f_s = 1/t_s$, for sample period t_s seconds). An accurate measurement of the resonator time constant requires a data record of minimum length, for example, τ seconds (one time constant). Thus, the number of points in the transient data record that is used to form the Hankel matrices must be at least $f_s\tau > 4f\tau \approx Q$, where Q is the quality factor associated with the mode. For high quality factor resonators, the data sets can become quite large and although storage is typically not an issue, the analysis of large Hankel matrices can require

significant computation. The "zoom" technique proposed in Section 3.5 significantly reduces the burden of storing and processing large data sets.

3.2.3 Modal frequencies, damping, and orientation

The A and C matrices can be analyzed for modal frequencies, damping and mode orientation. Since the identified model is obtained by sampling a continuous-time system with sample period t_s, a mode with exponential decay rate σ (units of s^{-1}) and modal frequency ω_n (units of rad/s) will be associated with eigenvalues of the form $e^{(-\sigma \pm j\omega_n)t_s}$, where $j = \sqrt{-1}$. Thus, analysis of the eigenvalues of A yield the modal frequencies and time constants.

The mode orientation can be determined from the eigenvectors of A. First, referring to the pick-off electrode arrangement in Figure 1.1, the angular reference bisects the S_1 pick-off electrode and establishes the origin for angle measurements and hence the orientation of a mode shape. The position of S_1 with respect to the angle origin is denoted $\theta_1 = 0°$, the position of S_2 with respect to the angle origin is denoted $\theta_2 = 15°$ and so forth through S_8 with $\theta_8 = 315°$. Although the mode shapes for the resonator in Figure 1.1 do contain higher-order harmonics in θ, eg. [BKS17], they are very small in amplitude compared to the dominant terms. Thus, it is assumed a mode shape is defined by $a\cos(2n(\theta - \phi))$, where ϕ is the orientation, for a mode in the n^{th} pair of degenerate modes. The amplitude of the mode shape as measured by the pick-off electrodes is proportional to

$$\begin{bmatrix} a\cos(2n(\theta_1 - \phi)) \\ a\cos(2n(\theta_2 - \phi)) \\ \vdots \\ a\cos(2n(\theta_8 - \phi)) \end{bmatrix} = \underbrace{\begin{bmatrix} \cos(2n\theta_1) & \sin(2n\theta_1) \\ \cos(2n\theta_2) & \sin(2n\theta_2) \\ \vdots & \\ \cos(2n\theta_8) & \sin(2n\theta_8) \end{bmatrix}}_{\Theta} \begin{bmatrix} \alpha \\ \beta \end{bmatrix}$$

where $\alpha = a\cos(2n\phi)$ and $\beta = a\sin(2n\phi)$, and Θ is defined as indicated. The objective is to determine α and β from analysis of the identified model. Let $\vec{w}$ be an eigenvector of A

corresponding to eigenvalue $e^{(-\sigma+j\omega_n)t_s}$ and consider the unforced response of the resonator with initial condition $\vec{x}_0 = \frac{1}{2}(\vec{w} + \vec{w}^*)$, where * denotes complex-conjugate. This initial condition only involves one mode. The transient response, as measured by the pick-offs, would be

$$\begin{aligned} y_k &= CA^k \frac{1}{2}(\vec{w} + \vec{w}^*) \\ &= e^{-\sigma k t_s} \cos(\omega_n k t_s) \mathrm{Re}(C\vec{w}), \end{aligned}$$

where $\mathrm{Re}(C\vec{w}) \in \mathbb{R}^8$ denotes the real part of $C\vec{w}$. Alternatively, the imaginary part of $C\vec{w}$ can be used since this corresponds to replacing cos with sin in the transient response. Assuming the anti-alias filters are identical, an element of $\mathrm{Re}(C\vec{w})$ represents the amplitude of the mode shape expressed at the electrode of the corresponding measurement channel. Thus, α and β are determined from the following least squares problem,

$$\arg\min_{\alpha,\beta} \left\| \Theta \begin{bmatrix} \alpha \\ \beta \end{bmatrix} - \mathrm{Re}(C\vec{w}) \right\|,$$

where $\|\cdot\|$ denotes the Euclidean norm. The orientation ϕ of the mode with respect to the angle reference is computed from α and β.

3.2.4 Completing the resonator model

The B matrix in the resonator model can be determined once A and X have been extracted from the Hankel matrix analysis. The relationship between the columns of B, denoted $\vec{b}_1, \vec{b}_2 \in \mathbb{R}^{n_s}$, and X is

$$X = \begin{bmatrix} \vec{x}_{0,1} \\ \vec{x}_{0,2} \end{bmatrix} = \begin{bmatrix} I & A^{N_p/2} \\ A^{N_p/2} & I \end{bmatrix} \begin{bmatrix} \Gamma\vec{b}_1 \\ \Gamma\vec{b}_2 \end{bmatrix}, \tag{3.12}$$

where

$$\Gamma = (I - A^{N_p})^{-1} \left(\sum_{k=0}^{N_p-1} A^{N_p-1-k} v_k \right) \in \mathbb{R}^{n_s \times n_s}.$$

The resonator is asymptotically stable due to the fact that there is always some energy dissipation so $\det\left(I - A^{N_p}\right) \neq 0$. Therefore, Γ is always well-defined. The determinant of the matrix in (3.12) is equal to $\det\left(I - A^{N_p - 2N_b}\right)$ and is similarly non-zero. The elements of B in (3.12) are easily established by simulating the model from the identified initial conditions and knowledge of the burst chirp signal, v_k, all assuming the resonator has settled into its periodic response to the periodic input $\vec{u}$.

3.3 Identification Results

The modeling results for the $n = 1, 2, 3$ pairs of modes are presented in this section. The period of the input is 10 seconds in all cases, however, the burst chirp frequency parameters are tailored to a given pair based on the modal frequencies estimated from Figure 1.3. The input signal parameters are reported in Table 3.1. The chirp frequency span is 100 Hz. The burst amplitude is 9 volts and its duration is 1 second ($t_s = 1/70000$ second, $N_p = 700\,\text{k}$ and $N_b = 70\,\text{k}$). The block-Hankel matrices have the same dimension $n_r = 5$ for all cases, however, $n_c = 210000$ for $n = 1, 2$, and $n_c = 105000$ for $n = 3$. These choices correspond to using 3 seconds and 1.5 seconds of transient data in the formation of $\mathcal{H}_0$ and $\mathcal{H}_1$ –this is adequate to accurately identify the time constants associated with the modes.

The five largest singular values of $\mathcal{H}_0$ for each case ($V_{\text{bias}} = 0$) are given in Table 3.2. Since σ_4 exceeds σ_5 by at least two orders of magnitude in all cases, $\mathcal{H}_0$ is approximated by a rank 4 matrix. Thus, $n_s = 4$ and A, C and X are obtained from analysis of $\mathcal{H}_{0,4}$ and $\mathcal{H}_1$. The quality of the models can be assessed by simulating the model from the identified initial

Table 3.1: Burst chirp input parameters

Pair	f_{low} (Hz)	f_{hi} (Hz)	a (V)	τ_p (s)	τ_b (s)
$n = 1$	6525	6625	9	10	1
$n = 2$	13500	13600	9	10	1
$n = 3$	23825	23925	9	10	1

Table 3.2: Five largest singular values of $\mathcal{H}_0$

Pair	σ_1	σ_2	σ_3	σ_4	σ_5	σ_4/σ_5
$n=1$	338	315	226	212	0.12	1841
$n=2$	154	147	124	118	0.09	1332
$n=3$	15.9	12.6	12.1	9.6	0.12	81

conditions: $CA^k\vec{x}_{0,1}$, $k \geq 0$, is compared to the transient response measurements starting at $t = 0$; similarly $CA^k\vec{x}_{0,2}$, $k \geq 0$, is compared to the transient response measurements starting at $t = 5$. Residuals are formed from the difference between the simulations and measurements (over the same 3 second data segment used in forming the Hankel matrices), thus, there is a residual associated with $\vec{x}_{0,1}$ and with $\vec{x}_{0,2}$. Since each residual has eight "channels" corresponding to the eight pick-offs for the transient measurements taken at $t = 0$ and $t = 5$, the power spectrum of each channel for each transient record is computed and then summed to a scalar-valued function of frequency –the square root is graphed and compared to the measured baseline noise spectrum, which is aggregated in a similar manner to the residuals for the eight "channels" . The baseline noise spectrum is the same over all tests. In a similar manner, the power in the transient signals are computed for the time intervals starting at $t = 0$ and $t = 5$ (although the transient response of the resonator is not a stationary signal the PSD computation still quantifies its power distributed as a function of frequency over the 3-second interval). In order to have a reasonable degree of smoothing for the relatively short duration data sets, the frequency resolution is only 100 Hz. The power in transient should be much larger than the power in the residual in a neighborhood of the pair of modes under test if the model is accurately reproducing the transient response.

The frequency response of the models is also compared to non-parametric frequency response estimates. The columns of the model's B matrix are determined according to Section 3.2.4 and then the discrete-time frequency response is computed via $C\left(e^{j\omega t_s} - A\right)^{-1} B$, where ω is the frequency variable in units of rad/s and $B = \begin{bmatrix}\vec{b}_1 & \vec{b}_2\end{bmatrix}$. The non-parametric frequency response is estimated from single-input-at-a-time tests using a periodic band-limited chirp excitation signal. The ratio of the discrete Fourier transform (DFT) of one period of

a pick-off measurement to the DFT of one period of the input (applied to either D_1 or D_2) yields the empirical frequency response estimate for the corresponding input-output channel. The non-parametric method includes the effects of input-to-pick-off, or "feedthrough", coupling. The parametric models, however, completely reject any feedthrough and only show components associated with resonator motion.

The feedthrough is largely associated with capacitive coupling between electrodes, and since the input electrodes are driven by buffered voltage sources, the currents picked up by the pick-off electrodes generally increase with increasing frequency. This creates the trend in Figure 1.3 up to the bandwidth of the pick-off buffers which is approximately 30 kHz. The feedthrough can be estimated using the models and measurement data: 1) the model is simulated over the time window that the burst is active; 2) this result is subtracted from the contemporaneous measurement data to produce a short (about τ_b second) record of data that has had the resonator motional component removed; 3) the non-parametric frequency response estimate is applied to this short segment along with the corresponding segment of burst chirp signal. Although the short data records do not give high frequency resolution, this is typically not necessary since the feedthrough is nearly constant in a small neighborhood of the modes. The feedthrough is significant for the $n = 2, 3$ modes and so it is estimated for these cases.

3.3.1 Results for the $n = 1$ modes

The periodic response of the resonator is shown in Figure 3.3 for a subset of pick-offs. The power spectra of the transient, the residual and pick-off noise are shown in Figure 3.4. An interesting feature in the spectra in Figure 3.4 is the presence of the second harmonic near 13 kHz. This harmonic is not captured by the linear resonator model and so the power in the residual and transient data PSDs are equal in a neighborhood of this harmonic. Signed amplitudes and fit sinusoids for the mode pair to determine mode orientation are plotted in Figure 3.5. The modal properties extracted from the identified model are given in Table 3.3

Table 3.3: $n = 1$ modal properties extracted from model

f_1 (Hz)	f_2 (Hz)	τ_1 (s)	τ_2 (s)	ϕ_1 (deg)	ϕ_2 (deg)
6559.17	6604.80	4.66	2.45	7.3	-82.3

and the frequency response of the model and a non-parametric estimate are compared in Figure 3.6.

3.3.2 Results for the $n = 2$ modes

The $n = 2$ pair of modes is an interesting case because this pair has been "tuned" using the algorithm introduced in [BKS17] and deposition technique from [SKS15]. The modal frequencies are very nearly equal and separate resonances cannot be distinguished in frequency response plots. Nevertheless, the modeling technique is able to clearly identify two modes and, importantly, their mode orientations. The periodic response of the resonator is shown in Figure 3.7 for a subset of the pick-offs when $V_{\text{bias}} = 0$.

As a further demonstration of power of the proposed modeling technique, the $n = 2$ modes are perturbed by applying $V_{\text{bias}} \neq 0$. The perturbed modes exhibit small changes in modal frequencies, however, it is shown that the mode orientations are quite sensitive to V_{bias}. Signed amplitudes and fit sinusoids for the mode pair to determine mode orientation are plotted in Figure 3.8. A summary of the modal properties are given in Table 3.4. Figure 3.9 compares the PSD of the residual to the PSD of the transient data when $V_{\text{bias}} = 0$. The frequency response of the model versus a non-parametric estimate is shown in Figure 3.10. Significant feedthrough is evident in certain input-output channels.

3.3.3 Results for the $n = 3$ modes

The response of the resonator to the periodic burst chirp input adapted to excite the $n = 3$ pair of modes is shown in Figure 3.11. The feedthrough coupling is quite evident in the time response. The five largest singular values of $\mathcal{H}_0$ are reported in Table 3.2. Signed

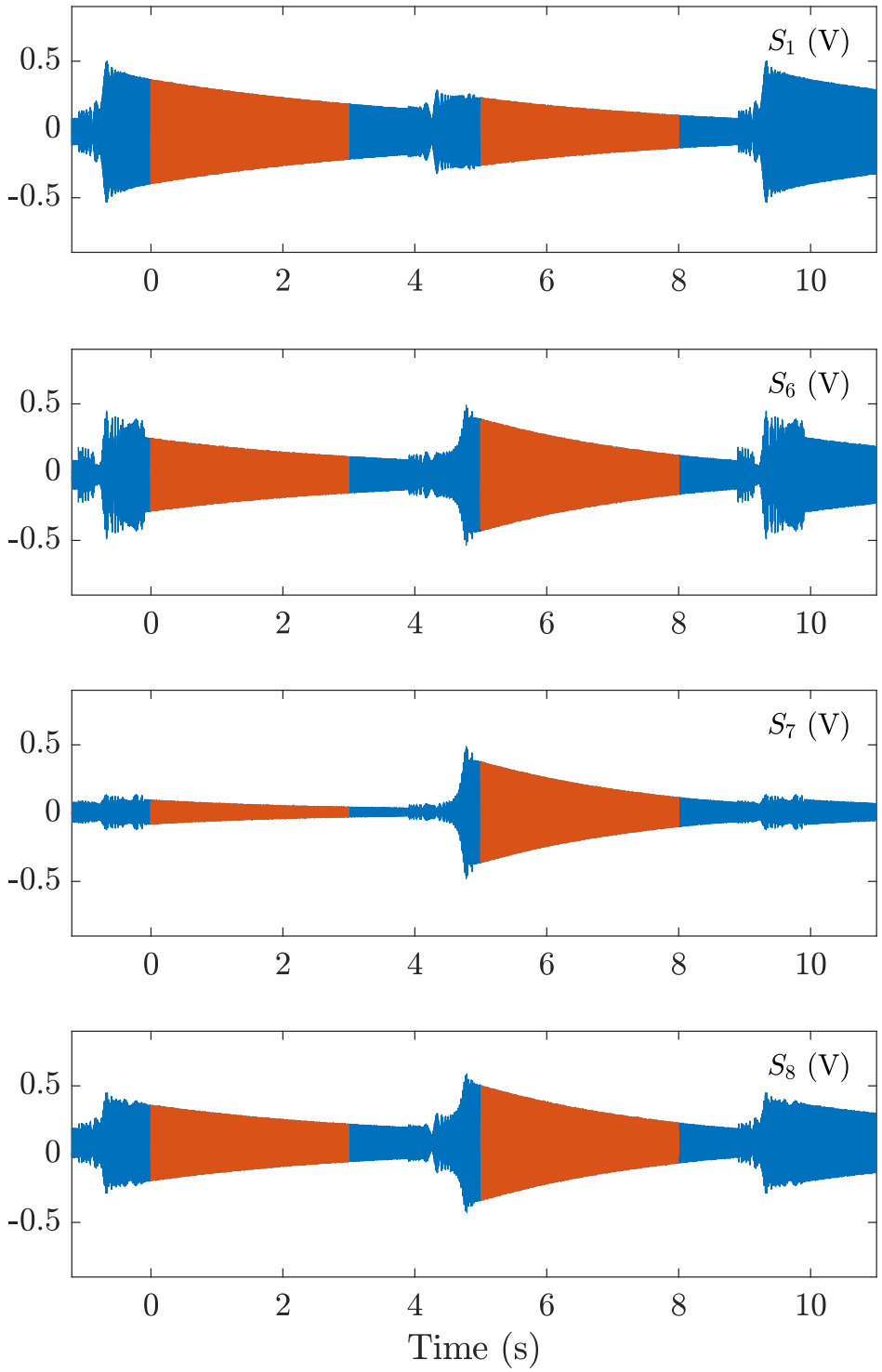

Figure 3.3: Response of $n = 1$ modes to the input in Figure 3.2. Only a subset of the pick-offs are shown (four, out of eight, pick-offs). The data highlighted in red is used to form the Hankel matrices after detrending to remove offsets. The model state $x_{0,1}$ is associated with $t = 0$, while $x_{0,2}$ is associated with $t = 5$.

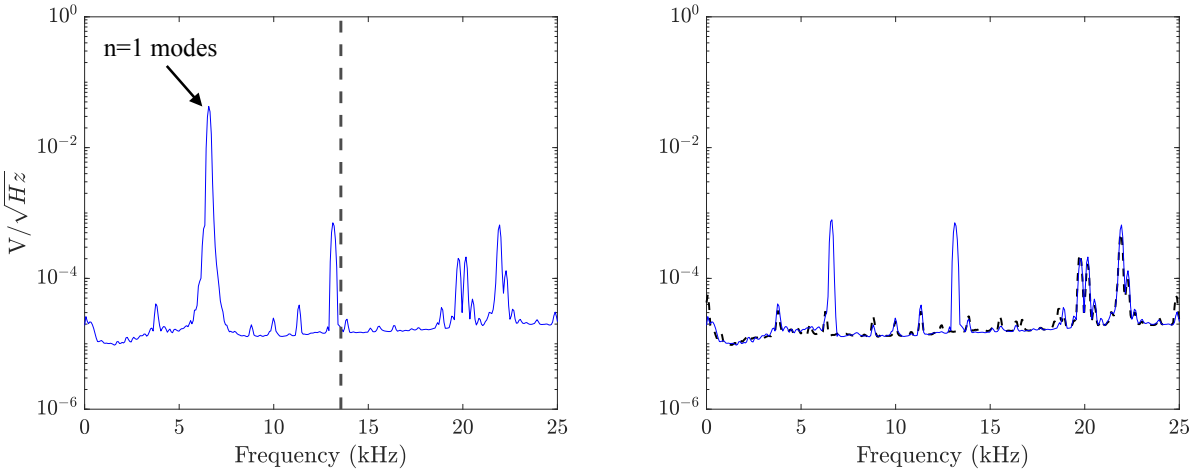

Figure 3.4: (Left) Spectrum associated with the transient data used for model development. The $n = 1$ pair of modes are near 6.6 kHz. A second harmonic is also evident. The dashed vertical line is located at the $n = 2$ modal frequencies. (Right) Spectrum of the residuals compared to the noise floor (dashed). The model has removed significant power from the transient data at the $n = 1$ modal frequencies. The model is linear and does not capture the harmonic distortion near 13 kHz.

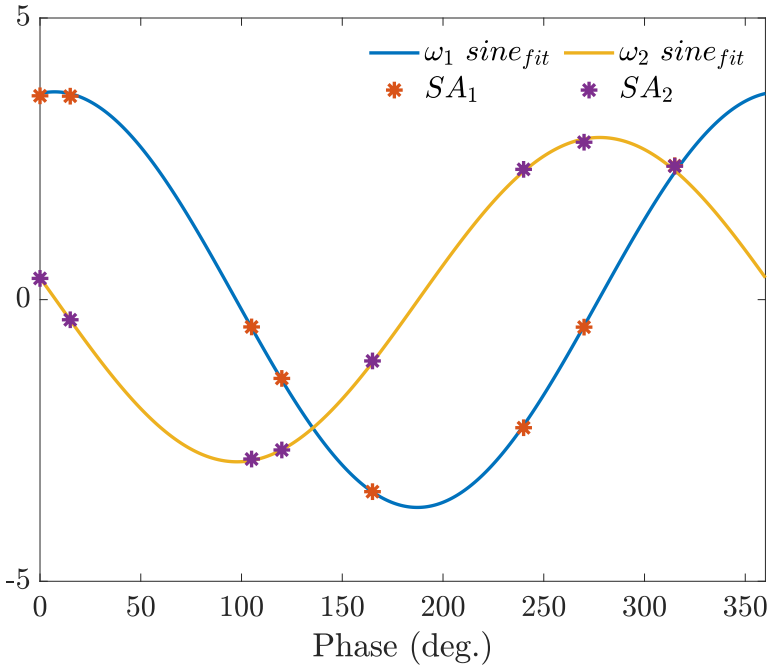

Figure 3.5: $n = 1$ signed amplitudes (stars) and least-squares fit sinusoids (solid) for each mode. Modes are clearly close to 90° apart, consistent with orthogonality for the $n = 1$ mode pair.

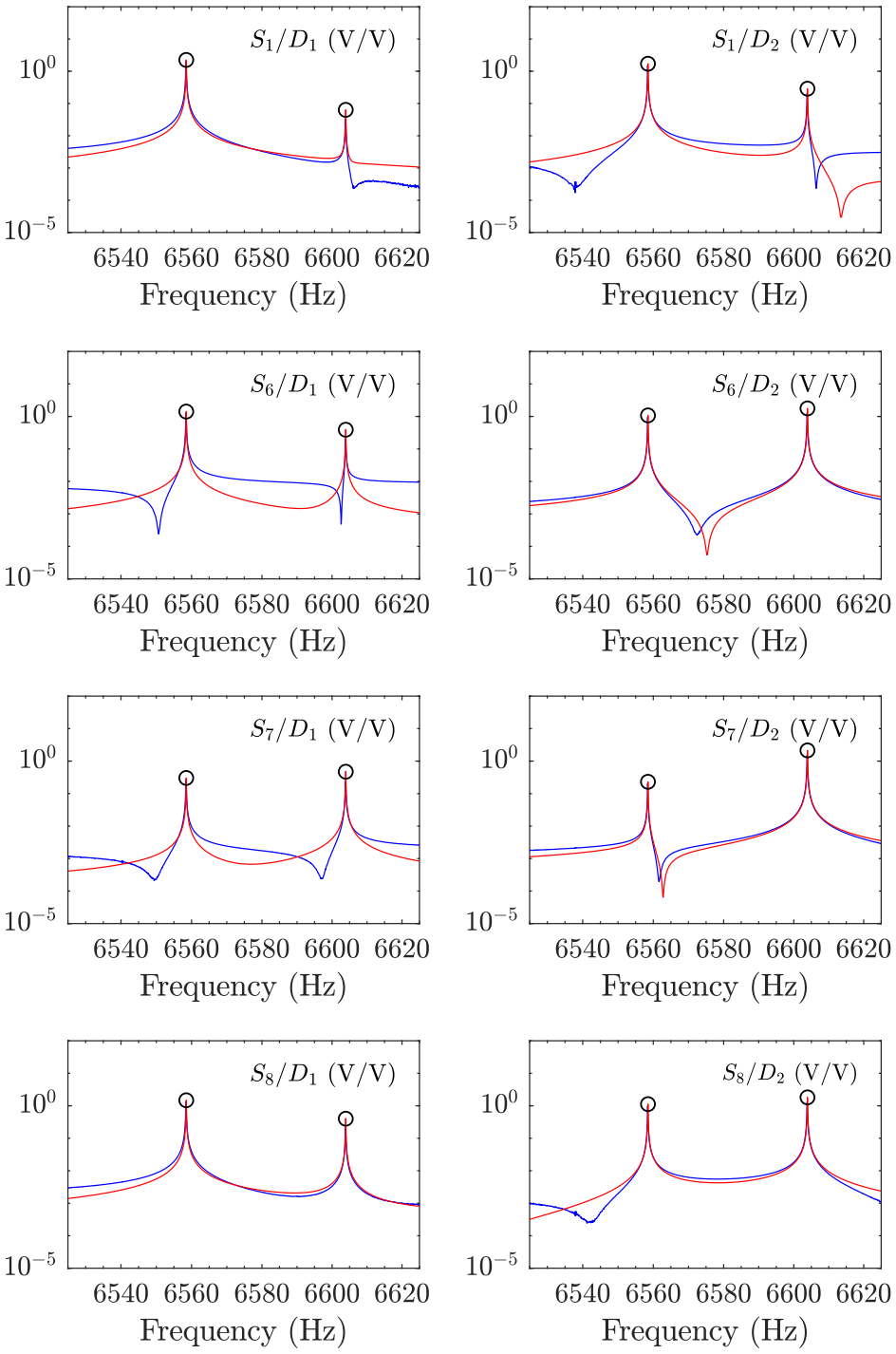

Figure 3.6: Non-parametric frequency response magnitude (dash-dot) is compared to the model frequency response for the $n = 1$ pair of modes. The "○" are derived from analysis of the model's eigenvectors –see Section 3.4.

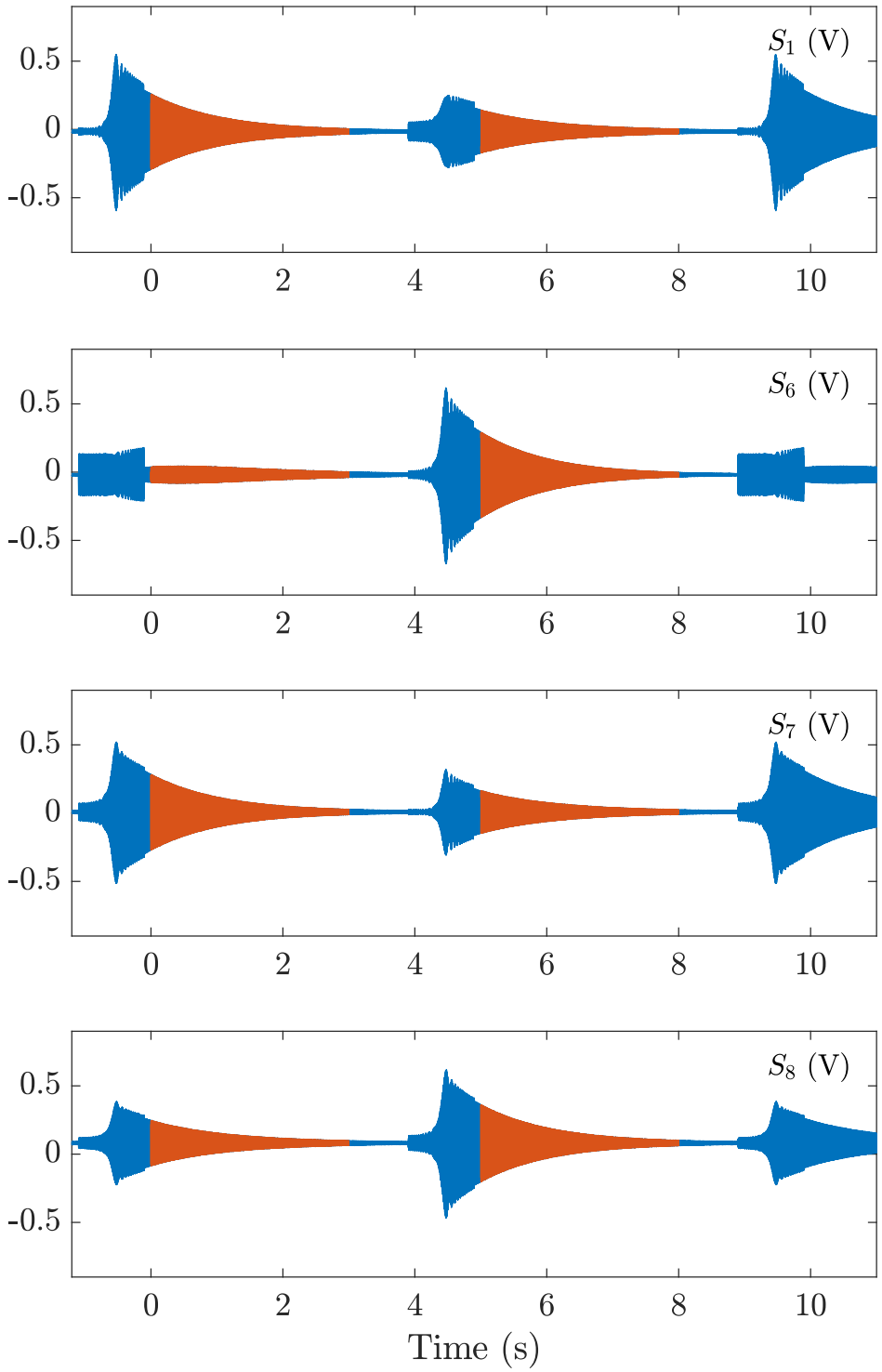

Figure 3.7: Response of $n = 2$ modes to the input in Figure 3.2 when $V_{\text{bias}} = 0$. Only a subset of the pick-offs are shown (four, out of eight, pick-offs). The data highlighted in red are used to form the Hankel matrices after detrending to remove offsets.

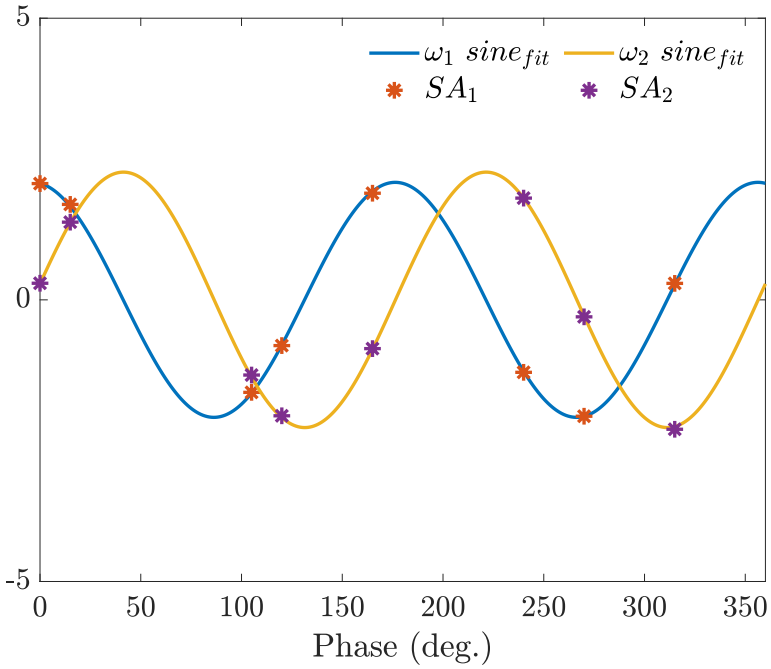

Figure 3.8: $n = 2$ signed amplitudes (stars) and least-squares fit sinusoids (solid) for each mode. Modes are clearly close to 45° apart, consistent with orthogonality for the $n = 2$ mode pair.

Table 3.4: $n = 2$ modal properties determined from model

	V_{bias} (V)			
	0	15	30	45
f_1 (Hz)	13548.95	13548.89	13548.87	13548.79
f_2 (Hz)	13549.04	13548.96	13548.90	13548.85
$f_2 - f_1$	0.09	0.07	0.03	0.06
τ_1 (s)	1.08	1.08	1.08	1.08
τ_2 (s)	1.08	1.08	1.08	1.08
ϕ_1 (deg)	-3.7	-2.3	5.5	31.0
ϕ_2 (deg)	41.4	42.8	50.5	75.8
$\lvert\phi_2 - \phi_1\rvert$	45.1	45.1	45.0	44.8

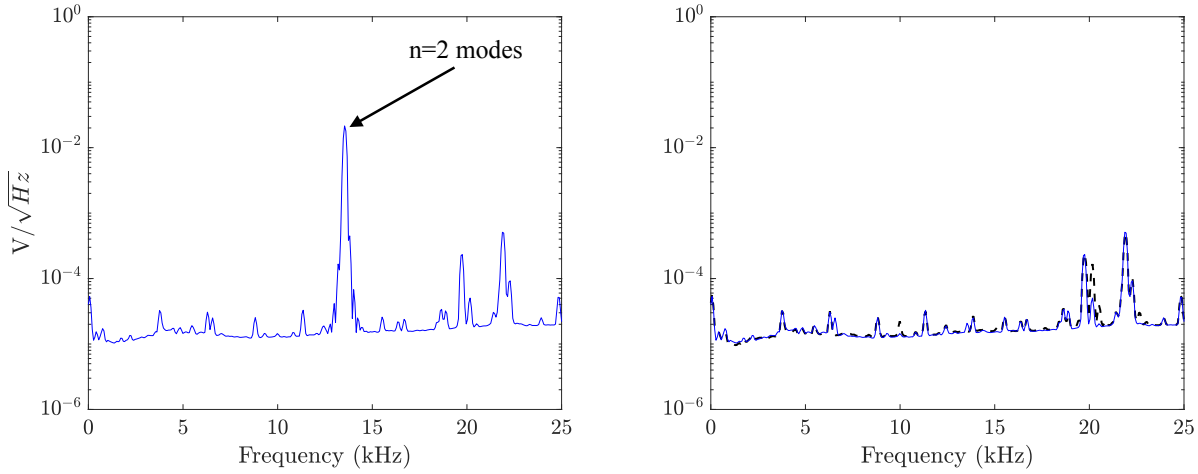

Figure 3.9: (Left) Spectrum associated with the transient data used for model development. The $n = 2$ pair of modes are near 13.5 kHz. (Right) Spectrum of the residuals compared to the noise floor (dashed). The residual spectra are essentially equal to the noise spectrum.

Table 3.5: $n = 3$ modal properties determined from model

f_1 (Hz)	f_2 (Hz)	τ_1 (s)	τ_2 (s)	ϕ_1 (deg)	ϕ_2 (deg)
23867.31	23901.07	0.43	0.43	15.5	-14.5

amplitudes and fit sinusoids for the mode pair to determine mode orientation are plotted in Figure 3.12. A summary of the modal frequencies and mode orientations extracted from the 4-state model are given in Table 3.5. The power spectrum of the residual and transient are shown in Figure 3.13. Finally, Figure 3.14 compares the frequency responses of the model and non-parametric estimate.

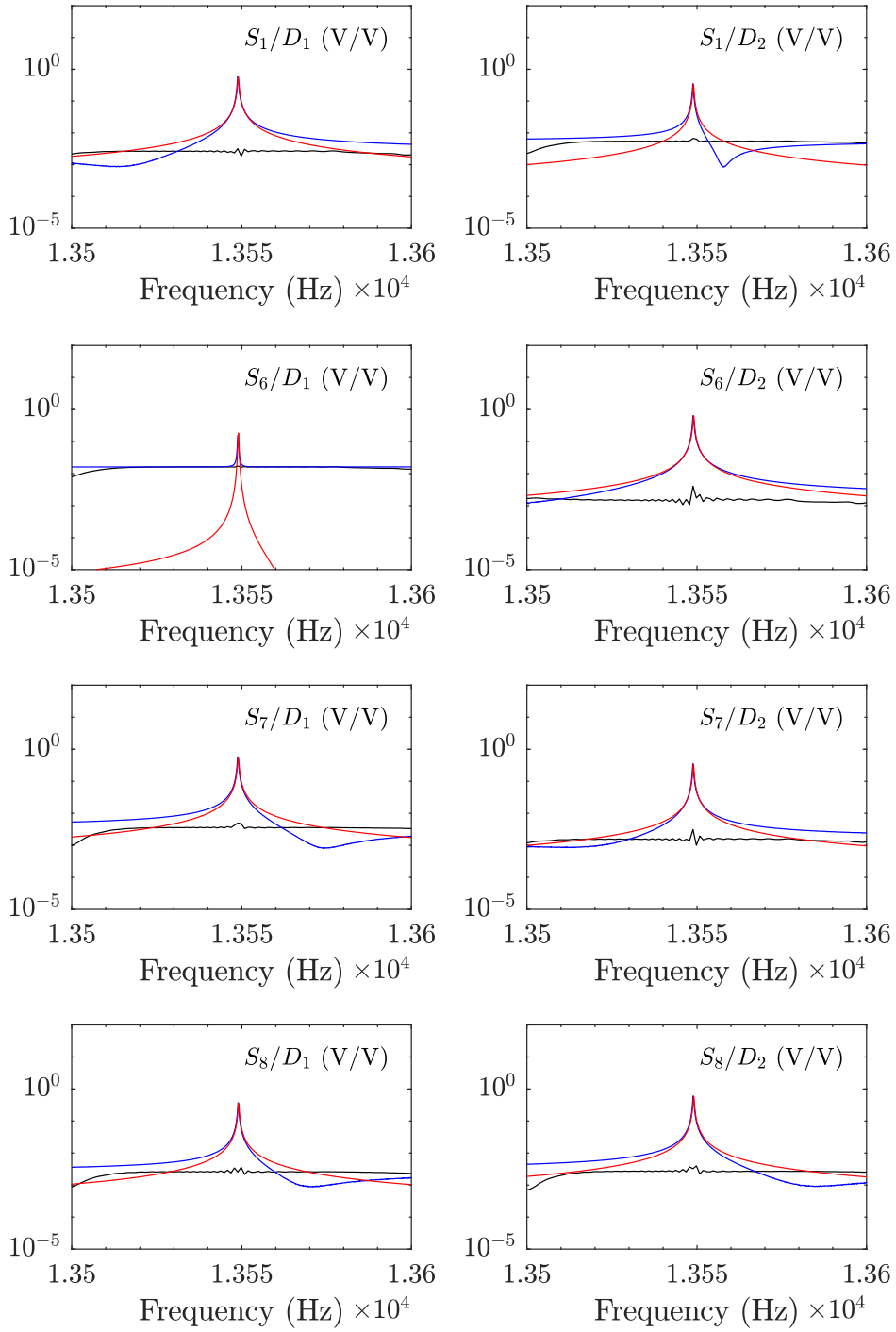

Figure 3.10: Frequency response magnitudes showing the $n = 2$ pair of modes. The non-parametric estimate (dash-dot) has significant feedthrough coupling (estimated shown) in some input-output channels. The model frequency response is not afflicted by the coupling.

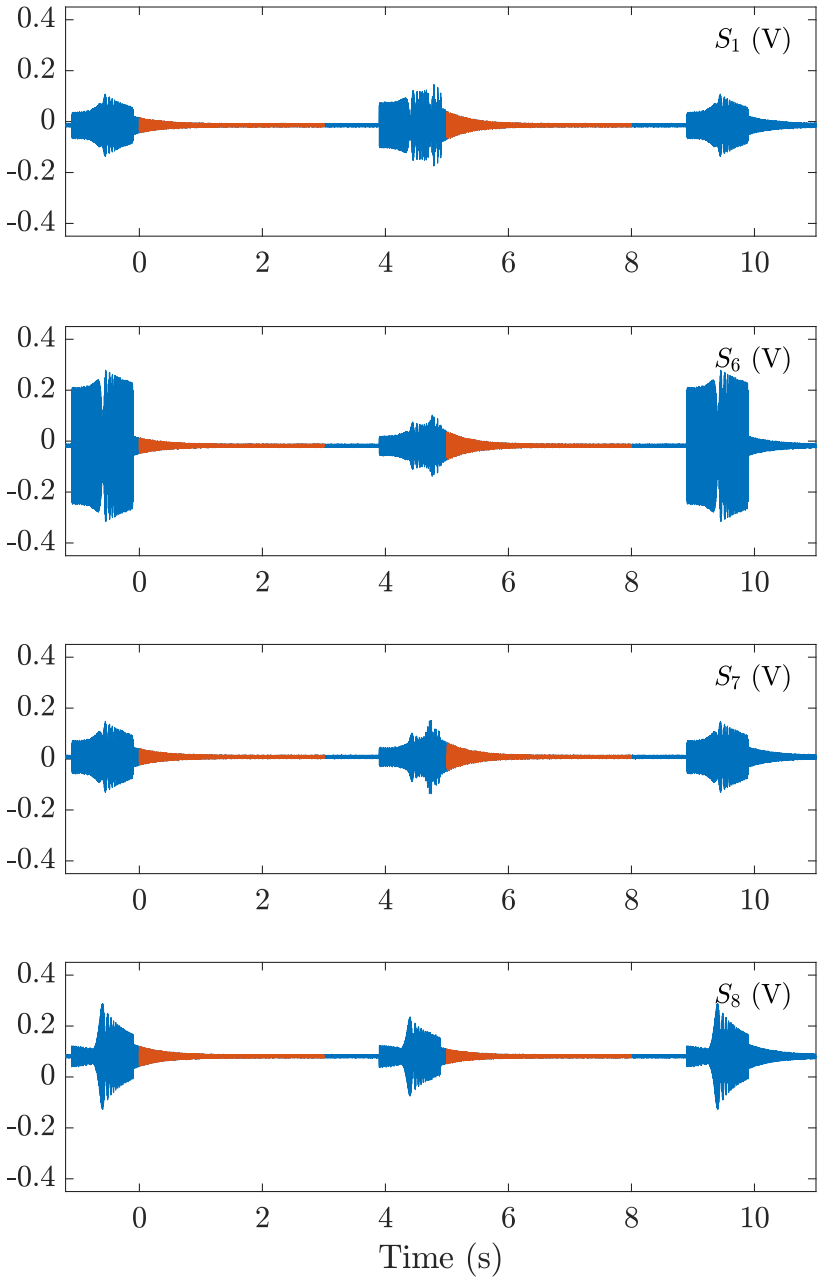

Figure 3.11: Response of $n = 3$ modes to the input in Figure 3.2 when $V_{\text{bias}} = 0$. Only a subset of the pick-offs are shown (four, out of eight, pick-offs). The data highlighted in red is used to form the Hankel matrices. The feedthrough coupling is a significant issue for these modes as evidenced by the measurement values at the times the burst is active, cf. Figure 3.2.

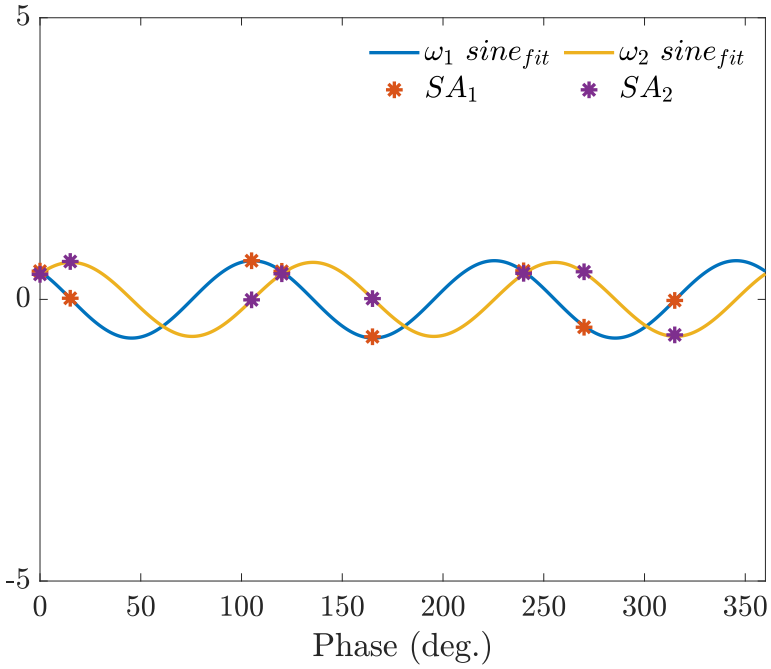

Figure 3.12: $n = 3$ signed amplitudes (stars) and least-squares fit sinusoids (solid) for each mode. Modes are clearly close to 30° apart, consistent with orthogonality for the $n = 3$ mode pair.

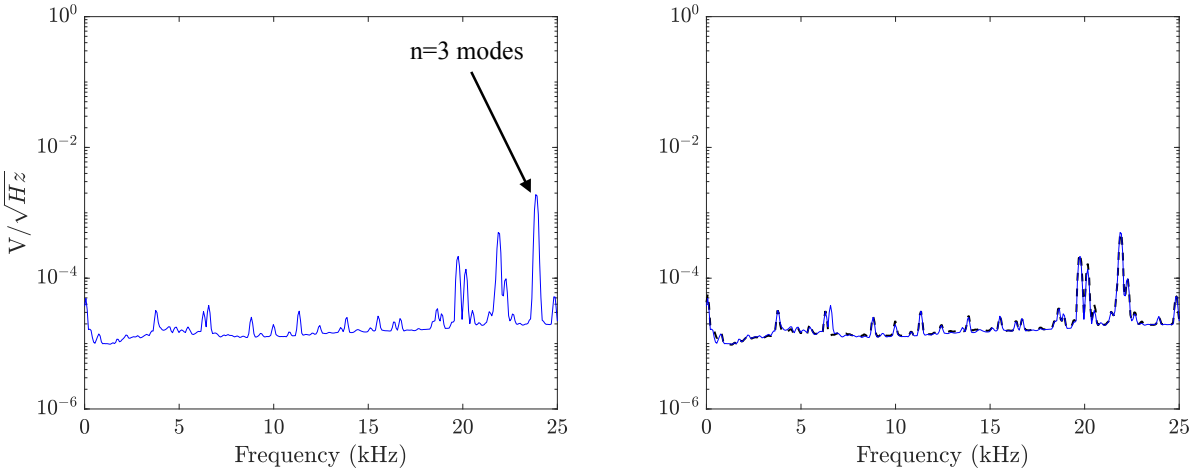

Figure 3.13: (Left) Spectrum associated with the transient data used for model development. The $n = 3$ pair of modes are near 24 kHz. (Right) Spectrum of the residuals compared to the noise floor (dashed).

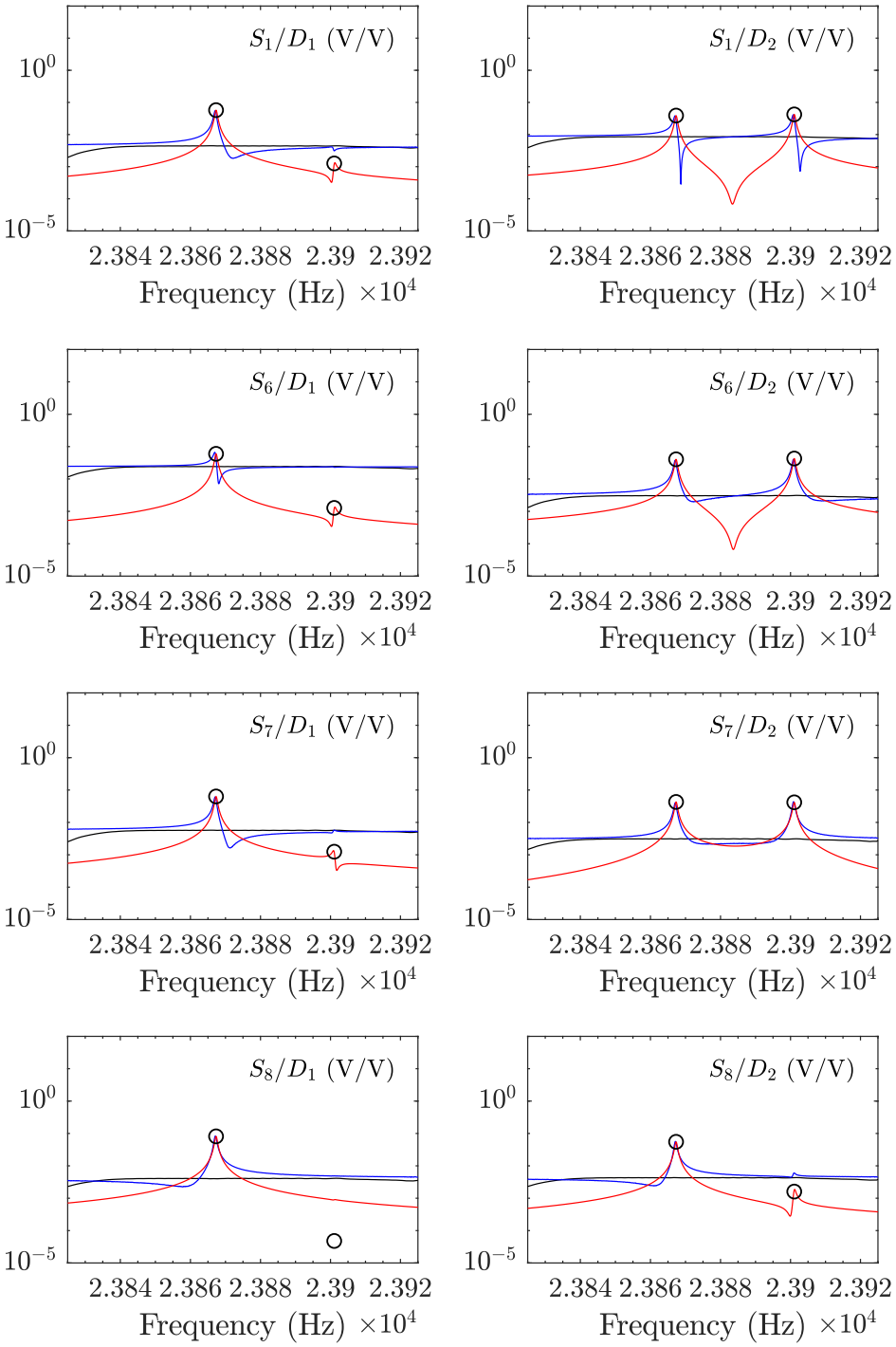

Figure 3.14: Non-parametric (dash-dot) and model frequency response magnitude for the $n = 3$ modes. The estimated feedthrough coupling is also shown. The "○" are derived from analysis of the model's eigenvectors –see Section 3.4.

3.4 Discussion

The veracity of the identified models is confirmed in several ways. First, comparing model and non-parametric frequency responses shows very close agreement between the resonant frequencies and peak magnitude at these frequencies. The model and non-parametric frequency responses differ away from the resonant frequencies, though, because of the feedthrough coupling. Although not shown here, if the feedthrough estimate is summed with the model frequency response, the non-parametric frequency response is recovered.

The mode orientations can also be estimated from the magnitudes of the frequency responses at a given resonant frequency –mapping the magnitudes to the electrode locations gives insight into orientation of the mode under consideration. This approach can only be applied when the modal frequencies are significantly detuned because the two modes respond in an essentially decoupled manner. The model yields mode orientations that are consistent with the non-parametric frequency responses in the $n = 1, 3$ cases. For these cases the elements of $\mathrm{Re}(C\vec{w})$ are graphed in the frequency response plots at the modal frequency corresponding to the eigenvector $\vec{w}$. Since all elements can be scaled by the same factor without changing the mode shape, the scaling is employed to match one element in $\mathrm{Re}(C\vec{w})$ to the frequency response magnitude. Figs. 3.6 and 3.14 show the scaled elements of $\mathrm{Re}(C\vec{w})$ for both modes as the "$\circ$" points –note how all of these amplitude estimates using the eigenvector coincide with the frequency response magnitudes at the resonant frequencies. This confirms that mode orientations derived from the models are consistent with those derived from the frequency response plots.

The spectra of the residuals compared to the noise floor and spectra of the transient data is a measure of how well the model captures the transient response measurements. The residual in the $n = 2, 3$ cases is indistinguishable from the noise floor measurement. In other words, the model has removed any trace of the transient response from the residual. The $n = 1$ residual still shows some power at the modal frequencies but the RMS value of the

residual is more than two orders of magnitude smaller than the transient response RMS value. Also note that the model identifies poorly matched time constants for these modes. The time constant mismatch is not readily apparent from the time domain data because both modes are mixed into each output channel. Although the source of the mismatched time constants has not been identified with certainty, the fact that the $n = 1$ modes are not isolated from the substrate makes them very susceptible to the boundary conditions/mounting method of the die (in contrast, the $n = 2, 3$ pairs are nominally isolated from the substrate). It was mentioned in Chapter 1 that the resonator die is suspended from wire bonds. This mounting method reduces interaction between the die and its supporting substrate when testing the $n = 1$ modes. Although this mounting method produces the longest time constants for the $n = 1$ modes, the time constants are still sensitive to how the wire bonds are attached to the buffer board, e.g., removing and reattaching the die will change the $n = 1$ time constants. The sensitivity of the $n = 1$ modes to its boundary conditions, and the fact that they are very susceptible to vibration imposed on the die, make them unsuitable for exploitation in vibratory gyros, however, they are included here to demonstrate the generality of the proposed modeling method.

Finally, the mode orientations obtained from the models should conform to known properties of modally degenerate ring-type resonators. The mode orientations determined from analysis of the models satisfy $|\phi_1 - \phi_2| \approx 90^\circ/n$ with at most a 0.5° deviation for all of the cases considered in Section 3.3, including the $n = 2$ modes for different values of V_{bias}. This result is consistent with the modal properties of slightly perturbed ring resonators. It is important to note that the model was in no way constrained to enforce a relationship between the orientations of the modes in a given pair –this observation lends considerable credibility to the modeling approach. Further investigation of the $n = 2$ modes yields additional insight. The modal frequencies are weakly perturbed by V_{bias} as shown in Table 3.4 yet the mode orientations are very sensitive to V_{bias}. This behavior is well-known in structural systems with nearly equal eigenvalues: although the eigenvalues are continuous functions

of the perturbation parameter (in this case the "stiffness" created by the electrostatic force gradient when $V_{\text{bias}} \neq 0$), the eigenvectors are generally not continuous functions of the perturbation parameter so it is no surprise that the mode orientations display sensitivity to V_{bias}. The foregoing discussion addresses the ability of the model to provide accurate modal information for degenerate mode resonators.

One outstanding issue is why the first four singular values of $\mathcal{H}_0$ are orders of magnitude larger than the remaining singular values. This fact implies that a model order of four ($n_s = 4$) can accurately represent the transient data. The anticipated *minimum* model order is four because this corresponds to the two oscillator model that is necessary to capture both modes in a degenerate pair, however, the testing block diagram in Figure 3.1 shows that the smoothing and anti-alias filters filters are part of the signal chain that includes the resonator and, thus, their effects are present in the measurements. There are a total of 76 states associated with these filters –each of the eight pick-offs is filtered by an 8-pole anti-alias filter and each of the two resonator inputs is preceded by a 6-pole smoothing filter. Despite the large number of states in these filters, the analysis in Section 3.3 highlights that a 4-state model can very accurately reproduce the transient measurement data.

The truncation of $\mathcal{H}_0$ to a rank 4 matrix preserves the dynamic features that produce the highest energy in the pick-off measurements. These high energy modes are the resonator's modes due to their relatively long time constants when compared to the time constants of the anti-alias and smoothing filters. Nevertheless, the filters do contribute gain and phase shifts to the measurement data and, therefore, must be reflected in some manner in the 4-state models.

Since the Hankel matrix modeling technique produces models that are equivalent to models based on balanced truncation (using finite-time gramians), a realization of the system that includes the four resonator states and the filter dynamics can be transformed into block modal form. Truncating all of the states except the resonator states yields an "A" matrix whose eigenvalues match those of the resonator, however, the magnitude and phase shifts

produced by the smoothing and anti-alias filters in a neighborhood of the resonator modal frequencies are embedded into the B and C matrices of the truncated realization. Thus, the Hankel matrix analysis produces a model in which the resonator modes are faithfully captured, however, the identified B and C matrices include the effects of the input and output filters. Section 3.4.1 below provides additional details and, in summary, proves that the pure resonator system dynamics, H_{res}, can still be recovered even in the presence of input and sensing filters, H_a and H_s.

In the context of a resonator with two (possibly degenerate) modes, 3.4.2 shows that independent burst input sequences will, on average, equally excite both modes in a mode pair, thereby facilitating the identification of vibrational modes from measurements. Section 3.4.2 also highlights that whether the burst is random or deterministic, the two inputs need to be separated in time to generate two separate initial conditions for the transient ring-down model.

3.4.1 Effect of Input and Output Filters

The effects of the smoothing filters located at the resonator input and anti-alias filters located at the resonator output are quantified. It is demonstrated that the identified models have modified C and B such that the magnitude and phase shift introduced by the filters at the modal frequencies is preserved in the identified models. It was shown in [Jon84] that as structural damping approaches zero, balanced coordinates coincide with modal coordinates. The significance of this result is that the Hankel matrix modeling technique produces models that are equivalent to models based on balanced truncation. Thus, since the balanced realization coordinates coincide with modal coordinates as the modal damping is reduced to zero, the system consisting of the resonator and filters can be studied in modal coordinates. Assume that the anti-alias filter, smoothing filter and resonator have models given by $\{A_a, B_a, C_a, 0\}$, $\{A_s, B_s, C_s, 0\}$ and $\{A_r, B_r, C_r, 0\}$, respectively. The discrete-time case is studied, however, the coordinate transformations are identical for continuous-time models.

It is assumed that all subsystems are strictly proper. A realization for the state-space matrix of the series connection of these dynamic elements Figure 3.1 is given by

$$\tilde{x}_{k+1} = \tilde{A}\tilde{x}_k + \tilde{B}u_k,\ y_k = \tilde{C}\tilde{x}_k,$$

where

$$\tilde{A} = \begin{bmatrix} A_a & B_aC_r & 0 \\ 0 & A_r & B_rC_s \\ 0 & 0 & A_s \end{bmatrix},\ \tilde{B} = \begin{bmatrix} 0 \\ 0 \\ B_s \end{bmatrix},\ \tilde{C} = \begin{bmatrix} C_a & 0 & 0 \end{bmatrix}.$$

The vector $\tilde{x}_k$ is a concatenation of the states of the filters and resonator. The "0" blocks represent appropriately dimensioned matrices of zeros. The partitions $\tilde{A}$, $\tilde{B}$, and $\tilde{C}$ are compatible. Define the following matrix

$$T = \begin{bmatrix} I & T_1 & T_3 \\ 0 & I & T_2 \\ 0 & 0 & I \end{bmatrix}$$

where T_1, T_2, and T_3 are solutions to the following Sylvester equations,

$$A_aT_1 - T_1A_r = \quad -B_aC_r, \tag{3.13}$$

$$A_rT_2 - T_2A_s = \quad -B_rC_s, \tag{3.14}$$

$$A_aT_3 - T_3A_s = \quad -B_aC_rT_2. \tag{3.15}$$

The blocks of T are compatible rank wise with $\tilde{A}$. Sylvester equation (3.13) has a solution if the eigenvalues of the A_a and A_r are disjoint. Since the eigenvalues of A_r represent the lightly damped resonator modes and eigenvalues of A_a are the anti-alias filter poles, it is reasonable to assume that the solvability condition is satisfied. A similar argument can be made for (3.14). Sylvester equation (3.15), which involves A_a and A_s, may not have a solution if identical anti-alias and smoothing filters are used, however, for the tests conducted

in Section 3.3, the anti-alias filter poles and smoothing filter poles are disjoint. Assuming the Sylvester equations are solvable, T block diagonalizes A

$$T^{-1}\tilde{A}T = \begin{bmatrix} A_a & 0 & 0 \\ 0 & A_r & 0 \\ 0 & 0 & A_s \end{bmatrix}, \; T^{-1}\tilde{B} = \begin{bmatrix} T_1T_2 - T_3 \\ -T_2 \\ I \end{bmatrix} B_s$$

$$\tilde{C}T = C_a \begin{bmatrix} I & T_1 & T_3 \end{bmatrix}.$$

Modal truncation which retains the dynamics present from the modal portion of the system response produces

$$\{A_r, -T_2B_s, C_aT_1\} \tag{3.16}$$

with corresponding frequency response

$$-C_aT_1(zI - A_r)^{-1}T_2B_s, \; z = e^{j\omega t_s} \tag{3.17}$$

where ω is the frequency variable. The modal truncation doesn't affect the resonator modes, however, the total frequency response is modified by the filters at the input and output. The precise manner in which the frequency response is modified is derived below. The original Sylvester equations can first be manipulated to relate the resonator state space model $\{A_r, B_r, C_r\}$ to the overall identified frequency response model in (3.16). From (3.13),

$$-(zI - A_a)T_1 + T_1(zI - A_r) = -B_aC_r,$$

which is rearranged to

$$-C_aT_1 + C_a(zI - A_a)^{-1}T_1(zI - A_r) = -C_a(zI - A_a)^{-1}B_aC_r. \tag{3.18}$$

Similarly (3.14) yields

$$-(zI - A_r)T_2 + T_2(zI - A_s) = -B_r C_s,$$

which is again rearranged to

$$-T_2(aI - A_s)^{-1}B_s + (zI - A_r)^{-1}T_2 B_s = -(zI - A_r)^{-1}B_r C_s (zI - A_s)^{-1}B_s. \tag{3.19}$$

Left multiplying the right-hand side of (3.19) by the right hand side of (3.18), and similarly, the left hand sides of these expressions, yields

$$\overbrace{C_a(zI - A_a)^{-1}B_a}^{H_a(\omega)}\overbrace{C_r(zI - A_r)^{-1}B_r}^{H_{res}(\omega)}\overbrace{C_s(zI - A_s)^{-1}B_s}^{H_s(\omega)} =$$

$$\underbrace{-C_a T_1(zI - A_r)^{-1}T_2 B_s}_{\text{model from truncation, (3.17)}} + C_a T_1 T_2 (zI - A_s)^{-1}B_s$$

$$- C_a(zI - A_a)^{-1}T_1(zI - A_r)T_2(zI - A_s)^{-1}B_2 + C_a(zI - A_a)^{-1}T_1 T_2 B_s. \tag{3.20}$$

This utility of this relationship is explained. If the resonator has a continuous-time mode $-\alpha + j\omega_n, \alpha > 0$, then A_r has an eigenvalue equal to $\lambda = e^{(-\alpha + j\omega_n)t_s}$ with associated right and left eigenvectors v and u, i.e. $A_r v = \lambda v$ and $u^* A_r = \lambda u^*$ (u^* represents the conjugate-transpose of the column vector u). Let $z = \sigma = e^{j\omega_n t_s}$, localizing the analysis to a neighborhood of the mode. Then,

$$(zI - A_r)^{-1} = \sum_i \frac{1}{z - \lambda_i} v_i u_i^*,$$

which is the spectral decomposition of $(zI - A_r)^{-1}$, and the summation is over all eigenvalues of A_r. $\frac{1}{z-\lambda} vu^*$ dominates relative to all other spectral terms in the summation assuming α is small. Thus,

$$(zI - A_r)^{-1} \approx \frac{1}{z - \lambda} vu^* = \frac{e^{-j\omega_n t_s}}{1 - e^{-\alpha t_s}} vu^*.$$

This expression is unbounded as $\alpha \to 0$, thus

$$\frac{e^{-j\omega_n t_s}}{1 - e^{-\alpha t_s}} vu^* \approx \frac{1}{\sigma} vu^*.$$

The left hand side of the frequency response relation (3.20) is approximated by

$$H_a(\omega_n) H_{res}(\omega_n) H_s(\omega_n) \approx H_a(\omega_n) \frac{1}{\sigma} C_r vu^* B_r H_s(\omega_n), \tag{3.21}$$

and the right-hand side is approximated by

$$-C_a \frac{1}{\sigma} vu^* T_2 B_s + C_a T_1 T_2 (j\omega_n I - A_s)^{-1} B_s - C_a (j\omega_n I - A_a)^{-1} T_1 (j\omega_n I - A_r) T_2 (j\omega I - A_s)^{-1} B_s + C_a (j\omega_n I - A_a)^{-1} T_1 T_2 B_s. \tag{3.22}$$

Assuming there are no transmission zeros in H_a or H_s at λ (this condition is easy to satisfy in practice given the high frequency roll-off associated with the smoothing and anti-aliasing filters) then the dominant terms in (3.21) and (3.22) are the terms containing $(zI - A_r)^{-1}$ and must match. Note that the terms in (3.20) without $1/\sigma$ remain bounded as $\sigma \to 0$. Thus,

$$H_a(\omega_n) H_{res}(\omega_n) H_s(\omega_n) \approx -C_a T_1 (j\omega_n I - A_r)^{-1} T_2 B_s.$$

In other words, the truncated system preserves the magnitude and phase of the smoothing and anti-alias filters for frequencies in a neighborhood of the resonator modal frequencies.

3.4.2 Sufficiency of Model Excitation and Identification

Assume a model of

$$(I + \epsilon M_0)\ddot{x} + \epsilon D_0 \dot{x} + \omega_0^2 (I + \epsilon K_0) x = u,$$

where M_0, K_0, D_0 are all assumed positive definite and M_0, K_0 are assumed symmetric. With the assumption of Rayleigh damping, the damping is then a linear combination of the mass

and stiffness, so the model is then

$$(I + \epsilon M_0)\ddot{x} + \epsilon(\alpha M_0 + \beta K_0)\dot{x} + \omega_0^2(I + \epsilon K_0)x = u,$$

where $\alpha > 0$ and $\beta > 0$ are constants. K_0 and M_0 can be simultaneously diagonalized via the transformation matrix $T = M_0^{-\frac{1}{2}}O$ For the state change $x = Tz$ where $O^{-1}M_0^{-\frac{1}{2}}$ diagonalizes K_0. Applying the transformation yields a new model

$$(I + \epsilon \begin{bmatrix} m_1 & 0 \\ 0 & m_2 \end{bmatrix})\ddot{z} + \epsilon(\alpha \begin{bmatrix} m_1 & 0 \\ 0 & m_2 \end{bmatrix} + \beta \begin{bmatrix} k_1 & 0 \\ 0 & k_2 \end{bmatrix})\dot{z} + \omega_0^2(I + \epsilon \begin{bmatrix} k_1 & 0 \\ 0 & k_2 \end{bmatrix})z = T^{-1}u.$$

Decoupling the system into two systems with $z = \begin{Bmatrix} z_1 \\ z_2 \end{Bmatrix}$ yields

$$(1 + \epsilon m_1)\ddot{z_1} + \epsilon(\alpha m_1 + \beta k_1)\dot{z_1} + \omega_0^2(1 + \epsilon k_1)z_1 = \tilde{u_1}, \tag{3.23}$$

$$(1 + \epsilon m_2)\ddot{z_2} + \epsilon(\alpha m_2 + \beta k_2)\dot{z_2} + \omega_0^2(1 + \epsilon k_2)z_2 = \tilde{u_2}, \tag{3.24}$$

where $\tilde{u_1}$ and $\tilde{u_2}$ are transformed inputs of the original input u applied to the decoupled state system. Begin by looking at the Gramian from the state space equation generated from Equation 1. Let $\tilde{z}_1 = \begin{Bmatrix} z_1 \\ \dot{z_1} \end{Bmatrix}$. Then

$$A_1 = \begin{bmatrix} 0 & 1 \\ -\frac{\omega_0^2(1+\epsilon k_1)}{1+\epsilon m_1} & -\frac{\epsilon(\alpha m_1 + \beta k_1)}{1+\epsilon m_1} \end{bmatrix}, \; B = \begin{bmatrix} 0 \\ 1 \end{bmatrix}.$$

The same approach for $\tilde{z}_2 = \begin{Bmatrix} z_2 \\ \dot{z}_2 \end{Bmatrix}$ yields

$$A_2 = \begin{bmatrix} 0 & 1 \\ -\frac{\omega_0^2(1+\epsilon k_1)}{1+\epsilon m_1} & -\frac{\epsilon(\alpha m_1+\beta k_1)}{1+\epsilon m_1} \end{bmatrix}, \; B = \begin{bmatrix} 0 \\ 1 \end{bmatrix}.$$

Thus, the continuous time solution is described by the initial conditions at the start of the ring-down and the system matrix A, where the aggregate solution $\tilde{z} = \begin{Bmatrix} \tilde{z}_1 \\ \tilde{z}_2 \end{Bmatrix}$.

Let $\tilde{z}_1(0)$ and $\tilde{z}_2(0)$ be the initial conditions describing the ring-down, once the inputs are turned off, for each oscillator described by A_1 and A_2 respectively. Then $\tilde{z}_1 = e^{A_1 t}\tilde{z}_1(0)$ and $\tilde{z}_2 = e^{A_2 t}\tilde{z}_2(0)$.

Constructing the Hankel matrix via simulating the full state at multiple times $t_i, i = 0, ..., n_c$, where n_c is then the Hankel column dimension and $t_0 = 0$, yields

$$M_s = \begin{bmatrix} \tilde{z}_1(0) & e^{A_1 t_1}\tilde{z}_1(0) & e^{A_1 t_2}\tilde{z}_1(0) & \cdots \\ \tilde{z}_2(0) & e^{A_2 t_1}\tilde{z}_2(0) & e^{A_2 t_2}\tilde{z}_2(0) & \cdots \\ e^{A_1 t_1}\tilde{z}_1(0) & e^{A_1 t_2}\tilde{z}_1(0) & \ddots & \\ e^{A_2 t_1}\tilde{z}_2(0) & e^{A_2 t_2}\tilde{z}_2(0) & \ddots & \\ \vdots & \vdots & & \end{bmatrix}.$$

If the modes aren't degenerate then $A_1 \neq A_2$, then the Hankel matrix is full rank. Even with a single initial condition, if the modes are equally excited then the full model will be identified with balanced coordinates.

If the modes are degenerate, then $A_1 = A_2 = A$ and the Hankel matrix is then

$$M_s = \begin{bmatrix} \tilde{z}_1(0) & e^{At_1}\tilde{z}_1(0) & e^{At_2}\tilde{z}_1(0) & \cdots \\ \tilde{z}_2(0) & e^{At_1}\tilde{z}_2(0) & e^{At_2}\tilde{z}_2(0) & \cdots \\ e^{At_1}\tilde{z}_1(0) & e^{At_2}\tilde{z}_1(0) & \ddots & \\ e^{At_1}\tilde{z}_2(0) & e^{At_2}\tilde{z}_2(0) & \ddots & \\ \vdots & \vdots & & \end{bmatrix},$$

where $M_s \in \mathcal{R}^{n_c \times n_r}$. The matrix rank is $\min(n_r/2, n_c/2)$ because clearly each "even" row differs by the previous one by a scalar factor. The chosen row dimension typically is smaller than that associated with the simulation time, i.e. $n_c > n_r$, so the matrix rank is $n_r/2$. Given that the matrix is then "half" rank and in essence the Hankel matrix contains simulation data for the model from one of the two states. The recovered model from the Hankel singular values will then be one oscillator instead of the two identical copies that may be expected from the onset. With a single initial condition for the completely degenerate modes, a one oscillator (one input) model accurately describes the system.

Now assume that the system is still degenerate but has been hit with two inputs that are delayed from one another (the dual input case) so that two different initial conditions can be identified at the beginning of each set of ringdown data. In this case since the two inputs are separated enough both physically and spatially the modes are equally excited. Denote the initial condition at the start of the ring-down for $\tilde{u}_1$ and $\tilde{u}_2$ as $\tilde{z}_1 = \begin{Bmatrix} \tilde{z}_{11} \\ \tilde{z}_{12} \end{Bmatrix}$ and $\tilde{z}_2 = \begin{Bmatrix} \tilde{z}_{21} \\ \tilde{z}_{22} \end{Bmatrix}$. Then the aggregate Hankel matrix for this set of ring-down "dual input" data for the same

simulation time as before is

$$M_d = \begin{bmatrix} \tilde{z}_{11}(0) & \tilde{z}_{21}(0) & e^{At_1}\tilde{z}_{11}(0) & e^{At_1}\tilde{z}_{12}(0) & e^{At_2}\tilde{z}_{11}(0) & e^{At_2}\tilde{z}_{12}(0) & \cdots \\ \tilde{z}_{12}(0) & \tilde{z}_{22}(0) & e^{At_1}\tilde{z}_{12}(0) & e^{At_1}\tilde{z}_{22}(0) & e^{At_2}\tilde{z}_{12}(0) & e^{At_2}\tilde{z}_{22}(0) & \cdots \\ e^{At_1}\tilde{z}_{11}(0) & e^{At_1}\tilde{z}_{12}(0) & e^{At_2}\tilde{z}_{11}(0) & e^{At_2}\tilde{z}_{12}(0) & \ddots & \ddots & \\ e^{At_1}\tilde{z}_{12}(0) & e^{At_1}\tilde{z}_{22}(0) & e^{At_2}\tilde{z}_{12}(0) & e^{At_2}\tilde{z}_{22}(0) & \ddots & \ddots & \\ \vdots & \vdots & \vdots & \vdots & & & \end{bmatrix},$$

where $M_d \in \mathbb{R}^{2n_c \times 2n_r}$ and is generally full rank. With this two input/two output system, two different initial conditions are necessary and sufficient to fully model the two input system, especially as the modes are close to degenerate.

3.5 Zoom Analysis

The Hankel matrices analyzed in Section 3.3 have dimension up to 40×420000 ($n_r = 5$, $n_o = 8$, $n_c = 120000$ and $n_i = 2$). The column dimension must be large in order to faithfully capture the modal time constants. Although an "economy" SVD can efficiently produce the necessary factorization for modeling, it is possible to greatly reduce both the size of the test data sets and dimension of the Hankel matrices without compromising the integrity of the models. The proposed approach is termed "zoom analysis" given its similarity to the signal processing used in "zoom-FFT" spectral analysis [Bro90].

Since the transient response of a pair of degenerate modes is a narrow-band phenomenon, it is possible to downsample the response using demodulation frequency f_0 in a neighborhood of the pair of modes under study. Figure 3.15 illustrates how the sampled resonator output $\vec{y}_k$ is manipulated –it is the same block diagram that is used for standard zoom spectral analysis, however, the downsampled data sequences, denoted $\vec{y}_{c,k}$ and $\vec{y}_{s,k}$ are now used to form $\mathcal{H}_0$ and $\mathcal{H}_1$. The sample period associated with $\vec{y}_{c,k}$ and $\vec{y}_{s,k}$ is $t_D = Dt_s$, where the positive integer D is the decimation factor, and "LPF" denotes unity DC gain low-pass filters that

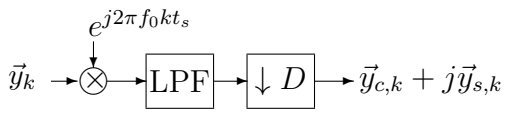

Figure 3.15: Block diagram for zoom analysis. The demodulated signals $\vec{y}_{c,k}$ and $\vec{y}_{s,k}$ are used to form the Hankel matrices, however, the decimation operation greatly reduces the size of the data sets and, thus, the dimensions of the Hankel matrices.

remove the high frequency products. The lower data rate associated with the demodulated signals is where the savings is realized. Since $\vec{y}_k$ is a vector-valued signal, the operations in Figure 3.15 are performed element-wise. Note that the storage requirements are reduced by a factor of $D/2$ because the number of output channels is effectively doubled. Non-parametric zoom-FFT techniques use the spectrum of the demodulated signals to recover the spectrum of the original signals in a neighborhood of ω_0. In the Hankel matrix analysis, though, it is necessary to convert the properties of the identified "baseband" model into properties of the resonator. In view of the modeling results in Section 3.3, it can be assumed that the model generating the transient data is composed of m oscillators and is given by $\vec{y}_k = CA^k\vec{x}_0$, $k \geq 0$, where $A \in \mathbb{R}^{2m\times 2m}$, so $n_s = 2m$ ($m = 2$ for the resonator analyzed throughout this research). The analysis proceeds by representing A in a special basis. Since the system is composed of m oscillators, the eigenvalues of A are given by $e^{(-\sigma_l \pm j\omega_l)t_s}$, $\omega_l > 0$, $l = 1, 2, \ldots, m$, where the exponential decay rate and modal frequency for the l^{th} mode are given by σ_l and ω_l, respectively. Even if there are some repeated eigenvalues, it is assumed that A is non-defective and so A is diagonalizable. Let the columns of $T^+ \in \mathbb{C}^{n_s\times m}$ span the A-invariant subspace associated with the eigenvalues $e^{(-\sigma_l + j\omega_l)t_s}$, $l = 1, 2, \ldots, m$. The complex-conjugate of T^+ is denoted T^-. The columns of T^- span the A-invariant subspace associated with the eigenvalues $e^{(-\sigma_l - j\omega_l)t_s}$. Since these invariant subspaces only intersect at 0, the matrix $T = \begin{bmatrix} T^+ & T^- \end{bmatrix} \in \mathbb{C}^{n_s\times n_s}$ is invertible. The change of basis yields a block diagonal format,

$$T^{-1}AT = \begin{bmatrix} A^+ & 0 \\ 0 & A^- \end{bmatrix}$$

where $A^+ \in \mathbb{C}^{m\times m}$ has eigenvalues $e^{(-\sigma_l + j\omega_l)t_s}$, $l = 1, 2, \ldots, m$, and A^- is the complex

conjugate of A^+ with eigenvalues $\{e^{(-\sigma_l - j\omega_l)t_s}\}$. The measurement sequence from a transient response with initial condition $\vec{x}_0 \in \mathbb{R}^{n_s}$ is

$$\begin{aligned}\vec{y}_k &= CA^k\vec{x}_0 \\ &= CT\begin{bmatrix}(A^+)^k & 0 \\ 0 & (A^-)^k\end{bmatrix}T^{-1}\vec{x}_0.\end{aligned}$$

An expression for the demodulated components of $\vec{y}_k$ is derived. The demodulating sinusoid is assumed to be $\cos(\omega_0 k t_s)$, $\omega_0 = 2\pi f_0 > 0$. In general, the phase of the demodulating sinusoid should be an arbitrary parameter since it is not possible to control the phase relative to the data that is used for forming the Hankel matrices. Including a phase parameter only complicates the analysis without changing the fundamental result, thus, the phase is assumed to be zero as shown. Multiplying $\vec{y}_k$ by the sinusoid yields,

$$\begin{aligned}&\cos(\omega_0 k t_s)\vec{y}_k \\ &= \frac{1}{2}CT\begin{bmatrix}(A^+)^k e^{j\omega_0 k t_s} & 0 \\ 0 & (A^-)^k e^{j\omega_0 k t_s}\end{bmatrix}T^{-1}\vec{x}_0 \\ &\quad + \frac{1}{2}CT\begin{bmatrix}(A^+)^k e^{-j\omega_0 k t_s} & 0 \\ 0 & (A^-)^k e^{-j\omega_0 k t_s}\end{bmatrix}T^{-1}\vec{x}_0.\end{aligned} \tag{3.25}$$

The demodulation frequency ω_0 is selected to be near the set of frequencies $\{\omega_1, \omega_2, \ldots, \omega_m\}$. It is possible for ω_0 to be greater than these frequencies, less than these frequencies, or in the midst of this set. The examples shown below demonstrate that identified modal properties are robust to the choice of ω_0. The low-pass filter is designed so that its corner frequency is greater than $|\omega_l - \omega_0|$, $l = 1, 2, \ldots, m$, so that contributions from all oscillators are preserved in the demodulated signal. Furthermore, D is selected to avoid aliasing. This permits the truncation of the blocks in (3.25) that generate the terms with approximate frequencies $\pm 2\omega_0$ (the eigenvalues of $A^+ e^{j\omega_0 t_s}$ and $A^- e^{-j\omega_0 t_s}$). The decimation operation simply replaces

k with Dk in the right-hand side terms. The sample period of the downsampled data is $t_D = Dt_s$. Thus,

$$\vec{y}_{c,k} = \frac{1}{2} C \Phi^k \vec{x}_0, \tag{3.26}$$

where

$$\Phi := T \begin{bmatrix} (A^+)^D e^{-j\omega_0 t_D} & 0 \\ 0 & (A^-)^D e^{j\omega_0 t_D} \end{bmatrix} T^{-1} \in \mathbb{R}^{n_s \times n_s}.$$

It can be shown that Φ is real if A is real.

Application of the Hankel matrix analysis technique to the demodulated signal $\vec{y}_{c,k}$ will yield estimates for C, Φ and $\vec{x}_0$. Although C and $\vec{x}_0$ are associated with the original system, it is not possible to recover the modal frequencies ω_l, $l = 1, \ldots, m$, from analysis of Φ alone because the eigenvalues of Φ are the set $\{e^{(-\sigma_l \pm j(\omega_l - \omega_0))t_D}\}$ and it is not *a priori* known if the beat frequency $|\omega_l - \omega_0|$ corresponds to a mode whose natural frequency is greater than, or less than, the demodulation frequency ω_0. The ambiguity can be eliminated by considering the demodulated signal $\vec{y}_{s,k}$ in addition to $\vec{y}_{c,k}$.

The expression for $\vec{y}_{s,k}$ is

$$\begin{aligned} \vec{y}_{s,k} &= \frac{1}{2} C T \begin{bmatrix} j(A^+)^{Dk} e^{-j\omega_0 k t_D} & 0 \\ 0 & -j(A^-)^{Dk} e^{j\omega_0 k t_D} \end{bmatrix} T^{-1} \vec{x}_0 \\ &= \frac{1}{2} \underbrace{CM}_{C_s} \Phi^k \vec{x}_0, \end{aligned}$$

where

$$M = T \begin{bmatrix} jI & 0 \\ 0 & -jI \end{bmatrix} T^{-1} \in \mathbb{R}^{n_s \times n_s},$$

and the matrix $C_s \in \mathbb{R}^{n_0 \times n_s}$ is defined as indicated. It is important to express $\vec{y}_{s,k}$ and $\vec{y}_{c,k}$ with the same dynamics matrix Φ because the Hankel matrix analysis is applied to the

base-band system with augmented outputs. The definition of Y_k is updated to

$$Y_k = \frac{1}{2}\begin{bmatrix} C \\ C_s \end{bmatrix} \Phi^k X, \quad k \geq 0$$

where X is the matrix of initial conditions associated with the transients starting at $t = 0$ and $t = 5$ as shown in Figure 3.16. Analysis of the Hankel matrices formed from the demodulated data yield C, C_s, Φ and X.

The modal frequency and damping terms associated with the oscillators are determined as follows. Only a single output is necessary to describe the process so it can be assumed $\vec{y}$, and, hence, $\vec{y}_{c,k}$ and $\vec{y}_{s,k}$, are scalar-valued. Let $\vec{w} \in \mathbb{C}^{n_s}$ be an eigenvector of Φ whose corresponding eigenvalue is $e^{(-\sigma+j\tilde{\omega})t_D}$, where the eigenvalue is chosen so that $\tilde{\omega} > 0$. There are two cases to consider. Suppose the "baseband" frequency $\tilde{\omega}$ is associated with an oscillator whose frequency is greater than ω_0. In other words, $\tilde{\omega} = \omega_l - \omega_0$ for some $l \in [1, \ldots, m]$. In this case the eigenvector $\vec{w}$ may be expressed as $\vec{w} = T^+\vec{z}$ for some unique $\vec{z} \in \mathbb{C}^m$, $\vec{z} \neq 0$. The output matrix associated with the $\vec{y}_{c,k}$ "channel" is C and $C\vec{w} \in \mathbb{C}$ is its product with the eigenvector (since a single output is assumed for this argument). Without loss of generality, it is assumed $C\vec{w} \neq 0$ otherwise the pick-off associated with this output is located at a node of the mode and so no response is observed (another output channel must be selected). Represent $C\vec{w} = \alpha + j\beta$, $\alpha, \beta \in \mathbb{R}$. Now, consider the product of $\vec{w}$ with the output matrix associated with $\vec{y}_{s,k}$,

$$\begin{aligned} C_s\vec{w} &= CMT^+\vec{z} \\ &= jCT^+\vec{z} \\ &= -\beta + j\alpha \end{aligned}$$

Define the matrix $\mathcal{S} \in \mathbb{R}^{2\times 2}$

$$\mathcal{S} = \begin{bmatrix} \mathrm{Re}(C\vec{w}) & \mathrm{Im}(C\vec{w}) \\ \mathrm{Re}(C_s\vec{w}) & \mathrm{Im}(C_s\vec{w}) \end{bmatrix}. \tag{3.27}$$

For the case considered above, namely $\omega_l > \omega_0$,

$$\det \mathcal{S} = \det \begin{bmatrix} \alpha & \beta \\ -\beta & \alpha \end{bmatrix} = \alpha^2 + \beta^2 > 0$$

The second case to consider is when $\tilde{\omega} = \omega_0 - \omega_l > 0$, for some $l \in [1, \ldots, n]$. In this case, the demodulation frequency is greater than the oscillator frequency and the eigenvector $\vec{w}$ can be represented $\vec{w} = T^- \vec{z}$, for some unique $\vec{z} \in \mathbb{C}^m$, $\vec{z} \neq 0$. As before, suppose $C\vec{w} = \alpha + j\beta$ for a new set of $\{\alpha, \beta\}$. Consider,

$$\begin{aligned} C_s \vec{w} &= CMT^- \vec{z} \\ &= -jCT^- \vec{z} \\ &= \beta - j\alpha \end{aligned}$$

In this case, $\det \mathcal{S} = -(\alpha^2 + \beta^2) < 0$. Thus, the sign of $\det \mathcal{S}$ determines whether the modal frequency is less than or greater than the demodulation frequency.

In summary, each output channel is demodulated to produce the baseband signals $\vec{y}_{c,k}$ and $\vec{y}_{s,k}$. A linear model is fit to the baseband data and yields C, C_s, Φ and x_0. Consider an eigenvalue/vector pair of Φ: $e^{(-\sigma + j\tilde{\omega})t_D}$ and $\vec{w}$, for which $\tilde{\omega} > 0$ (since the eigenvalues of Φ appear in conjugate-pairs, m eigenvalues can be chosen to satisfy this constraint). Selecting the same row in C and C_s, $\mathcal{S}$ is computed and the modal frequency of the oscillator is recovered from

$$\omega_0 + \tilde{\omega} \operatorname{sgn}(\det \mathcal{S}), \tag{3.28}$$

where sgn is the signum, or sign, function. This calculation can be performed for each output channel to check consistency of frequency estimates. The exponential decay rate σ is preserved in the demodulated data and so can be directly obtained from the eigenvalue $e^{(-\sigma + j\tilde{\omega})t_D}$.

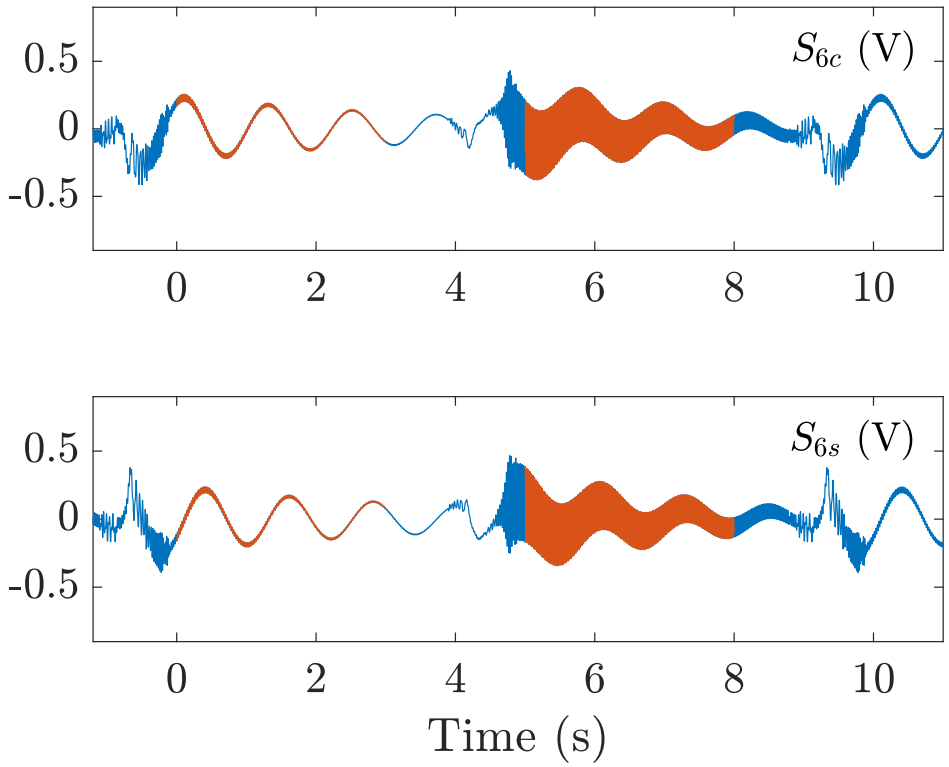

Figure 3.16: An example of the S_6 electrode measurement of the $n = 1$ test from Figure 3.3 demodulated with $f_0 = 6560\,\text{Hz}$ into components $\vec{y}_{c,k}$ (top) and $\vec{y}_{s,k}$ (bottom). The highlighted segments (red) are used to construct the Hankel matrices. The decimation factor is $D = 100$ so the sample period is $t_D = Dt_s = 1/700$ second.

3.5.1 Zoom analysis applied to resonator

The zoom technique is applied to the $n = 1, 2, 3$ resonator modes in order to determine modal frequencies, time constants, and mode orientations. In order to assess consistency with the results presented in Section 3.3, the same data sets are used for the zoom analysis since these data are stored and can be processed according to the zoom method. The low-pass filters are 4-pole Butterworth filters with 200 Hz corner frequencies and $D = 100$. The only parameter that is changed is ω_0 since that is dependent on the which pair of degenerate modes is to be analyzed (ω_0 is reported as f_0, with unit Hz, in the tables). As in the prior analysis, two 3-second transient data segments are used to form the Hankel matrices for $n = 1, 2$, so $n_r = 5$ and $n_c = 2100$, however, $n_o = 16$ because demodulation of $\vec{y}_k$ into $\vec{y}_{c,k}$ and $\vec{y}_{s,k}$ doubles the number of output channels. The dimensions of the Hankel matrices are now 80×4200. For $n = 3$, 1.5 seconds of data are used. An example of the demodulated S_6 pick-off for $n = 1$ is shown in Figure 3.16 (compare to Figure 3.3). The singular values of $\mathcal{H}_0$ are presented in Table 3.6 for three demodulation frequencies applied to each pair of modes. Although the singular values are different from the non-zoom analysis, σ_4 remains more than two orders of magnitude larger than σ_5 so $n_s = 4$ is still a reasonable choice for the model order (demodulation reduces the signal power and this is reflected in the new singular values). Analysis of the Hankel matrices yields Φ, C, C_s and X for each demodulation frequency. The mode orientations can be determined using the process described in Section 3.2.3 with the eigenvectors of Φ without modification. The modal properties determined from the zoom analyses yield the *same* values as quoted in Tables 3.3, 3.4 and 3.5 so no separate summaries for the zoom analyses are required. Note that the modal properties are independent of the choice of f_0.

Table 3.6: Singular values of $\mathcal{H}_0$ for zoom analysis

Pair	f_0 (Hz)	σ_1	σ_2	σ_3	σ_4	σ_5	σ_4/σ_5
	6550	46.0	45.8	30.8	30.7	0.0093	3291
$n=1$	6580	46.0	45.8	30.9	30.6	0.0095	3233
	6610	45.9	45.9	30.9	30.6	0.0093	3280
	13540	21.4	21.1	17.2	17.0	0.0071	2381
$n=2$	13550	22.7	19.8	18.3	15.8	0.0072	2186
	13560	21.4	21.1	17.2	17.0	0.0072	2348
	23860	2.01	1.98	1.58	1.53	0.0079	193
$n=3$	23880	2.04	1.94	1.60	1.51	0.0079	191
	23910	2.03	1.96	1.56	1.55	0.0081	192

3.6 Conclusion

This chapter highlighted the use of a novel method to identify empirical frequency responses in general for any system, but more specifically for a MEM-DRG. By using transient data to fit a state space model using a Hankel matrix based approach, the empirical model is not limited by potential parasitic feed-through. The process is shown to be useful for the n=1, n=2, and n=3 vibratory modes for the DRG, with each mode showing different potential advantages to the modeling process.

Analytical results in this chapter first highlight the need to strategically stagger the burst chirp inputs. Second, the ability for the truncated system to preserve the magnitude and phase of the smoothing/anti-alias filters in a neighborhood of the resonator modal frequencies is derived. In other words in the truncated system, one can decouple the filter and resonator dynamics local to the modal frequencies.

The state space model is so close to the actual transient data that we take it as an "empirical" model. For Chapter 4, where the focus is on the n=2 vibratory modes, this model is optimally converted into a predictive mechanical model for DRGs.

CHAPTER 4

A Mechanistic Modeling Approach for the MEMS Resonator

4.1 Introduction

Chapter 3 establishes a method to extract an accurate state space model for the resonator. Thus, this chapter explores if an improved predictive mechanistic model can be developed to inform mode pair tuning procedures.

Prior predictive models, although physical, only use changes in kinetic energy to inform the tuning process. Although the use of a mass and stiffness matrix for the physical model in this chapter yields more flexibility in terms of a spring energy term, this new physical model, for reasons discussed in Section 4.6, is purely complementary to the prior predictive models used such as that in [BM19], however, this model does benefit from the ability to view prediction results using system frequency responses, which older models do not contain.

4.2 Mechanistic Model Fitting Procedure

Consider a mechanical system modeled by the continuous time equation

$$\begin{aligned} M_l\ddot{x} + D_l\dot{x} + K_l x &= u, \\ y &= C_{1_l} x + C_{2_l}\dot{x}, \end{aligned} \tag{4.1}$$

where u represents the applied stimulus from which y, the pick-off measurements, are obtained for the lth nominal state of the system. $M_l \in \mathbf{R}^{2x2}$ is the mass matrix, $D_l \in \mathbf{R}^{2x2}$ is the damping matrix, K_l is the stiffness matrix, and $C_{1_l}, C_{2_l} \in \mathbf{R}^{8x2}$ encapsulate the dynamics associated with any the pick-off locations and electronics necessary to acquire data from the system. Now consider for this lth state of the system that an empirical frequency response has been obtained, denoted $H_l(\omega) \in \mathbf{C}^{8x2}$. It is then desired to fit the model parameters from (4.1). If the error, at each frequency, indexed by q, in a user defined band where the system dynamics occur, between the determined empirical frequency response and model frequency response is minimized then the obtained model matrices in the system model are considered optimally fit. Let $\tilde{H}_l(\omega_{l,q}) = (C_{1_l} + C_{2_l} j\omega_{l,q})(-M_l\omega_{l,q}^2 + D_l j\omega_{l,q} + K_l)^{-1}$ be the continuous-time frequency response function for the mechanistic model. Now, define $Z_{l,q} = -M_l\omega_{l,q}^2 + D_l j\omega_{l,q} + K_l$ and $R_{l,q} = C_{1_l} + C_{2_l} j\omega_{l,q}$ as the "denominator" and "numerator" of the frequency response function. The error reduction between H_l and $\tilde{H}_l$ for each $\omega_{l,q}$ to optimally fit the model parameters can be accomplished by solving the following.

$$\min_{\substack{M_l > I, D_l \in \mathbf{R}^{2x2}, \\ K_l > 0, C_{1_l}, C_{2_l} \in \mathbf{R}^{8x2}}} \max_{q=1,\ldots,m_l} \sigma(R_{l,q} - H_l(\omega_{l,q}) Z_{l,q}),$$

where σ represents the singular value of the multi-dimensional frequency response and m_l is the total number of frequency points considered for the optimization in the user defined grid. This optimization problem is non-convex, however, an equivalent formulation is found of a more standard generalized eigenvalue minimization problem with LMI constraints via Schur's complement.

$$\begin{aligned} &\min_{\gamma > 0} \gamma, \\ \text{sub. to} &: J_{l,q} > 0 \; \forall \; q \\ &M_l > I, D_l \in \mathbf{R}^{2x2}, \\ &K_l > 0, C_{1_l}, C_{2_l} \in \mathbf{R}^{8x2}, \end{aligned} \tag{4.2}$$

$$J_{l,q} = \begin{bmatrix} \gamma I & (R_{l,q} - H_{l,q}Z_{l,q})^* \\ (R_{l,q_k} - H_{l,q}Z_{l,q}) & \gamma I \end{bmatrix},$$

where $(\cdot)^*$ is the complex conjuate operation. It is possible to optimally fit model parameters simultaneously based on multiple sets of nominal resonator state data. In that case l is the index denoting the current nominal state of the resonator. Only one nominal state of the resonator is fit at a time to then be used for point mass predictions. The optimization is solved using programs such as those in MATLAB's Robust Control Toolbox, so long as the constraints are real-valued. Details of transforming the positive-definiteness of the complex-valued constraint $J_{l,q}$ to one that is real-valued are briefly discussed. An analog to $J_{l,q} > 0$ must be formed. Ann equivalent formulation of the above inequality is

$$\begin{bmatrix} Re(J_{l,q}) & Im(J_{l,q}) \\ -Im(J_{l,q}) & Re(J_{l,q}) \end{bmatrix} > 0.$$

Expanding and then constructing the above matrix yields an equivalent positive-definiteness constraint on $J_{l,q} > 0$.

Intuitively, it should be easier to determine the effect of a mass or stiffness perturbation to the system with a model of this form. The next section focuses on determining a functional form of the perturbed mass matrix when a small mass perturbation is added to a MEM-DRG. The experimental results for the $n = 2$ vibrational mode are then given in the subsequent section, highlighting the model's predictive efficacy.

4.3 Predictive Resonator Model

4.3.1 Resonator Description

Although the fitting procedure is general for any mechanical linear system, the MEM-DRG, with schematic shown in Figure 1.1, will be used due to the existence of vibrational mode

pairs, ideally modally degenerate but realistically not. The outer ring layers, where a total of 96 potential point mass perturbations can be placed are ordered from $k = 1$ (innermost ring layer) to $k = 4$ (outermost ring layer). Other details such as experimental conditions are highlighted in Section 1.2.

4.3.2 Eigensystem Analysis of Mass Perturbations on the Uniform Thin Ring

Once the resonator system model matrices for the lth experiment are optimally fit, the key next step is to establish a way to accurately predict changes to the model when point masses are added to the resonator at various specified locations around the resonator in the analytical form of a change in mass matrix before and after a mass perturbation is placed as a function of the point mass placement θ. This is accomplished first in Chapter 2 via analysis of a uniform thin ring and then in Section 4.3.3 by extending the ring analysis to the resonator, which can be modeled using various superposed thin rings with finite element analysis in COMSOL as a guide.

Plugging into the form of Δ_M obtained via Galerkin Analysis in Chapter 2 for the $n = 2$ vibrational mode yields

$$\Delta_M = \Gamma_2 \begin{bmatrix} \frac{5}{8} + \frac{3}{8}\cos(4\theta) & \frac{3}{8}\sin(4\theta) \\ \frac{3}{8}\sin(4\theta) & \frac{5}{8} - \frac{3}{8}\cos(4\theta) \end{bmatrix}. \tag{4.3}$$

It is crucial to generalize this analysis to a case where the nominal state of the ring isn't uniform. That analysis seen in Chapter 2 is expanded upon here. For this nominal state of the ring, the modes are detuned and there are two distinct modal frequencies (ω_1, ω_2) and eigenvectors v_1, v_2. The generalized eigenvalue problem (assuming negligible damping) is as follows with a point mass placed along the ring at θ with a to be determined perturbation

$\tilde{\Delta}_M(\theta)$ to the nominal mass matrix M:

$$\omega_i^2(M + \tilde{\Delta}_M(\theta))v_i = Kv_i, \quad i = 1, 2.$$

The mass matrix and stiffness matrix are assumed to be perturbed from scalar times identity by a series of small mass perturbations placed throughout the ring and small ring width perturbations, both of which are of order ϵ_M, ϵ_K. It is reasonable to assume that $M \approx mI$, $K \approx kI$. In all experimental models fit shown in this study, the mass and stiffness matrices relatively differ from scalar times identity by roughly 3 percent at most, so this is a valid assumption. Thus the eigenvalue problem is

$$\omega_i^2(mI + \tilde{\Delta}_M(\theta))v_i = kIv_i, \quad i = 1, 2. \tag{4.4}$$

It is clear that $\tilde{\Delta}_M(\theta) = \Delta_M(\theta)$ from (4.3). This result, given the assumptions, is important for a few reasons. First, (4.3) gives a functional form for the perturbation to a mass matrix when a point mass is placed anywhere on a potentially non-uniform thin ring. Second, the analysis in Section 2.3 shows that the mass matrix perturbations are additive for multiple point masses. Thus, for a nominal ring state (M, K), the post-perturbation mass matrix $\tilde{M} = M + \sum_{i=1}^{p} \Delta_M(\theta_i)$, where p is the total number of point masses placed on the ring and θ_i is the orientation of the ith point mass.

4.3.3 Multi Layered Ring-Resonator model

The model is extended to resonators for multiple point masses, which generalizes the single point mass term into a summation over multiple ring spoke layers, as seen in Figure 1.1. For each layer index k the radial and tangential velocity amplitudes α_k and β_k scale.

The full FEM analysis for this ring-type resonator design is shown in Figure 4.1 and is also seen in [BM19, Beh18].

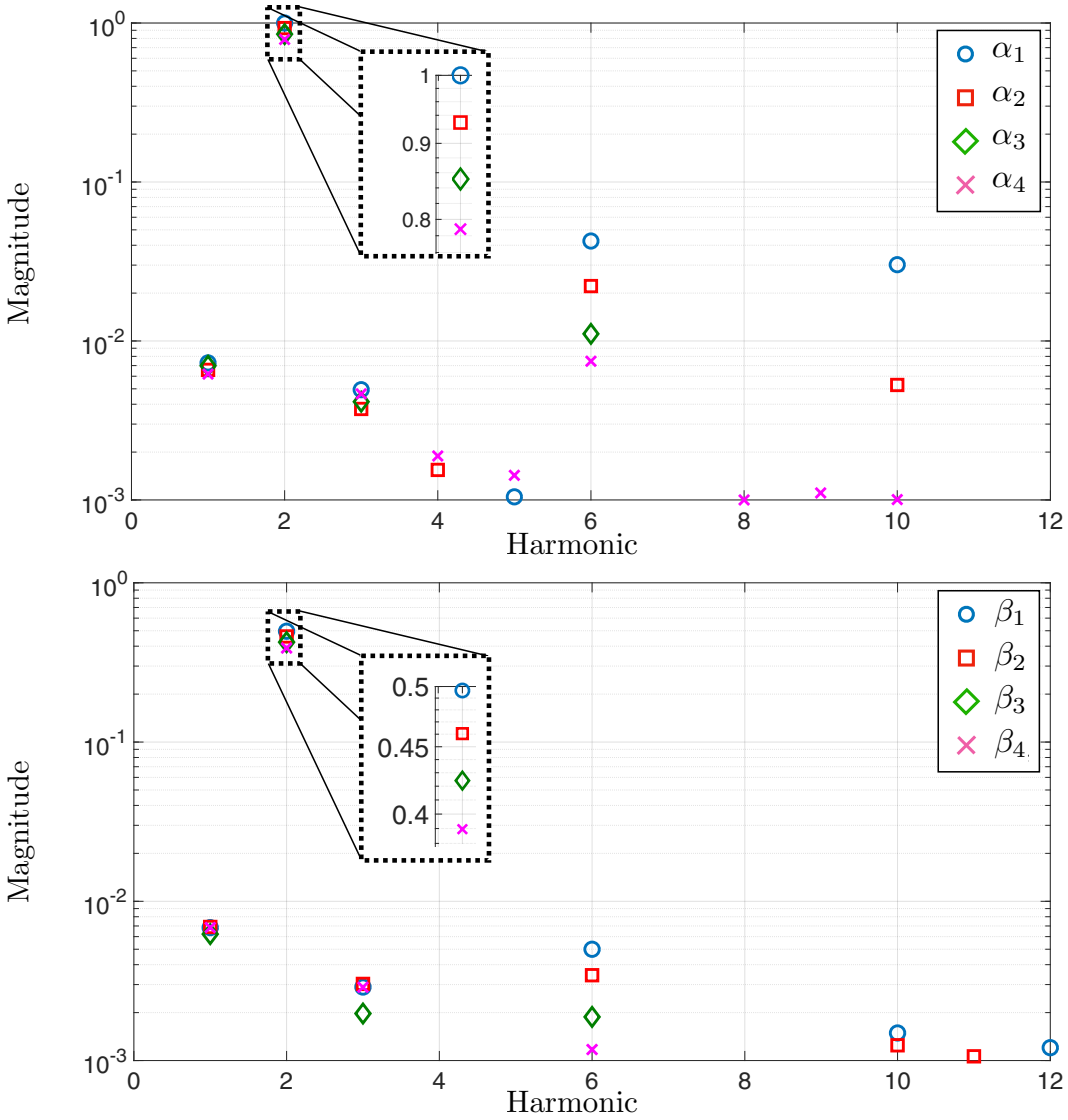

Figure 4.1: Finite Element Analysis for ring-type resonator showing non-negligible contribution magnitude of $n = 6$ and $n = 10$ modal radial (top) and tangential (bottom) velocity FS coefficients to $n = 2$ modal velocity amplitudes, significantly in innermost layers

For the $n = 2$ mode, the 6θ and 10θ harmonics of the Fourier Series coefficients for the spoke radial velocities are non-negligible, especially as you look at the innermost layers. In other words, based on this model, the predictions will have low variance for the outermost ring layers and higher variance for the innermost ring layers. Further analysis on these added harmonics is performed for the innermost two layers in Section4.6.3.

The velocity amplitudes derived from finite element analysis performed in [BM19] for the

$n = 2$ mode in this resonator design are highlighted in Table 4.1

Relative Velocity Amplitudes for $n = 2$		
Ring layer k	α_k	β_k
k = 1	1.0000	0.4949
k = 2	0.9289	0.4603
k = 3	0.8506	0.4214
k = 4	0.7868	0.3886

Table 4.1: Velocity amplitudes are normalized to the radial velocity amplitude for inner layer k=1 and are computed via finite element analysis

The pair (k,i) represent both a layer and orientation, i.e. a spoke location, for mass deposition. Based on the velocity amplitudes in Table 4.1, the sensitivity γ_1 is related to the change in the frequency split if the reference mass m_0 is placed on the anti-node of the innermost spoke layer ($k = 1$). If mass is deposited at an anti-node, then the change in frequency split (frequency increase if placed on lower frequency anti-node and decrease if placed on higher frequency anti-node) is

$$\gamma_k = \gamma_1 \frac{(\alpha_k^2 - \beta_k^2)}{(\alpha_1^2 - \beta_1^2)}. \tag{4.5}$$

The focus of this work is on the $n = 2$ vibratory mode so the n portion of the subscript is dropped for the remainder of this chapter.

The point mass sensitivity for a layer k in [SKS15] is defined as $\gamma_k = \tilde{\Delta} - \Delta$, which has units of Hz, where Δ is the nominal modal frequency split, and $\tilde{\Delta}$ is the modal frequency split after a single point mass has been applied on ring layer k. Of note is that this sensitivity does not vary along a particular ring layer, however, experimentally this value is determined by a series of single mass depositions where the value of γ_k can be determined via an average.

In this modeling process, the coordinate frame is established by the placement of the sense channels around the ring and the set of orthogonal inputs, designating generalized system inputs.

In this mechanistic model, the analog to a sensitivity γ_k is $||\Delta_{M,k}||$, where $||\cdot||$ refers to the matrix Frobenius norm. $\Gamma_k := ||\Delta_{M,k}||$ is proportional to the sensitivity and is dependent on ring layer k. Γ_k can be apriori determined analytically after the modal properties of a resonator without point mass adjustment is measured. Thus $\Delta_{M,k}$ can be rewritten as a constant multiplying a norm 1 matrix, i.e. $\Gamma_k \Delta_M$ for each point mass perturbation, where Δ_M is the analytical form of the change to the mass matrix derived in the prior section for a thin ring and Γ_k is the norm of Δ_M that varies based on spoke layer k. The matrix norm is obtained in the following manner:

For this particular resonator design, γ_1 was experimentally determined for a particular type of solder sphere in [BM19]. (4.5), in addition to a ratio of densities of solder sphere used in this study over the prior study, converts the sensitivity to that used in this study for the outermost ring layer, having the least experimental variance. Γ_4 is then determined for four single mass depositions in the outermost layer by iterating Γ_4 until the predicted and computed sensitivities match. This is then normalized by its nominal mass matrix norm $||M_l||_2$ so that the averaged Γ_4 represents the norm of Δ_M when the nominal mass matrix has unit norm. Converting between Γ_4 and Γ_k for another ring layer k is the same as the conversion for the sensitivity in (4.5).

Predicting the state of a resonator via the mechanistic model with an empirically obtained Γ_k is then straightforward based on the prior analytical and ring-resonator FEM results:

$$M_{l+N}\ddot{x} + D_l\dot{x} + K_l x = u, \tag{4.6}$$

$$y = C_{1_l} x + C_{2_l}\dot{x}, \tag{4.7}$$

where l is the index for the pre-perturbation experiment/state of a single resonator. $M_{l+N} = M_l + \sum_{i=1}^{96} \mu_i ||M_l|| \Gamma_{k(i)} \Delta_M(\theta_i)$, and $\sum_{i=1}^{96} \mu_i = N$, where N is the total number of point masses for which a prediction is made, i is the position on the resonator where a point mass could be placed, θ_i is the angle where a point mass is placed on the as a function of position

i, where μ_i is 1 if a point mass is placed at location i and 0 otherwise, and the $||M_l||_2$ factor multiplying $\Gamma_{k(i)}$ is compensating for the step taken in the computation of Γ_k, ensuring that Δ_M is normalized for a mass matrix close to identity with unit norm.

4.4 Application to Resonator

4.4.1 Two Step Model Fitting

The process to fit the predictive model contains two primary steps. More information is contained in the prior Chapter 3, but important details are reviewed here. First, a ring-down model is fit for the system localized to the $n = 2$ mode. For any nominal state of the resonator, the discrete-time linear state-space model for that mode takes the form below for a particular vibratory mode.

$$\begin{aligned} \vec{x}_{k+1} &= A_l \vec{x}_k + B_l \vec{u}_k, \\ \vec{y}_k &= C_l \vec{x}_k, \end{aligned} \tag{4.8}$$

where $A_l \in \mathbf{R}^{4x4}, B_l \in \mathbf{R}^{8x2}, C_l \in \mathbf{R}^{8x4}$, and $\vec{y}_k \in \mathbf{R}^{8x1}$ represents the pick-off measurements in response to the applied stimulus $\vec{u}_k \in \mathbf{R}^{2x1}$, specifically each input contained in $\vec{u}_k$ is fed a chirp focused in a frequency range containing the modal peaks, turned on for 1 second, followed by 9 seconds of no input for a total period of 10 seconds, however, each unique input is time delayed by five seconds relative to the other. The state space model fit from empirical transient data accurately describes the system without parasitic feed-through effects, and thus can be effectively used to both fit and to check the predictive capabilities of the mechanistic model, i.e. as an empirical model. To that effect, it is necessary to extract the modal properties inherit to the $n = 2$ vibrational mode. A_l and C_l matrices can be analyzed for modal frequencies, damping and mode orientation. Since the identified model is obtained by sampling a continuous-time system with sample period t_s, a mode with exponential decay

rate $\sigma\,(\mathrm{s}^{-1})$ and modal frequency $\omega_n\,(\mathrm{rad/s})$ will be associated with eigenvalues of A_l of the form $e^{(-\sigma\pm j\omega_n)t_s}$. Analysis of the eigenvalues of A_l yield the modal frequencies and time constants and the mode orientation can be determined from the eigenvectors of A_l.

$H_l(\omega) = C_l(e^{j\omega t_s}I - A_l)^{-1}B_l$ is therefore the empirical frequency response used to fit the nominal predictive model matrices. Figure 4.2 below shows the mechanistic model relative to empirical frequency response data for a representative nominal state of the resonator focused on the $n = 2$ modes. A linear chirp signal with 0 to 30 kHz band over a ten second period sent to a single input at a time yields the empirical data. These are plotted for the S_4/D_1 and S_5/D_1 channels only. Present in the empirical data especially for S_5/D_1 is capacitive feed-through, which the modeling process inherently removes. Also plotted is the relative error between the transient based state space and predictive models. To effectively compare these models define $\bar{\sigma}(H_l(\omega) - \tilde{H}_l(\omega))/\bar{\sigma}(H_l(\omega))$, where $\bar{\sigma}$ is the max singular value of the system's MIMO frequency response, as a relative error varying as a function of frequency between the ring-down and predictive models. The maximum over all frequencies in the band of interest for all nominal states of the resonator is no larger than one percent.

4.4.2 Discrete Time State Space Model to Continuous Time Mechanistic Model

The modeling process for the system at hand is discussed, leading to rationalization for purely fitting a continuous time mechanistic model from the discrete time state space model.

For the initial state space discrete time model, the block diagram in Figure 3.1, where H_s, H_a and H_sys represent smoothing filters, anti-alias filters, and the system under test, respectively. Any onboard electronics for the forcer and pick-off channels are aggregated in the smoothing and anti-alias filters respectively. The DAC implements a zero-order hold on the discrete-time signal u and the ADC blocks sample the continuous-time signals to yield the discrete-time signal y. A discrete-time model of the form (4.8) describes the relationship between the input-output samples and the state variable x [AW11] assuming all dynamic elements in the block diagram are linear.

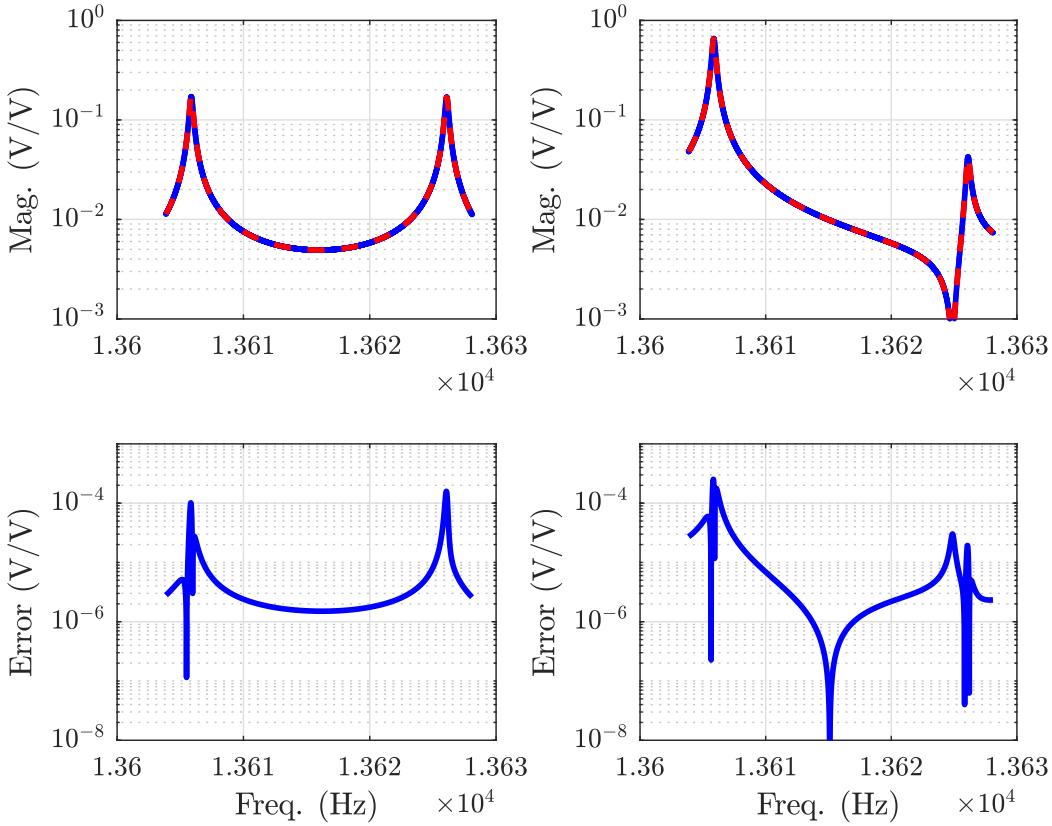

Figure 4.2: (top) The predictive model (solid) and empirical (dashed) frequency responses for single pick-off (S6)/dual forcer channels of interest and (bottom) relative error between transient and predictive models are shown for a "nominal" state of the resonator $n = 2$ mode pair after some mass has been loaded on the resonator, highlighting the veracity of the predictive model fit to the state space system model.

The state variables for the lth experiment are then denoted with the triplet $\{A_l, B_l, C_l\}$ and includes those of the system, DAC/ZOH, ADC, smoothing filters and anti-alias filters. In general, the aggregate effect of these components outside of the primary system can be assumed to be a magnitude and phase shift, i.e. the components before and after the resonator can be assumed to have a somewhat fixed effect, specifically *for a narrow frequency band*.

For the tests performed in this study, the smoothing and anti-alias filters (with pickoff and forcer electronics included) are fairly similar, so most of the discrepancies between experimentally identified model and the true system are from the ZOH.

Regardless, it is important to recognize that for the tests performed in this study predictions and results were found within a 20 Hz frequency range conservatively and within that range the effects are roughly a gain and a phase adjustment. Thus, even though the mechanistic model is continuous, the inclusion of C_{1_l} and C_{2_l} matrices for fitting the lth nominal state of the resonator gives flexibility to account for a constant magnitude and phase shift due to these extra components before and after the resonator system. Thus, it is not only justified to include those matrices in the model but to go right ahead and fit the continuous time mechanistic model straight from the discrete time state space model.

4.4.3 Predictive Frequency Response

One additional flexibility of the mechanistic model is a full system frequency response to compare to the actual state of the system in addition to the modal properties, which older models do have. This yields the ability to take a deeper dive on the prediction results seen in the above section.

The frequency responses presented in Section 4.5 are all taken for output pick-offs S_4 and S_5 in the presence of D_1 and D_2. Referring back to Figure 1.1, the force and sense channels in focus are all orthogonal from the perspective of the $n = 2$ vibrational mode. Neither pick-off is equivalently located, i.e. $\pm 90^\circ$ or antipodal, to the forcers making for a good set of input/output channels for which both mode-shapes can generally be made out from the magnitudes of the vibrational modes.

For the outermost layer deposition results in from which the fundamental sensitivity is obtained, it should be clear that the frequency responses will be the same when looking at the prediction results after one point mass has been applied in Figure 4.3. Since the vacuum chamber temperature wasn't kept consistent between tests, it is expected to see somewhat of a shift between the predicted and actual observed models, however, what's critical is that the shape and modal peaks are essentially the same, which is what is observed.

4.5 Predictive Results

Initially the process in Section 4.4.1 is applied to a resonator to calculate a consistent point mass sensitivity, and thus a norm of the analytical dM matrix, adjusted depending on the ring layer(s) used for point mass application. From here, (4.6) predicts the mechanistic model matrices after a set of perturbations have been applied. Predictions are made for each layer individually in terms of putting down up to 4 point masses and predicting the state of the resonator after that many point masses have been placed for the outermost two layers. In addition two types of point masses are used for these tests: (1) Large (75 μm diameter) leaded solder spheres and (2) Small (35 μm diameter) unleaded solder spheres. The results of these predictions in terms of the post-perturbation modal properties are listed in this section and discussed in Section 4.6.

4.5.1 Predictions for Large Mass Perturbations

The results when point masses are applied to the outermost three ring layers are given below. Each figure contains modal frequencies, modal frequency split, and modal orientations. These are computed for the nominal state of the resonator, predicted for up to 4 point masses placed one after the other in a 60° arc on a single ring layer, and then compared against the modal properties measured after placing a point mass and measuring the transient based model for the new nominal state of the resonator.

In total, the model based predictions for the post-perturbation resonator states are fairly accurate for layers $k = 2, 3, 4$, where all of the orientations are accurately predicted but a few of the post-perturbation frequency splits are not as accurately predicted. These errors can be attributed to error in the actual mass on the solder spheres, slight orientation deviation of mass placement on the mass deposition sites, and higher harmonic effects on the $n = 2$ vibrational mode, discussed in Section 4.6.3.

When the vibrational modes get closer to being tuned, it is a better idea to use a point

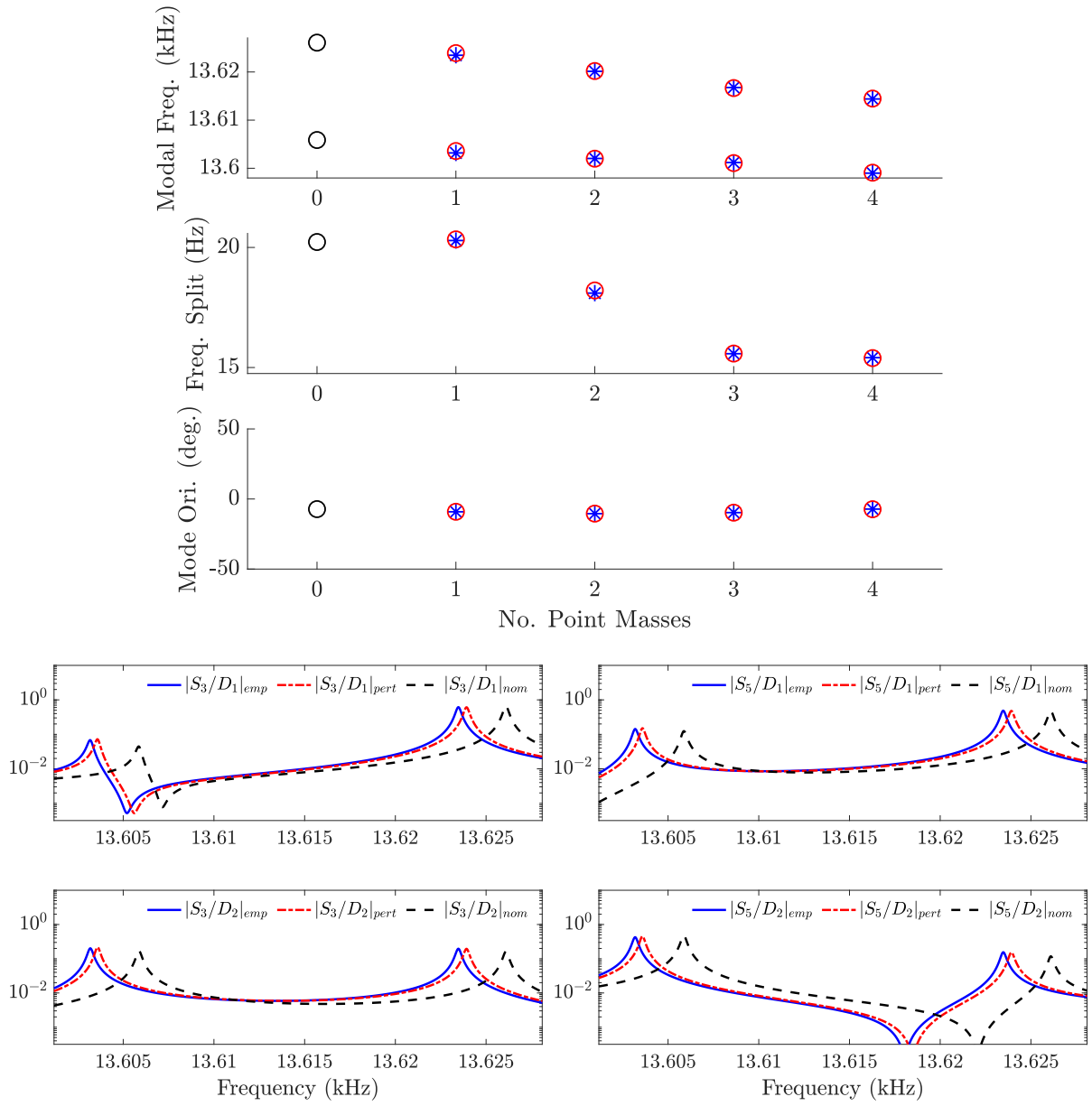

Figure 4.3: (top) Predicted (circles) and measured (stars) modal properties for small point masses placed on ring layer 4 (outermost) relative to nominal modal properties and (bottom) predicted (dash-dot) and measured (solid) frequency response magnitude after 1 large point mass is placed on ring layer 4, adjusting nominal (dashed) resonator state.

mass with lower sensitivity/mass so that it is easier to keep the modal frequency split in a fairly small range. Observing these states of the resonator for the outer two ring layers for smaller masses can also give a sense as to how the the mechanistic model performs as the modal properties can highly vary as the modes get close to degeneracy.

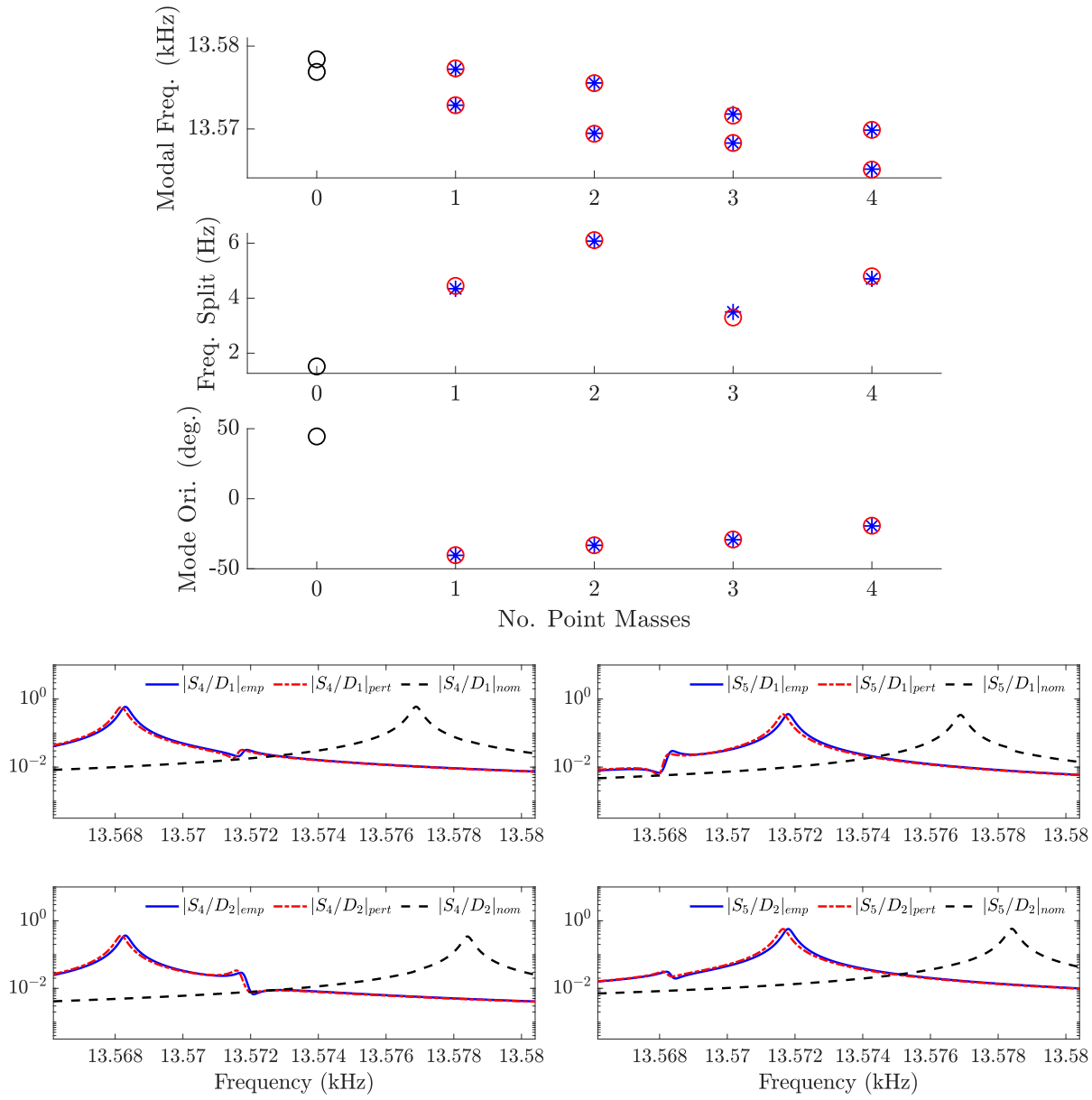

Figure 4.4: Predicted (circles) and measured (stars) modal properties for small point masses placed on ring layer 3 relative to nominal modal properties and (bottom) predicted (dash-dot) and measured (solid) frequency response magnitude after 3 large point masses are placed on ring layer 3, adjusting nominal (dashed) resonator state.

4.5.2 Predictions for Small Mass Perturbations

A scaling factor relating the small and large masses based on the ratio of solder sphere densities and cubed diameters is used to normalize the sensitivity in the small mass cases used in experiments on the outermost two layers. The discrepancy in mass is accounted for

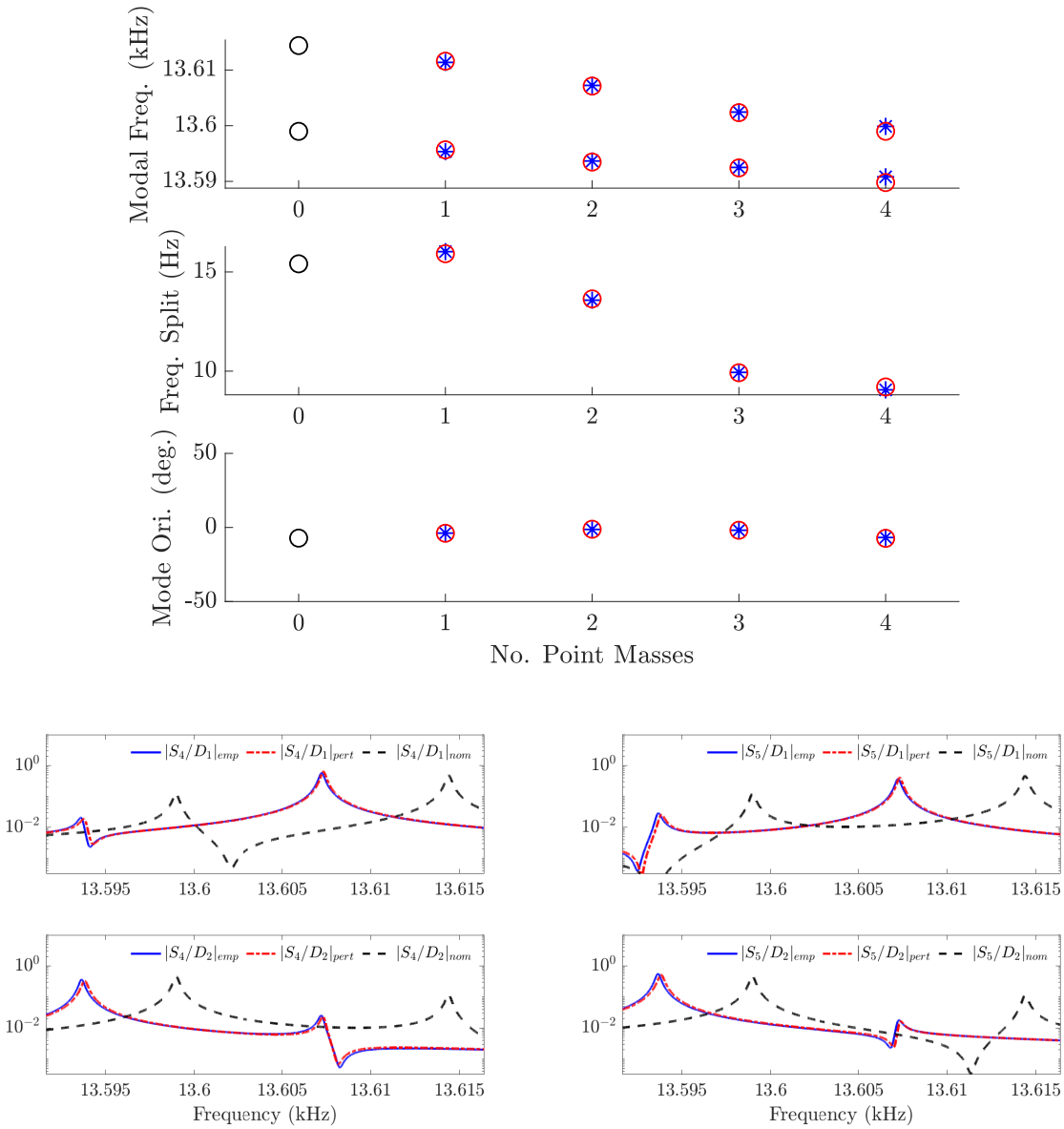

Figure 4.5: (top) Predicted (circles) and measured (stars) modal properties for small point masses placed on ring layer 2 relative to nominal modal properties and (bottom) predicted (dash-dot) and measured (solid) frequency response magnitude after 2 large point masses are placed on ring layer 2, adjusting nominal (dashed) resonator state.

when calculating the norm of Δ_m, i.e. the sensitivities are normalized to the larger diameter mass.

The results of the small perturbation studies on the outermost two layers is below in similar figures used in the prior section. The masses are placed strategically so that the model's efficacy can be determined as the modal orientations are more sensitive to small

changes when the modal frequency split is small.

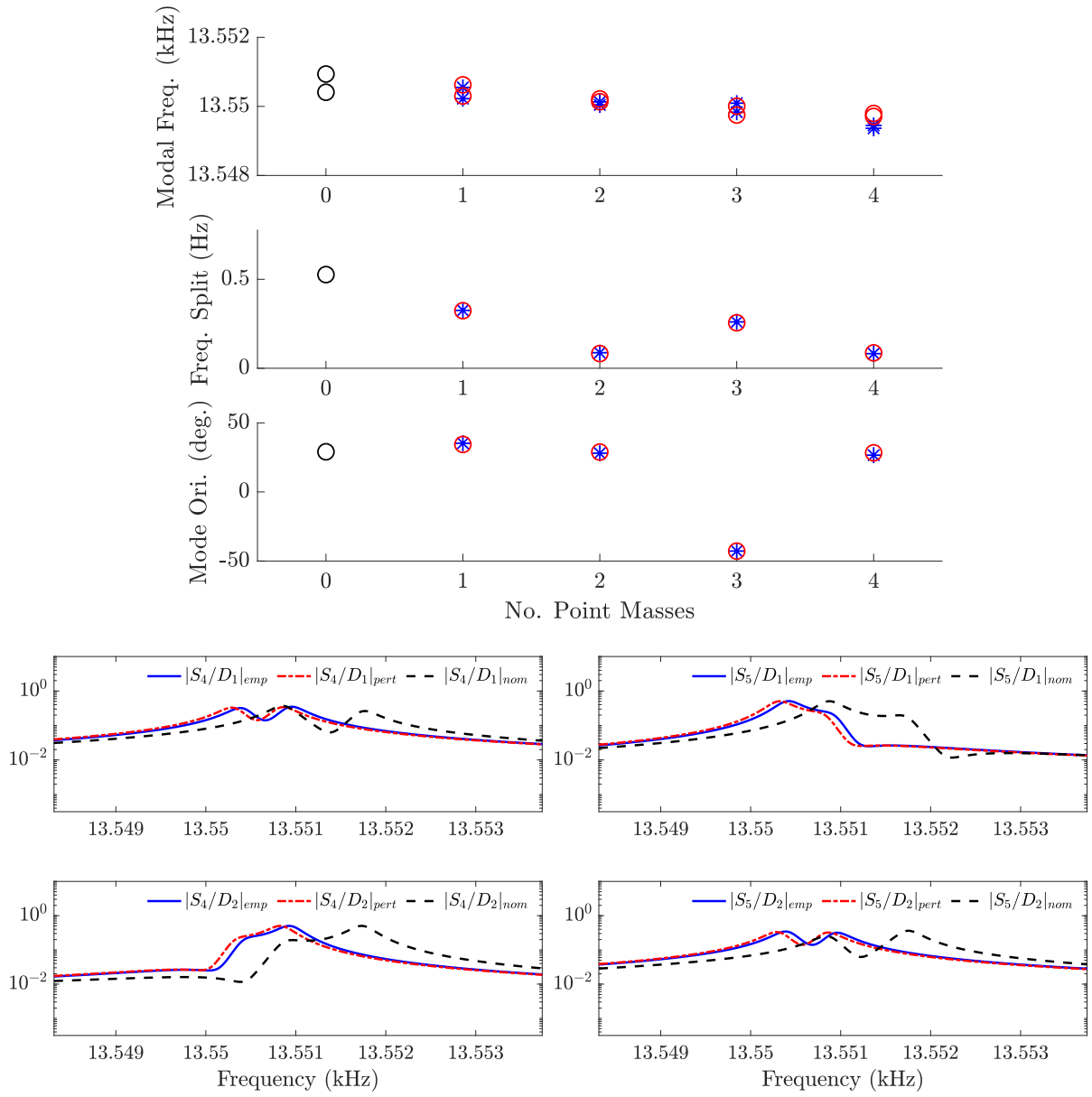

Figure 4.6: (top) Predicted (circles) and measured (stars) modal properties for small point masses placed on ring layer 4 (2nd outer) relative to nominal modal properties and and (bottom) predicted (dash-dot) and measured (solid) frequency response magnitude after 4 small point masses are placed on ring layer 4, adjusting nominal (dashed) resonator state.

To restate, the larger solder sphere cases were obtained when the modal frequency splits were relatively large. The smaller solder sphere cases were then obtained when the modal frequency splits were relatively small. From these results it would appear as if fine-tuning

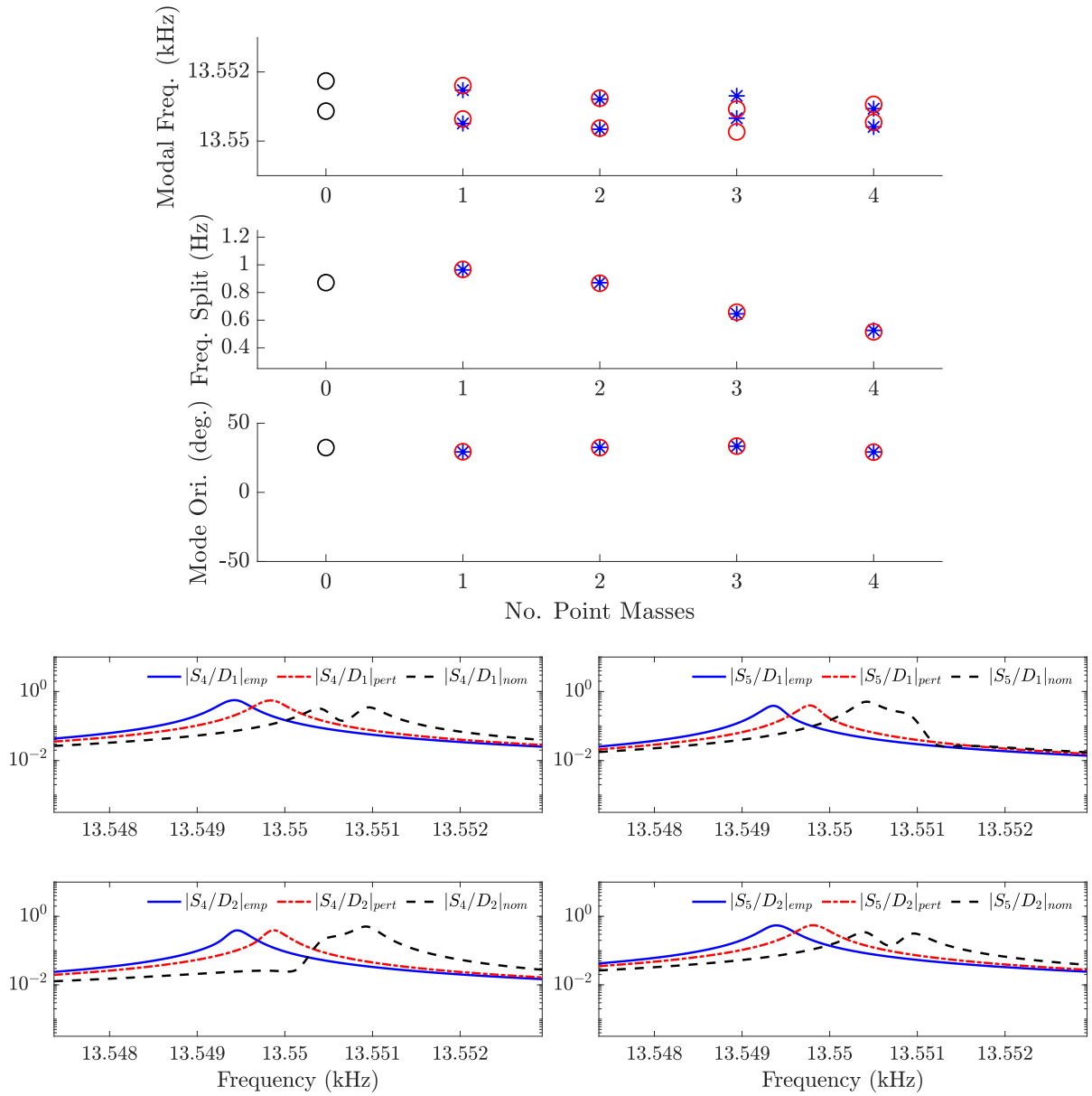

Figure 4.7: (top) Predicted (circles) and measured (stars) modal properties for small point masses placed on ring layer 3 (outer) relative to nominal modal properties and (bottom) predicted (dash-dot) and measured (solid) frequency response magnitude after 4 small point masses are placed on ring layer 3, adjusting nominal (dashed) resonator state.

the resonator, i.e. using small point masses to get the modal frequencies close to degenerate, can be constrained to mass deposition sites on the two outermost layers.

4.6 Discussion

4.6.1 Predictive Capability

The results in Section 4.5 show that the modal properties are predicted *qualitatively* well for the outermost layers and up to a few steps ahead in terms of point masses placed, whether small or large. Crucially the model still predicts quite well when the frequency split is quite small and masses are placed on the outermost two layers. The frequency responses further highlight the predictive efficacy of this model as the splits get small and the modal properties become sensitive. Figure 4.3 shows frequency shifts between the predicted and actual results due to experimental temperature discrepancies but very similar shaped magnitude spectra.

To show these ideas more *quantitatively* for each case presented in the above results section, an absolute error is computed for modal frequency split and orientation between the predictive model and the transient space model used to fit a nominal state of the resonator. Results are presented in Tables 4.2 and 4.3 below, where "PM" refers to point mass and "S" and "L" are small and large respectively, referring to the two sizes of mass depositions used in these tests.

Modal Frequency Split Model Absolute Error (Hz.)						
N PM Ahead	k=4 LPM	k=3 LPM	k=2 LPM	k=1 LPM	k=4 SPM	k=3 SPM
1 PM	0.0555	0.1833	0.0799	0.4674	0.0068	0.0062
2 PM	0.1293	0.2861	0.0953	1.1331	0.0009	0.0085
3 PM	0.0936	0.0255	0.2765	0.4926	0.0067	0.0077
4 PM	0.0809	0.2124	0.2248	0.2168	0.0112	0.0042

Table 4.2: Modal frequency split absolute error between N point mass (PM) ahead predictive and transient state space model

To capture even more of how the predictive capability as it pertains to the ring layers, each nominal state of the resonator has a predictive model fit and one step ahead predictions are computed. Table 4.4 shows average modal property absolute errors between the predictive and transient models.

Mode Orientation Model Absolute Error (Deg.)						
N PM Ahead	k=4 LPM	k=3 LPM	k=2 LPM	k=1 LPM	k=4 SPM	k=3 SPM
1 PM	0.0259	0.2103	0.0195	0.6081	0.0778	0.6073
2 PM	0.0120	0.1318	0.2431	0.6970	0.0570	2.1394
3 PM	0.0174	0.2973	0.2724	1.4115	0.2922	0.6544
4 PM	0.1307	0.5076	0.7092	2.5769	0.2188	0.1135

Table 4.3: Modal orientation absolute error between N point mass (PM) ahead predictive and transient state space model

Average Model Error for 1 Step Ahead Predictions						
Mod. Prop.	k=4 LPM	k=3 LPM	k=2 LPM	k=1 LPM	k=4 SPM	k=3 SPM
Freq. (Hz.)	0.0479	0.1279	0.0768	0.5900	0.0084	0.0051
Ori. (Deg.)	0.0548	0.1810	0.1853	0.5944	0.0965	0.8013

Table 4.4: Average modal property absolute errors over all ring layers.

With the results shown in a more quantitative manner, there are a few key takeaways:

1. The model does a poor job of predicting the effect of placing any number of point masses on the innermost ring layer. The error in frequency split being at max more than 1 Hz and the orientation error being more than 1° is pretty undesirable here, given that the frequency split in these cases is fairly large. This is more succinctly seen in the average results as well contrasting the innermost layer with the other layers. More details to explain this failing of the model are seen in Section 4.6.3.

2. The model performs decently well in predicting dynamic changes when masses are applied for a state close to modal degeneracy. Specifically, when the modal split is below 0.1 Hz as small point masses are applied to the second outermost layer, the modal frequency splits are well predicted but the modal orientation prediction is more erroneous. This is not surprising due to the high sensitivity of the modal orientations as the modal split reaches degeneracy, seen quite clearly in Figure 4.7.

4.6.2 Temperature Based Modal Frequency Shift

There is a clear shift in the experimentally measured and predicted modal frequencies that initially brings into question if the predictive model is accurate, especially as you predict for a few point masses simultaneously. Each experiment notably is not temperature regulated, so although the vacuum chamber used for testing any resonator is allowed a decently long startup time in order for the test temperature to reach steady state, there is no set temperature, which at steady state might vary between tests. The model does not incorporate this potential discrepancy because although a temperature difference shifts the absolute modal frequencies, the frequency split crucially is not affected., highlighted in Figures 4.6 and 4.7. Although the magnitudes are shifted, the *inherent structure in the frequency responses* is similar, and the error data in the previous section illustrates a minuscule difference in the frequency split for these case, again not due to a temperature difference between experiments.

4.6.3 Sensitivity of Inner Ring Layer Predictions

Based on the modeling approach in this paper, the basis functions only take into account the nth mode, or specifically $n = 2$. With this in mind, for the innermost ring layer for which mass depositions can be placed, the 6^{th} and 10^{th} harmonics of radial displacement carry significant contribution and thus affect the vibrational modes after a point mass has been placed. This effect can be seen pretty clearly in Figure 4.8. For layer 1, the four mass depositions were placed sequentially in 15° increments around the resonator. Thus, the sinusoidal functional form of the dM, and thus the frequency split as the 60° arc is journeyed across is clear in the predictions, however, the actual results are corrupted by phase and magnitude adjustments to the change in mass based on those significant higher harmonics. The figure also highlights that the frequency responses are not too different, sans a necessary adjustment to the sensitivity of dM, such that the lower modal frequency could shift more than predicted. Due to the variance for optimal sensitivities for the inner-most layers being

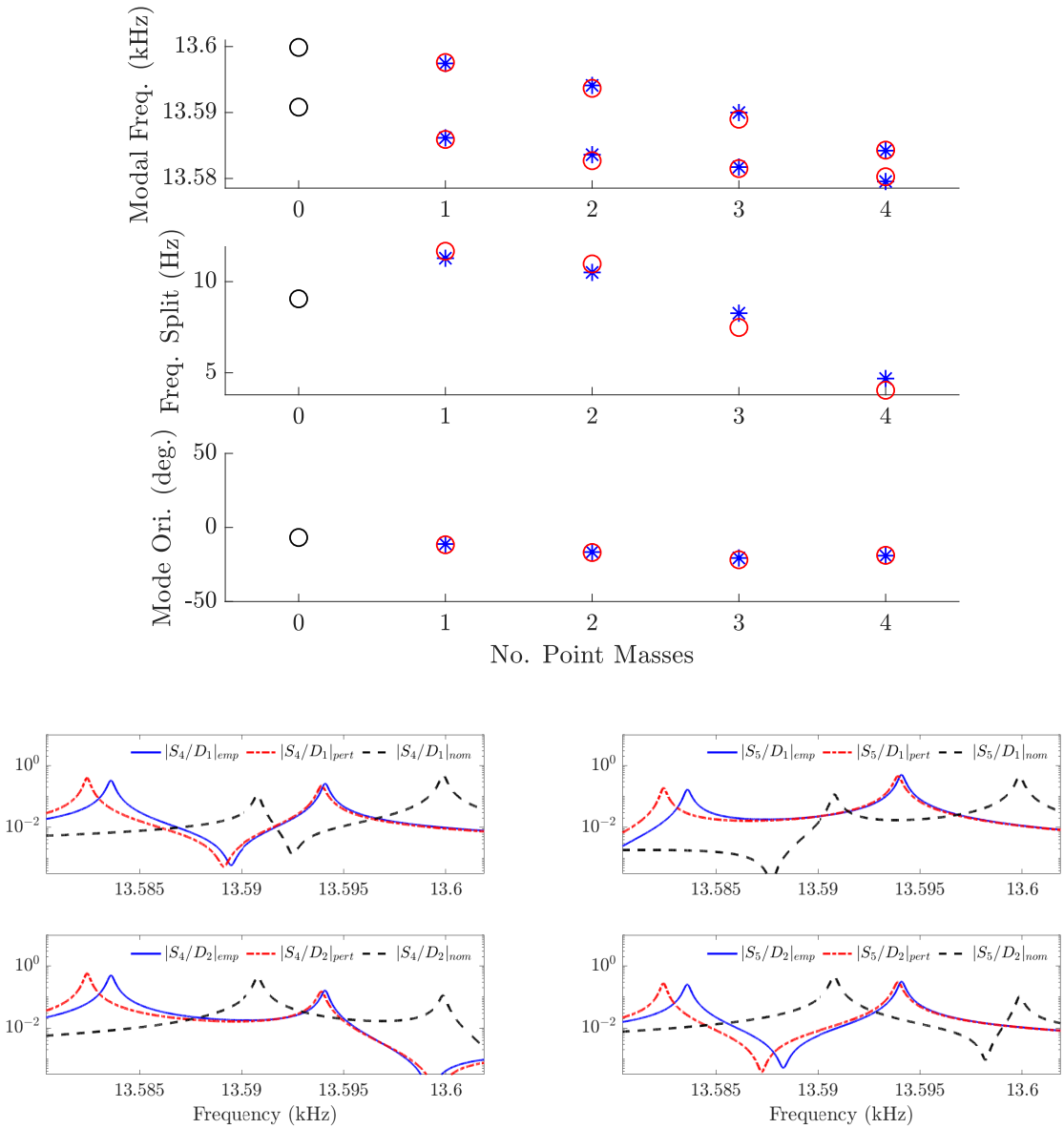

Figure 4.8: (top) Predicted (circles) and measured (stars) modal properties for large point masses placed on ring layer 1 relative to nominal modal properties, i.e. 0 point masses placed and (bottom) predicted (dash-dot) and measured (solid) frequency response magnitude after 2 large point masses are placed on ring layer 1, adjusting nominal (dashed) resonator state

too high, the outermost three layers should be the only point mass placement layers used for predictive purposes.

4.6.4 Tuning of the $n = 2$ Modal Frequencies

With the physical model fleshed out and its sensitivity highlighted, a tuning algorithm specific to this model is described. Consider (M_0, K_0), representing the mass and stiffness matrix pair contained in the predictive model of the current nominal state of the resonator for the nth mode. It is desired to obtain a solution for placement of point masses, constrained by the total number of point masses placed, on the resonator such that the generalized eigenvalues between M_0 and K_0 are as close as possible to one another. An initial normalization process can be made to make any potential optimization problem more standard across all nominal resonator states. Let $\tilde{M}_0 = (1/\bar{\omega}^2)TM_0T^*$, where $T = \sqrt{K_0^{-1}}$ and $\bar{\omega}$ is the mean modal frequency in rad/s for the current nominal resonator state and the nth vibrational mode. Then the transformation yields $\tilde{K}_0 = \alpha * I$, where α is some real scalar close to 1. Let $\tilde{M} = \tilde{M}_0 + \sum_i \mu_i \tilde{\Delta}_{M,i}$, be the desired mass matrix after mass perturbations have been applied, i.e. mode tuning requires $\tilde{M}$ to be as close to scalar times identity as possible. This can be accomplished by optimizing the individual entries of the transformed mass matrix as mass perturbations are potentially applied.

Define the entries of the desired transformed mass matrix, nominal mass matrix, and mass perturbations as

$$\tilde{M} = \begin{bmatrix} m_{11} & m_{12} \\ m_{12} & m_{22} \end{bmatrix}, \; \tilde{M}_0 = \begin{bmatrix} m_{0_{11}} & m_{0_{12}} \\ m_{0_{12}} & m_{0_{22}} \end{bmatrix}, \; \tilde{\Delta}_{M,i} = \begin{bmatrix} dm_{i_{11}} & dm_{i_{12}} \\ dm_{i_{12}} & dm_{i_{22}} \end{bmatrix},$$

where the entries of the mass perturbation matrix vary depending on type of mass, ring layer placed, and theta along the ring layer. Each decision variable indexed by i is a function of these, giving a total of $N = 12K$ integer decision variables, where K is the number of ring layers used, there are 2 total point masses used, and there are 6 unique placement location in terms of their mass matrix effect per layer. Thus, a solution is denoted by the vector $x = \{\mu_1, \ldots, \mu_N\}$.

The objective function is then $\min(\beta_1|m_{11}-m_{22}|)+\beta_2|m_{12}|)$, where β_1, β_2 are adjustable constants, as the goal is to minimize the absolute value of the difference between the diagonals as well as the off-diagonals so that the resultant mass matrix is close to scalar times identity, where it is initially unknown what the contribution of each to the overall objective should be. Because the decision variables μ_i are purely integer valued, the solution space can be divided into four constrained sets with four separate optimization problems as follows:

$$
\begin{aligned}
(1) : \min(&\beta_1(m_{11}-m_{22})+\beta_2(m_{12})), \\
&m_{11} > m_{22}, m_{12} > 0. \\
(2) : \min(&\beta_1(m_{11}-m_{22})+\beta_2(-m_{12})), \\
&m_{11} > m_{22}, m_{12} < 0. \\
(3) : \min(&\beta_1(m_{22}-m_{11})+\beta_2(m_{12})), \\
&m_{11} < m_{22}, m_{12} > 0. \\
(4) : \min(&\beta_1(m_{22}-m_{11})+\beta_2(-m_{12})), \\
&m_{11} < m_{22}, m_{12} < 0.
\end{aligned}
$$

where $m_{11} = m_{0_{11}} + \sum_i \mu_i dm_{i_{11}}$, $m_{12} = m_{0_{12}} + \sum_i \mu_i dm_{i_{12}}$, $m_{22} = m_{0_{22}} + \sum_i \mu_i dm_{i_{22}}$.

Common among all such tuning optimization problems of this type are constraints on point mass placement, namely a constraint on the total number of point masses that can be used and the total number of point masses that can be placed at a particular location, which is 4 for a combination of small and large point masses given that for the $n = 2$ mode there is repetition in the effect around the resonator when a point mass is placed in 90° increments from a particular mass placement location.

There are optional constraints additionally to achieve simultaneous modal frequency tuning and modal orientation placement, which all optimization problems also share. This set

of constraints is described. Let $R(\theta) = \begin{bmatrix} \cos(\theta) & -\sin(\theta) \\ \sin(\theta) & \cos(\theta) \end{bmatrix}$ be the rotation matrix that diagonalize $\tilde{M}$. Thus, $R(\theta_0)$ diagonalizes $\tilde{M}_0$. It follows that $\tan(2\theta_0) = \frac{2m_{0_{12}}}{m_{0_{11}} - m_{0_{22}}}$ and $\tan(2\theta) = \frac{2m_{12}}{m_{11} - m_{22}}$. Note that although θ_0 and θ are not the modal orientations of the first mode before and after the tuning process, $\delta\theta = \theta - \theta_0$ does correspond to the change in modal orientation of the first mode, given that the pick-off orientation is consistent in all tests. Thus, if the first mode's nominal modal orientation is known and the first mode's desired modal orientation is selected, then constraints can be made on the change in modal orientation such that the modal orientation post-tuning is bounded above and below, i.e. the post-tuning modal orientation can be constrained to be within a set of angles. For instance, $\delta\theta$ can be specified to be 15 ± 1 deg. It is important to specify the range to be large enough that a optimization solution is achievable given the constraint on the total number of allowable placed point masses.

With these constraints in mind, solving the optimization problems yields up to four optimal solutions (only two given a modal orientation constraint) that have an optimal solution amongst them, denoted x_{opt}.

4.7 Conclusion

A new predictive model is derived using analysis on the thin ring and extended to the desired ring resonator by applying FEM analysis on the ring resonator to the system in question. This new model is optimally fit from the Hankel based state space model seen in Chapter 3 using an LMI procedure to minimize the error between the system frequency responses. This new model performs well predictively with a few point masses and for the outer ring layers. The inner ring layer predictions, for this model and older models, are poor and as such these layers shouldn't be used to fine tune modal frequencies, however, these layers can be used to assist in initially reducing a larger frequency split without the use of many point masses

given the inner ring layers have higher frequency split sensitivity. Because this new model is complementary to older models, both can be used in making predictions. A potential tuning algorithm for this model is also rigorously derived.

CHAPTER 5

Measuring and Modeling Resonator Stem Reactions

Analysis of the center of mass in Sections 2.4.1 and 2.4.2 highlights a key oversight in mode pair tuning a MEM-DRG. Although steps may have been taken to tune a resonator, such as with the use of tuning masses, this new state of the resonator may now be imbalanced such that there is significant coupling between the $n = 2$ modes and the resonator's center stem. The objective of this chapter is to model and measure this coupling for disk resonators. The first step is the design, fabrication, and calibration of a six degree of freedom (DOF) Force/Torque (F/T) transducer for measuring stem reactions. Successful attempts are made to mitigate resonator/base motion coupling using properly placed tuning masses.

5.1 Overview

Extending the prior section's motivation to resonators, recall that manufacturing issues/imprecision yield an inability to *apriori* predict the degree and location of resonator/stem coupling and imbalance. Crucially there are also no published works relative to measuring center stem reactions for a ring-like disk resonator gyroscope.

As mentioned, these measurements can inform structure balancing to reduce stem reactions and thus coupling based energy losses, which in turn yields higher Q factors in resonator modes of interest. The primary challenge in these stem force and torque reaction measurements is that these measured reactions in the form of displacements are a few orders of magnitude lower than ring displacements present in the rings of the resonator gyroscope.

In other words great care must be taken in the design of a reaction transducer in order to even pick up the reactions themselves.

5.2 Motivation: Evidence of Micro-Resonator Die Motion

The initial desired applied system for measurement of stem reaction forces and torques is the micro scale resonator seen in Chapters 3 and 4. Rudimentary measurements with a laser vibrometer show that these reactions can be measured in the resonator's silicon base, and initial attempts to design a F/T transducer test bed along with challenges are described.

5.2.1 Resonator and Vibrometer Measurements

Section 1.2 describes the experimental conditions of the vacuum chamber. The MEM-DRG setup is similar to earlier tests with the addition of a laser vibrometer, aligned to hit the die side via a quartz prism, which detects planar die displacement when the $n = 1$ or $n = 2$ vibrational modes are actuated. Figure 5.1 highlights the position of the prism, MEM-DRG, and vibrometer laser/quartz prism in the vacuum chamber.

To gain insight into an electrode based system design to measure the die motion, it is desired to plot the frequency responses for the vibrometer in units of mm/V instead of the acquired V/V units. The sensitivity on the vibrometer velocity measurement, denoted S, is $S = 5\ mm/s/V$ for all measurements. Thus to convert to a displacement, take the measured frequency response, multiply by the sensitivity and integrate, or $H_{mm/V}(j\omega) = \dfrac{S \cdot H_{V/V}(j\omega)}{j\omega}$. The $n = 1$ and $n = 2$ resonator vibratory modes seen in the die motion are captured in the frequency responses, with magnitudes having units of $\mu m/V$, in sections 5.2.2 and 5.2.3. The appropriate conversion for resonator pick-offs is reviewed in Section 1.3.

For both the $n = 1$ and $n = 2$ resonator vibratory modes, the goal is to see these modes expressed, although with smaller displacement, in the die motion as measured by the vibrometer. The vibrometer output is treated as a random signal, and, as such, correlation

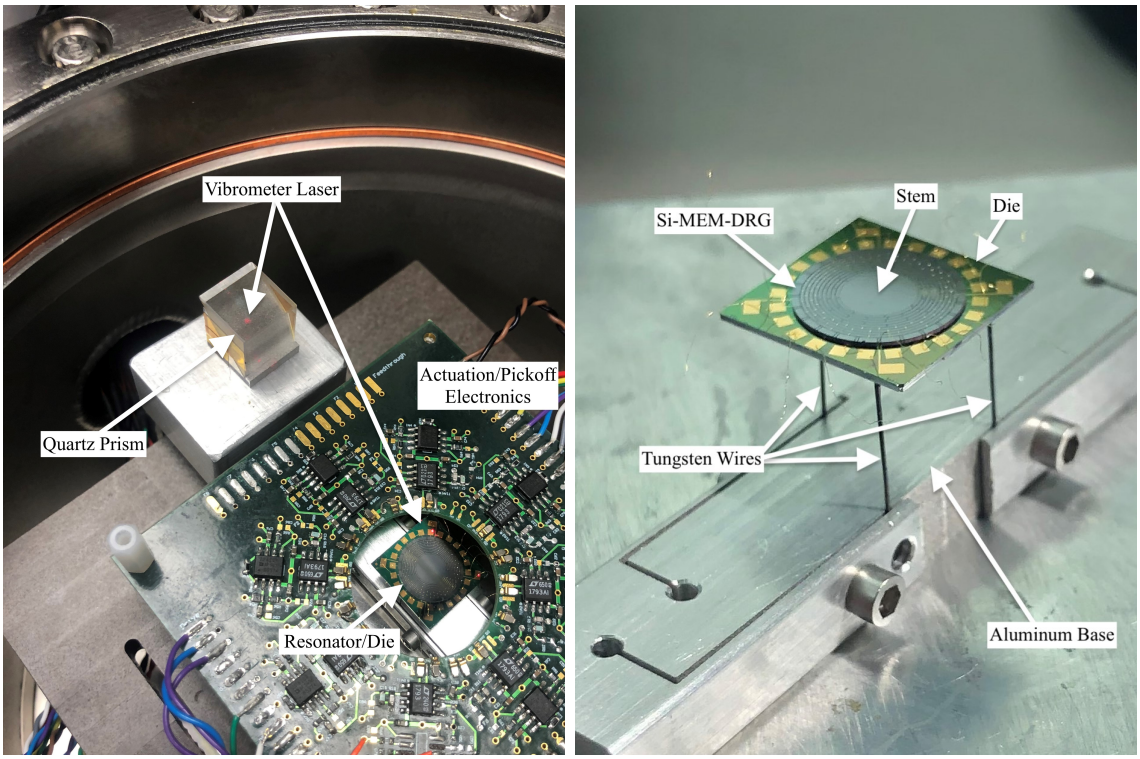

Figure 5.1: Experimental setup (left) is shown for measuring MEM-DRG vibrational modes and planar die motion simultaneously. Tungsten wires with a base holding the wire bottoms fixed (right) act as vibration isolation for the resonator and die, reducing the noise floor for vibrometer measurements.

analysis is employed to estimate the frequency response between the vibrometer output and the forced input to the resonator, i.e. band limited chirp containing the resonator modes. Multiple data sets are taken and averaged to obtain an estimated frequency response. For $n = 1$, the input has a 150 Hz bandwidth and 20 averages are taken for a 5 second input chirp signal. For $n = 2$, the input has a 10 Hz bandwidth and 20 averages are taken for a 10 second input chirp signal, as these modes are close to degenerate so a focused bandwidth is necessary.

Frequency responses are shown for experiments where the die is fixed onto three Tungsten wires. For each vibrometer frequency response figure, the first column corresponds to the response from input D_1 and the second column corresponds to the response from input D_2. For the resonator magnitude responses, the top row corresponds to the response from input D_1 and the second row corresponds to the response from input D_2.

The identified frequencies, for both $n = 1$ and $n = 2$ modes, between the tests performed using D_1 and D_2 are slightly shifted due to slight temperature changes between these tests as the resonator is not temperature regulated, however, each test yields the same frequency split for both mode pairs.

5.2.2 n=1 Responses

For the $n = 1$ modes, the resonator stem is not a node, so strong coupling between the resonator and its stem is expected. This is confirmed in Figure 5.2. Although the wires dampen the modes and die motion slightly, the $n = 1$ modes are clearly seen in the vibrometer measurement. The $n = 1$ responses are fairly similar between the repeated tests, highlighting

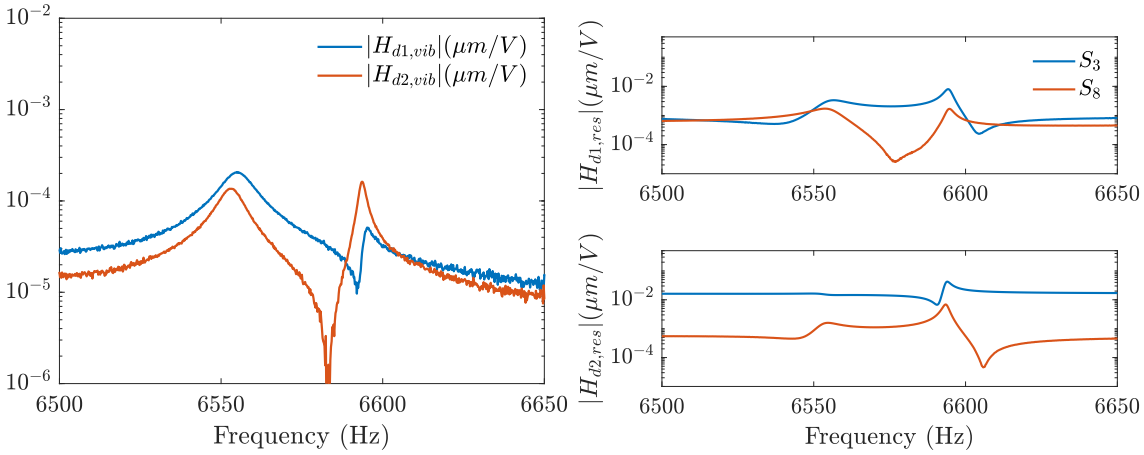

Figure 5.2: Vibrometer (left) and resonator (right) frequency responses focused on $n = 1$ when die is on tungsten wires. Resonator responses for S_3 and S_8 are shown separately for D_1 (top) and D_2 (bottom).

the repeatability of such experiments.

5.2.3 n=2 Responses

The more important set of experiments to analyze are those done for the $n = 2$ modes because the stem is a node for the resonator, hence an ideal MEM-DRG would have no coupling to its stem, which would show in terms of die motion, for the $n = 2$ modes. Figure 5.3 highlights the small yet still significant coupling present between the resonator

and stem as the modes, although close to tuned, are apparent in the vibrometer responses. Comparison of the $n = 1$ and $n = 2$ are encouraging, as the base motion in $n = 1$ modes are

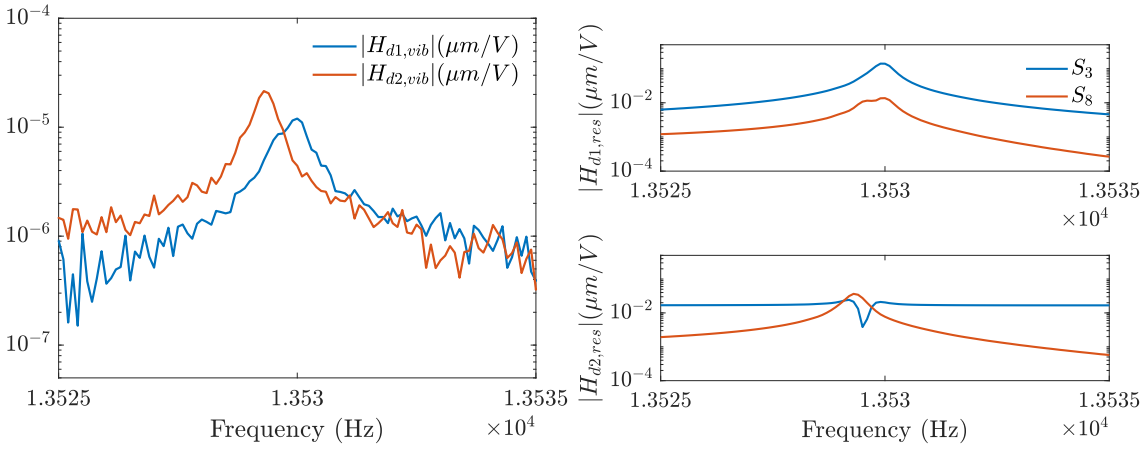

Figure 5.3: Vibrometer (left) and resonator (right) frequency responses focused on $n = 2$ when die is on tungsten wires. Resonator responses for S_3 and S_8 are shown separately for D_1 (top) and D_2 (bottom).

expected to be significantly higher than that in the $n = 2$ modes.

5.2.4 Challenges

The work shown in this section highlights that the motion of the base in a micro resonator can be measured at a single point on the resonator die, however, a few initial designs (not shown for sake of brevity) were created with the intention to measure multiple locations simultaneously on the resonator base. A design with two electrodes measuring one side of the base and two other electrodes measuring a perpendicular side would yield an over-determined system of sense channels from which the planar triplet of stem reaction forces and torques, i.e. $\{f_x, f_y, m_z\}$ can be extracted, however, this doesn't take into account the challenges in building, testing, and calibrating this micro-scale transducer. These electrodes would have to be mounted in such a way so that each electrode can be properly aligned relative to the sides of the resonator base. Because the motion of the base is significantly smaller relative to the resonator motion, these electrodes would have to be placed extremely close to the base itself so that the change in nominal gap can actually be measured as a

healthy output signal.

A workaround to study stem reaction forces for the disk resonator is to scale up the entire system to a macro scale. The advantages of this approach include (1) The mass perturbations are achieved on the macro scale via application of small temporarily placed magnets, and more importantly (2) A base can be designed and built with a six DOF F/T transducer internal to that base, which includes sensing of the $\{f_z, m_x, m_y\}$ triplet of stem reactions that would be almost impossible to design for in the micro-scale system.

The following section explores single axis, coupled oscillator models building up to the full resonator/transducer/base system to inform the macro-scale F/T transducer design process.

5.3 Simple Coupled Oscillator System Model

A simple force transducer has the following properties:

1. $\omega_{base} < \omega_{res,1} < \omega_{res,2} < \omega_{tr}$, i.e. the resonant frequencies fall between the maximum vibration isolation mode frequency ω_{base} and minimum transducer mode ω_{tr}.

2. There is a wide frequency range where the gain is constant for the frequency response from input force applied on the transducer and output transducer displacement. In essence this implies that any transducer should have a regime where the reaction force picked up by the transducer is proportional to its displacement.

Figure 5.4 shows a diagram of a simple resonator/transducer/vibration isolation base system.

If the transducer/base are isolated, i.e. there's no resonator, and then looking at a mass/stiffness linear system model for the state $\vec{y} = \{y_{base}, y_{tr}\}$, the mass and stiffness

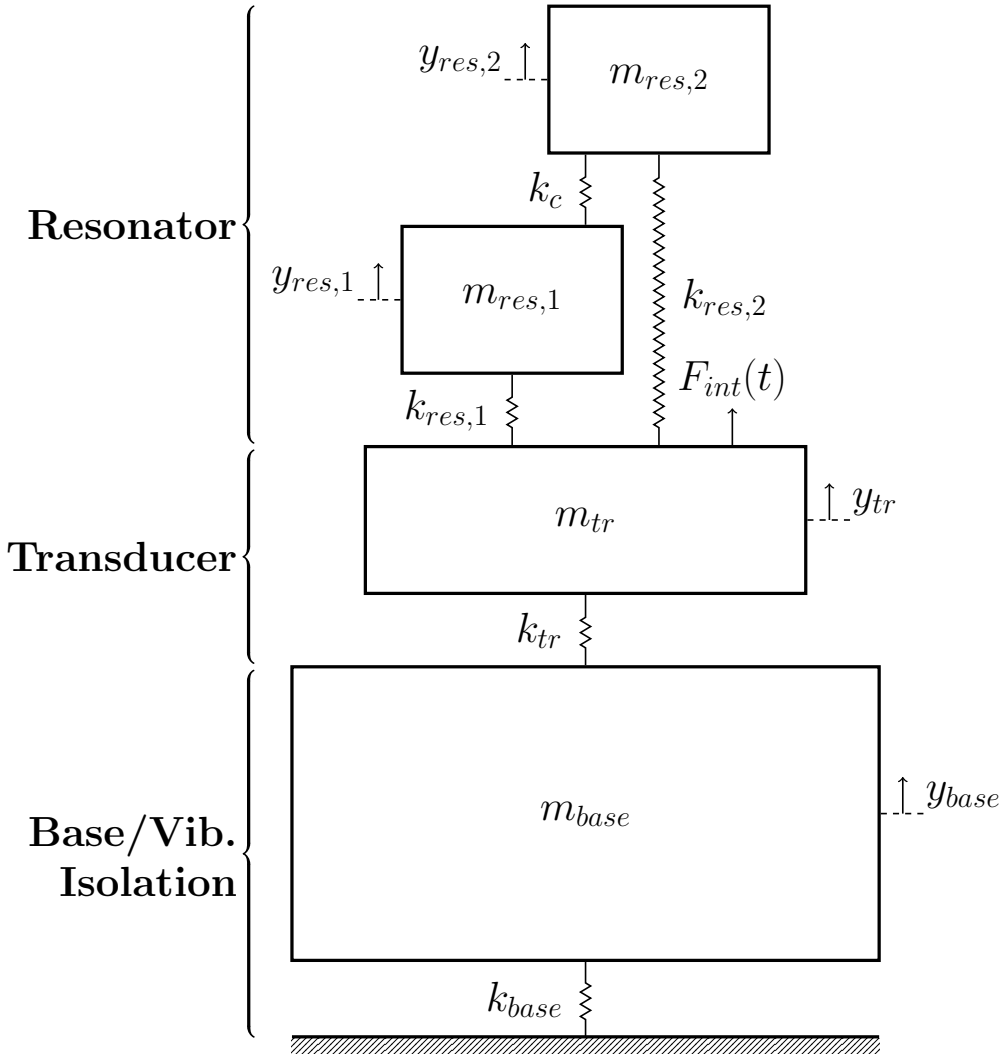

Figure 5.4: A coupled oscillator model highlights the resonator comprised of a spring-coupled (k_c) pair of mass spring systems, the transducer, a mass-spring system coupled to both the base and resonator, and a base with $m_{base} >> m_{tr}$. $F(i)$ denotes an applied force on the transducer mass, and y_{tr} represents the transducer mass displacement.

matrices are

$$M = \begin{bmatrix} m_{base} & 0 \\ 0 & m_{tr} \end{bmatrix},$$

$$K = \begin{bmatrix} k_{base} + k_{tr} & -k_{tr} \\ -k_{tr} & k_{tr} \end{bmatrix}.$$

Looking at a mass/stiffness linear system model for the state $\vec{y} = \{y_{base}, y_{tr}, y_{res,1}, y_{res,2}\}$, the

mass and stiffness matrices are

$$M = \begin{bmatrix} m_{base} & 0 & 0 & 0 \\ 0 & m_{tr} & 0 & 0 \\ 0 & 0 & m_{res,1} & 0 \\ 0 & 0 & 0 & m_{res,2} \end{bmatrix},$$

$$K = \begin{bmatrix} k_{base} + k_{tr} & -k_{tr} & 0 & 0 \\ -k_{tr} & k_{tr} + k_{res,1} + k_{res,2} & -k_{res,1} & -k_{res,2} \\ 0 & -k_{res,1} & k_{res,1} + k_c & -k_c \\ 0 & -k_{res,2} & -k_c & k_{res,2} + k_c \end{bmatrix}.$$

y refers to y_{tr} as the transducer displacement is of the most interest in the analysis.

After normalizing all parameters in both models by the transducer mass, the following values are set to keep the base mode, resonator modes, and transducer mode separated in order to easily analyze the simple with and without resonator models relative to each other

$$m_{base} = 20,\ m_{tr} = m_{res,1} = 1,\ m_{res,2} = 1.02,$$
$$k_{base} = 1,\ k_{tr} = 100,\ k_{res,1} = k_{res,2} = k_c = 4.$$

This places the resonator modes near 2 Hz, the base isolation mode at $\sqrt{1/20}$ Hz, and the transducer mode at 10 Hz, all of which are well separated in frequency.

The frequency responses of interest in the model are described where the output for all frequency responses is the transducer spring force, or $F_{sp,tr} = k_{tr}(y_{tr} - y_{base})$. $H_1(\omega)$ represents $F_{sp,tr}$ relative to the applied force on the transducer, $H_2(\omega)$ represents $F_{sp,tr}$ relative to an input disturbance to the base, and $H_{1,nobase}(\omega)$ (green dashed) is again $F_{sp,tr}$ relative to the applied force on transducer, but without a base present, where Figure 5.5 highlights these frequency responses for the single axis system model with and without a resonator coupled to the transducer/base system.

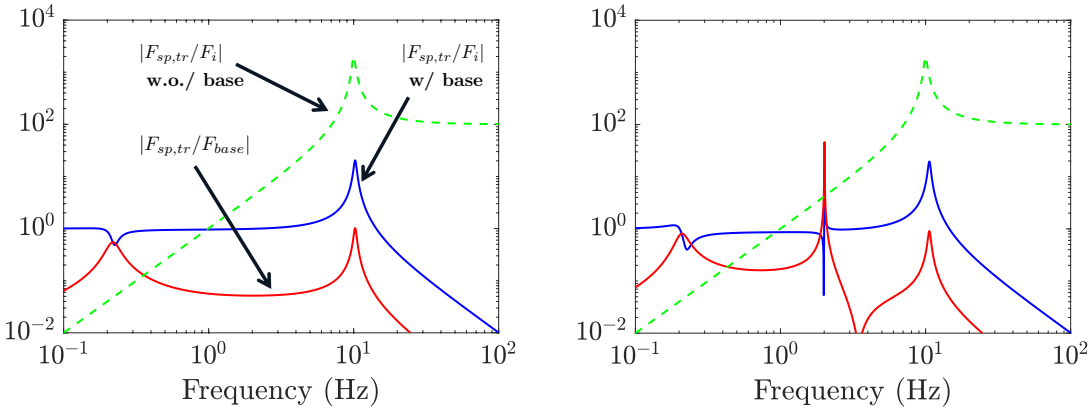

Figure 5.5: Pertinent transducer frequency responses are shown for the system with (left) and without (right) a resonator. In each plot, $F_{sp,tr}$ relative to the applied force on the transducer is shown without the seismic isolation base (green dashed) and with the base (blue). $F_{sp,tr}$ relative to an input base disturbance F_{base} is also shown (red)

A few key insights about the frequency responses for each system are noted. First, without a base, a flat region for the transducer is not established and the resonator modes are not observed. Second, for H_1, there is a large frequency range between 0.3 and 6 Hz where the transducer is usable. This is sufficient given the resonator modes are located around 2 Hz. Zooming in on the frequency responses between 1 and 3 Hz, for H_1, the system gains are slightly but not significantly different with and without a resonator. Thus it can be assumed a transducer need not be calibrated with a resonator mounted. Finally, the gain associated with H_2 is at least an order of magnitude lower than that in H_1 for both systems and so an input disturbance on the base will have little effect on the observed spring force, especially if the base mass is made significantly larger than the transducer and resonator masses.

Additionally it is important to study the effect of model parameters on transducer detection of the resonant modes. Of specific interest is the effect of the seismic base mass, while keeping ω_{base} fixed, on the ratio of stem force F_{st} to transducer measured force $F_{tr} := F_{sp,tr}$, which should be unity for an effective transducer for it to operate as an effective force trans-

ducer. Based on the model,

$$F_{st} = k_{res,1}(y_{res,1} - y_{tr}) + k_{res,2}(y_{res,2} - y_{tr}),$$
$$F_{tr} = k_{tr}(y_{tr} - y_{base}).$$

Varying the seismic mass, and then computing and plotting the force ratio for each resonator mode, yields Figure 5.6 below. As the seismic mass is increased, the ratio for both resonator modes converges to within 1 percent of unity.

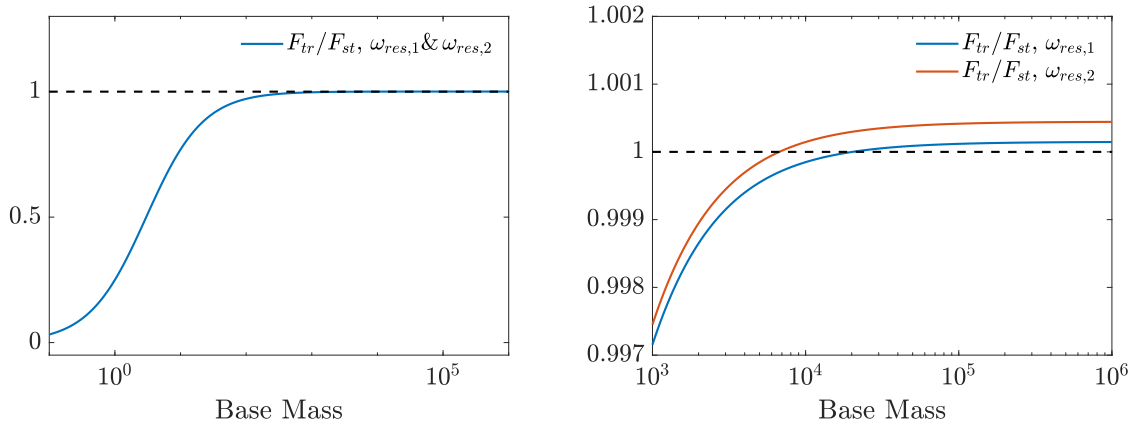

Figure 5.6: Force ratio is shown (left) between F_{tr} and F_{st} as the seismic mass is increased with ω_{base} fixed. The ratio converges close to unity as the seismic mass now overwhelmingly dominates in the total system mass (right).

5.4 Design of a Stiff Piezo-Electric (PZT) Based F/T Transducer for Macro-scale Applications

The need to measure the set of stems forces and moments, denoted by the sextuplet

$$\{f_x, f_y, f_z, m_x, m_y, m_z\},$$

helps inform the pick-off layout in the transducer. Additionally, the intuition gained from the simple models in the prior section guides the design for the six DOF F/T transducer. The

need for this transducer to be stiff dictates the use of stiff sensing elements, which motivates the use of piezoelectric elements (PZTs) instead of using a set of strain gauges.

5.4.1 Transducer Design

The transducer contains mostly aluminum with six 10x10x2 mm PZTs as sensing elements. Specifically, the PZTs are placed into two PZT layers. In the "Vertical" layer, the PZTs are placed such that compression/expansion primarily occurs vertically. This setup is in theory ideal for the measurement of F/T triplet $\{f_z, m_x, m_y\}$. In the "Horizontal" layer of PZTs, compression/expansion primarily occurs horizontally, and, as a result, this layer is meant to measure the other triplet $\{f_x, f_y, m_z\}$. The isometric views in Figure 5.7 highlight that the "Vertical" layer of PZTs simply bridge the top and middle aluminum layers. The "Horizontal" layer of transducer pick-offs connects the aluminum middle and bottom layers via aluminum block extrusions.

5.4.2 PZT Charge Amplification

Although the PZTs in the F/T transducer help to stiffen the overall sensor, the displacements in the PZTs are fairly small. As pick-offs, these PZTs convert displacement to a small output charge. A commonly accepted model of a PZT is a resistor and capacitor in parallel, with the majority of impedance contained in its capacitance.

Thus, circuits need to be built to amplify the output charge from the PZTs without sacrificing the PZT Signal to Noise Ratio. A common method (and that used for this system) is a current-mode charge amplifier which, upon initial view in Figure 5.8 below, looks eerily similar to a Trans-Impedance amplifier. The difference here is that the feedback components are chosen such that a low frequency corner is established for the system (V_o/Q_i), such that the gain over a wide range of frequencies is constant until the load induced by the PZT attenuates it.

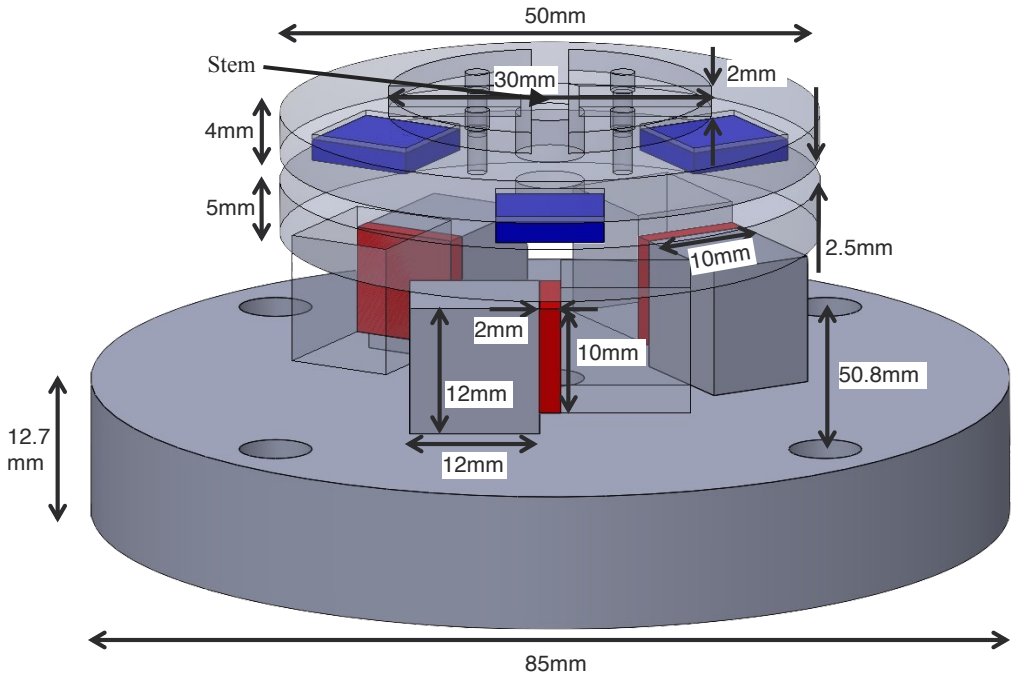

Figure 5.7: Solidworks rendition in an rotated side view of the F/T transducer made from aluminum (gray) which sandwiches the "Vertical" PZT (blue) and "Horizontal" PZT (red) layers. The top and middle aluminum layers are made transparent so the PZTs are visible. Transducer dimensions can also be seen.

Values for the resistors and capacitors of $R_i = 10\Omega$, $R_f = 10M\Omega$, and $C_f = 1nF$ are chosen such that there is a healthy system gain, which is inversely proportional to C_f, the low frequency corner is established at $\omega_{low} = 15$Hz, and the high frequency corner can be roughly approximated using the PZT capacitance only.

To clarify, system identification of this amplifier is made using a Signal Analyzer to generate the system gains in the plot to the right in Figure 5.8 with and without a PZT as a load (not displayed) on the input current source for the charge amplifier.

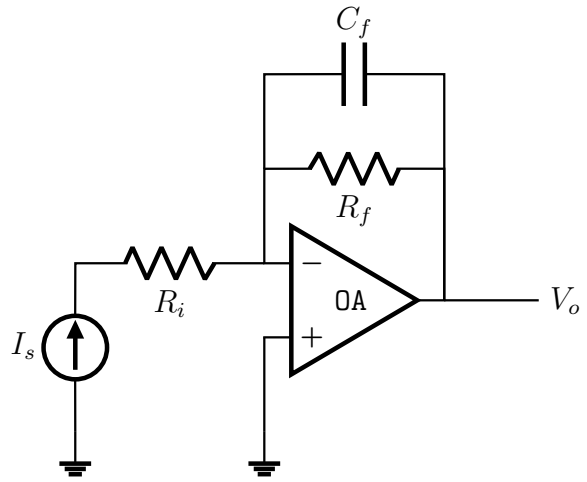

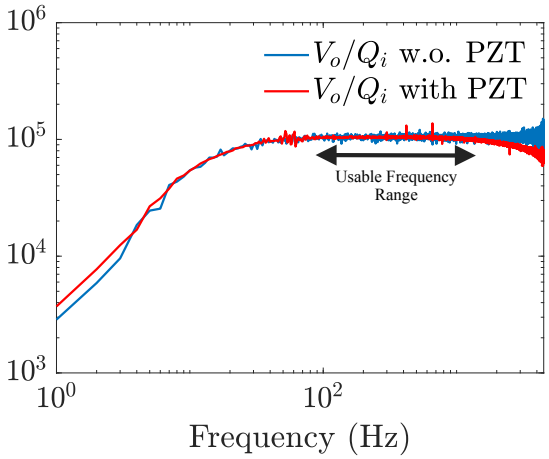

Figure 5.8: The charge amplifier (left) in current mode is shown with a current source. The frequency response magnitudes, V_o/Q_i (right) highlight the effect of the PZT in establishing the charge amplifier's high frequency corner. The amplification has constant gain roughly between 100 and 1000 Hz.

5.5 Calibration of F/T Transducer

After the F/T transducer is designed and built, it must be calibrated so there is knowledge as to how the imparted forces on the top of the transducer, at the interface of the resonator and transducer, are related to the PZT displacements in the transducer. That details of the calibration process are discussed.

5.5.1 Impact Hammer Forcing

Ideally the transducer calibration is achieved by mounting a calibration block on top of the transducer and applying known forces to the sides and tops of that plate. For this transducer and calibration block seen in Figure 5.9, the transducer is calibrated with ping tests, with impulsive forces applied via the PCB 086E80 hammer containing an internal force transducer. Its sensitivity of $\sim$ 100mV/lbf is quite suitable for the forces that can be applied to the transducer by hand.

Figure 5.10 indicates that the applied impulse in the time domain corresponds to a flat constant energy input spectrum in a reasonable frequency range, and representative

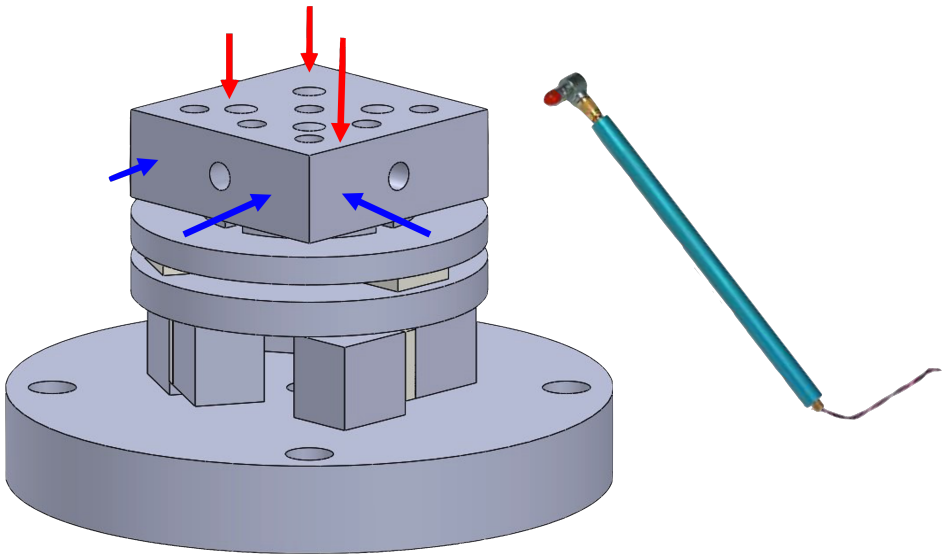

Figure 5.9: PZT based F/T transducer with PCB 086E80 Impact Hammer for use in calibration. At least six linearly independent location-wise impact tests are necessary to effectively calibrate the transducer. The large base with vibration isolation is not shown.

frequency responses in Figure 5.11 between PZTs and the input force are also shown to highlight the operable region of the transducer.

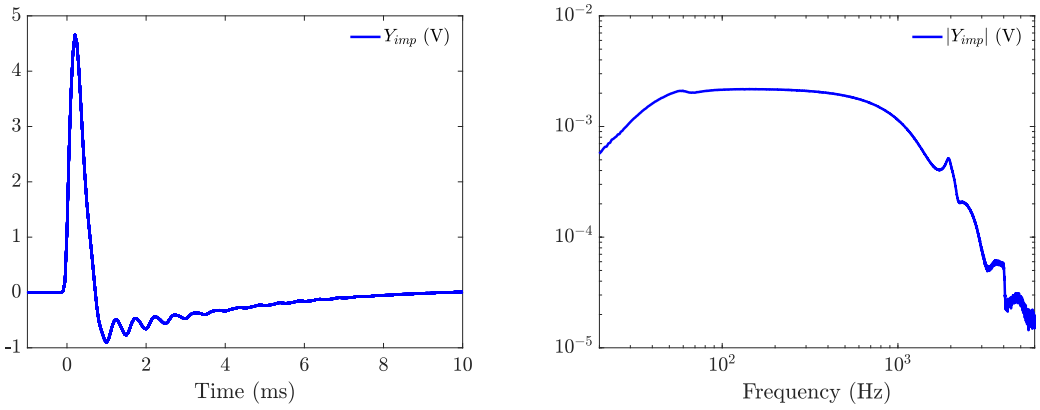

Figure 5.10: Time-Domain (left) and Magnitude (right) Spectrum of input ping at one side location from PCB 086E80 Impact Hammer internal force cell to highlight input energy into system

To obtain a full rank transformation matrix between the six PZT channels and the six forces and torques, at least six experiments are performed (and preferably more to better inform the transformation matrix), where the transducer is forced with known forces and torques such that the F/T vectors are linearly independent.

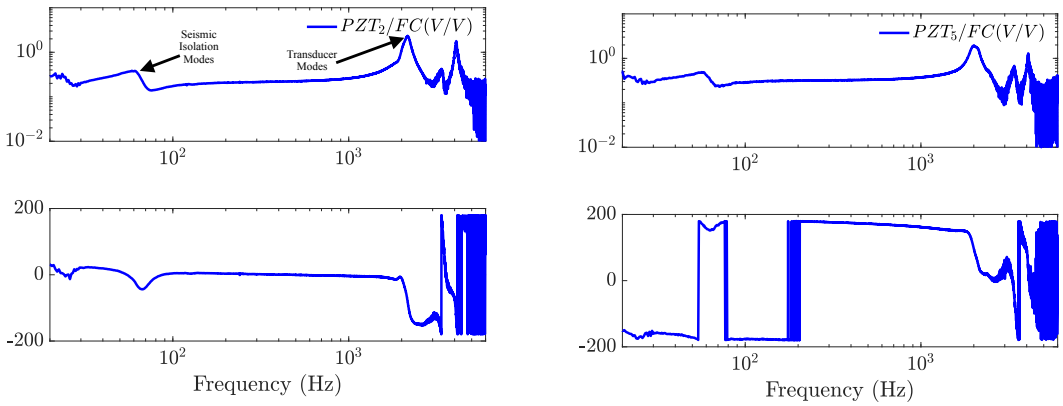

Figure 5.11: PZT to PCB Hammer Force Cell (FC) frequency responses from a representative PZTs showing a clear flat frequency region of operation for the isolated transducer in between the base vibration isolation modes at ∼40Hz and the lowest transducer modes at ∼2kHz.

Those force and moment components at the transducer mounting plate are deduced from kinematics, made clear in Figure 5.12, where the dimensions and forcing locations are shown for the isolated calibration plate.

Thus, the location and line-of-action of the applied solenoid force will be converted into a six element vector with elements $\{f_x, f_y, f_z, m_x, m_y, m_z\}$. The units of the first three elements are N, and the last three are N-m. Experiment p will yield the vector $v^{(p)} \in \mathbb{R}^6$ whose elements convert the solenoid force into $\{f_x, f_y, f_z, m_x, m_y, m_z\}$. This vector does not depend on frequency but is only applicable when the solenoid force frequency is sufficiently lower than the loaded transducer modal frequencies.

5.5.2 Obtaining Transformation between PZT voltages and Applied Forces and Torques

The frequency dependent transformation matrix $T(\omega) \in \mathbb{C}^{6x6}$ converts the PZT voltages into the transducer mounting plate forces and moments $\{f_x, f_y, f_z, m_x, m_y, m_z\}$. The units of the elements are N/V or N-m/V.

With these definitions in place the frequency dependent transducer plate forces and

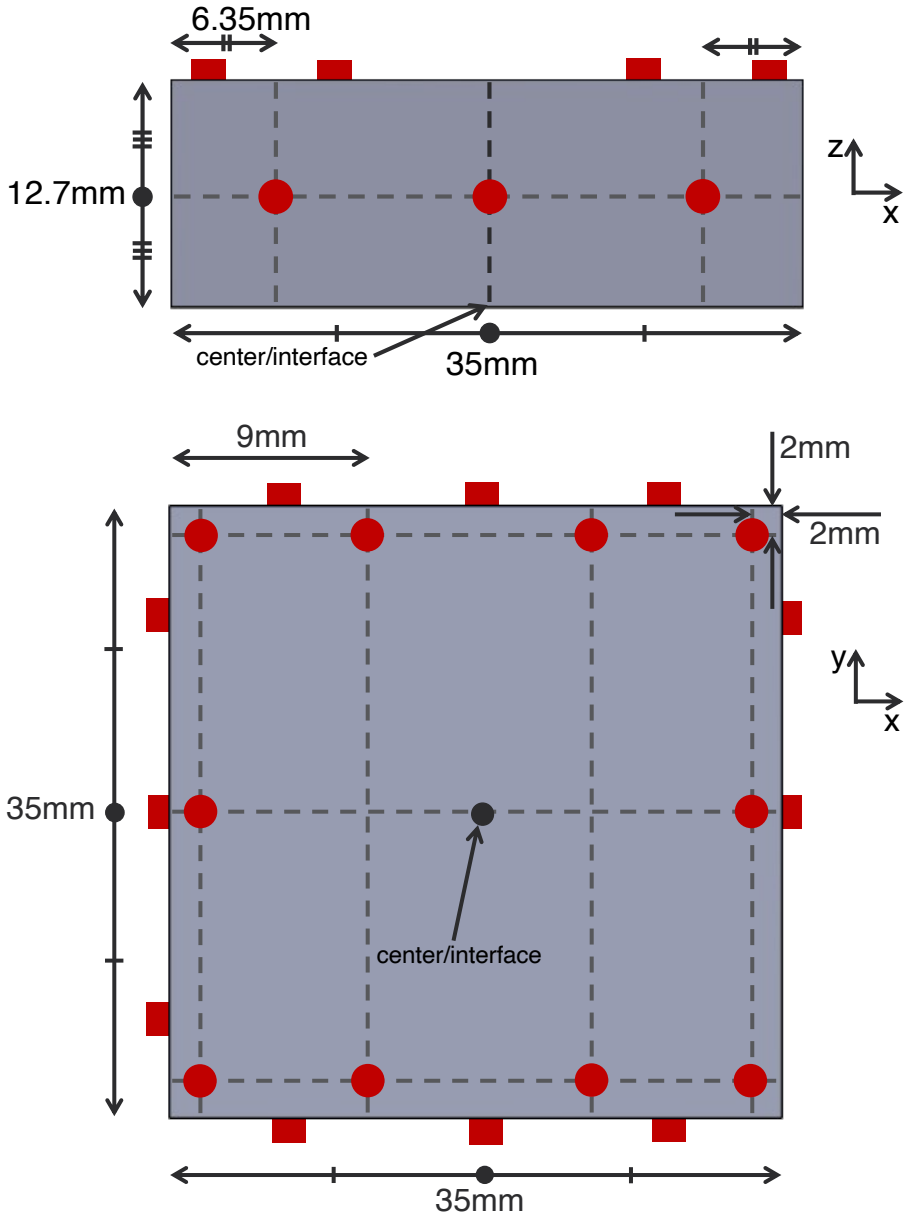

Figure 5.12: Side (left) and Top (right) views of the isolated calibration plate are shown. Applied force locations are shown in red. Kinematics are calculated using vector from force location to transducer center/interface and given plate dimensions. Series of dashes signify equal length segments.

moments as a function of the solenoid amplifier voltage for Experiment p are given by

$$\mathbf{v}^{(p)} K_{sf} H_F^{(p)}(\omega) \in \mathbb{C}^6. \tag{5.1}$$

These forces and moments as a function of solenoid input are also obtained by converting the PZT frequency responses,

$$T(\omega)H_S^{(p)}(\omega) = \mathbf{v}^{(p)}K_{sf}H_F^{(p)}(\omega). \tag{5.2}$$

If n experiments are conducted, then the results can be packed into

$$T\begin{bmatrix} H_S^{(1)} & H_S^{(2)} & \cdots & H_S^{(n)} \end{bmatrix} = \begin{bmatrix} \mathbf{v}^{(1)} & \mathbf{v}^{(2)} & \cdots & \mathbf{v}^{(n)} \end{bmatrix} \begin{bmatrix} K_{sf}H_F^{(1)} & 0 & \cdots & \\ 0 & K_{sf}H_F^{(2)} & & \\ \vdots & & \ddots & \\ & & & K_{sf}H_F^{(n)} \end{bmatrix}. \tag{5.3}$$

Multiplying on the right by the inverse of the diagonal $n \times n$ matrix yields (after factoring out K_{sf}):

$$T\begin{bmatrix} H_S^{(1)} & H_S^{(2)} & \cdots & H_S^{(n)} \end{bmatrix} \begin{bmatrix} 1/H_F^{(1)} & 0 & \cdots & \\ 0 & 1/H_F^{(2)} & & \\ \vdots & & \ddots & \\ & & & 1/H_F^{(n)} \end{bmatrix} = \begin{bmatrix} \mathbf{v}^{(1)} & \mathbf{v}^{(2)} & \cdots & \mathbf{v}^{(n)} \end{bmatrix} K_{sf}. \tag{5.4}$$

The left-hand side simplifies to

$$T\overbrace{\begin{bmatrix} H_S^{(1)}/H_F^{(1)} & H_S^{(2)}/H_F^{(2)} & \cdots & H_S^{(n)}/H_F^{(n)} \end{bmatrix}}^{\text{PZT vs. force cell frequency responses, } \mathbf{H}} = \underbrace{\begin{bmatrix} \mathbf{v}^{(1)} & \mathbf{v}^{(2)} & \cdots & \mathbf{v}^{(n)} \end{bmatrix}}_{\mathbf{V}} K_{sf}, \tag{5.5}$$

which is succinctly expressed as

$$T\mathbf{H} = \mathbf{V}K_{sf}. \tag{5.6}$$

From here, T is computed on a frequency-by-frequency basis,

$$T = K_{sf}\mathbf{V}\mathbf{H}^{*}(\mathbf{H}\mathbf{H}^{*})^{-1}. \tag{5.7}$$

5.5.3 Usable Range of F/T Transducer for Stem Reaction Measurements

There are a few initial issues with even considering using this F/T transducer for application with the macro scale steel resonator. As seen in Figure 5.11, the lowest transducer mode with calibration block on top is around 2 kHz. This is close enough to the resonator $n = 2$ vibration modes at about 1.6 kHz such that the transducer is not operating a pure stiffness regime, i.e. the frequency response is not flat anymore. Furthermore, putting the macro resonator on the transducer adds mass loading to the overall system and as such the lowest (loaded) transducer mode would decrease from its initial frequency.

5.6 Lightweight Tuning Fork and F/T Transducer Calibration

It is still necessary to show that the F/T transducer is effective in its operation when a resonator is mounted, which necessitates a lighter weight resonator with lower frequency modes, leading to the design and use of a lightweight steel tuning fork resonator to highlight that the full system can be effectively calibrated, i.e. the transducer can measure stem reactions. The design of the tuning fork and calibration of the transducer for use in detecting the stem reactions in the tuning fork are discussed.

5.6.1 Tuning Fork Design and Planar Tuning Fork Modes

The equation for the tuning fork mode as formulated using conventional Beam theory in [HBW99] is

$$f_{TF} = \frac{N}{2\pi L^2}\sqrt{\frac{EI}{\rho A}},$$

where $N \approx 3.516$ arises from the boundary conditions associated with the cantilevered nature of the tines, L is the tine length, E is the Young's modulus of the steel comprising the tines, I is the moment of inertia of the rectangular tine cross section, ρ is the tine material density, and A is the tine cross sectional area. Because the prongs are designed with a rectangular cross-section, $I/A = a^2/12$, where a is the tine cross-section width, and thus,

$$f_{TF} = \frac{3.516}{2\pi L^2}\sqrt{\frac{Ea^2}{12\rho}}, \tag{5.8}$$

To be well within the operating flat region of operating frequency for the F/T transducer, a tuning fork modal frequency of 400 Hz was chosen to design the tuning forks around. Additionally, the need for the tuning fork to be magnetic in order to easily study the effect of point mass magnet placement, meant that the tuning fork had to be steel. With this in mind, given a steel bar of cross-sectional width of 2 mm to be used to construct the tines, $\boxed{L = 63 \text{ mm}}$ is sufficient for the tuning fork mode to be close to 400 Hz.

Simulating the vibrational modes of this tuning fork design yields two modes near 400 Hz, the tuning fork mode and a side to side mode, visualized in Figure 5.13.

Both modes are present in a narrow frequency band around 400 Hz, however, the tuning fork mode is of interest for operation of the tuning fork as a resonator. Thus, although tests involving the tuning fork may yield two vibrational modes, the focus is purely on the tuning fork mode.

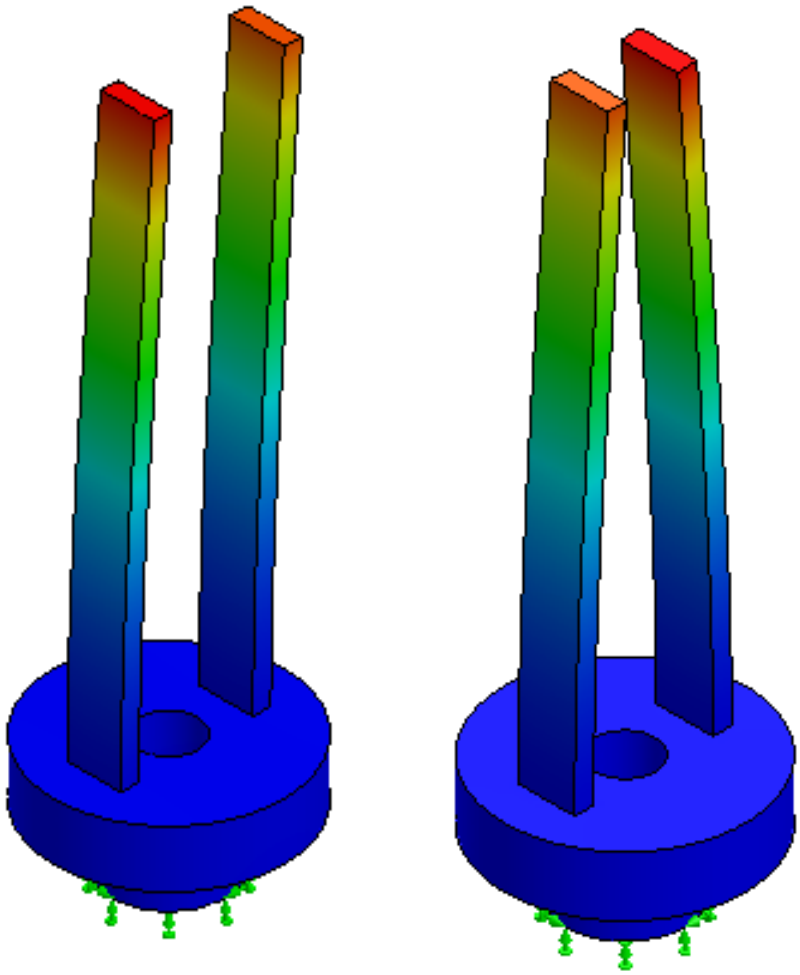

Figure 5.13: The tuning fork modes near 400 Hz for this tuning fork design. The steel tines are mounted on an aluminum base, and the green arrows represent the fixed boundary condition on the base. The side-to-side (left) mode has a mode-shape where the tines move in phase, whereas for the tuning fork (right) mode, the tines move in anti-phase

5.6.2 Calibration Results

With a new lightweight tuning fork, the F/T transducer is effective in detecting stem reactions. There is a need to calibrate with the tuning fork on the transducer, as there are mass loading effects that contribute to small but noticeable changes between reactions detected with and without the tuning fork on the transducer. Figures 5.14 and 5.15 contain diagrams of this setup used for calibration. For sake of brevity, the large metal base with pliable springs used for vibration isolation are not shown. Each figure shows representative

results for calibration ping tests performed from the side and top of the calibration block respectively.

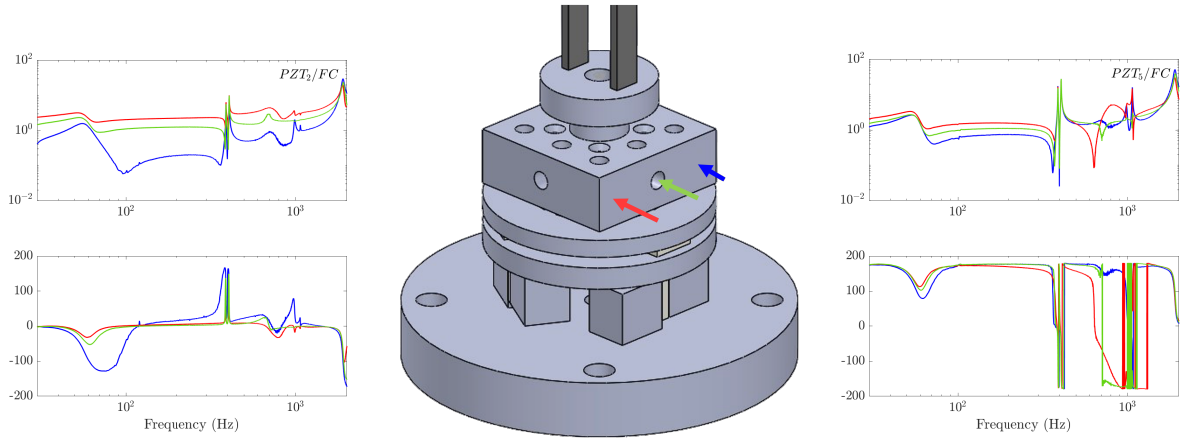

Figure 5.14: Representative diagram (center) of superposition check for horizontally applied forces. PZT-to-force frequency responses for horizontally (left) and vertically (right) facing PZTs.

It is expected that the average of the red and blue responses for all representative tests and PZTs average out to the result of the green response, and, although the responses are shown on a log-log scale, the response show this to be the case. Additionally, it is important to note that the tuning fork and side-to-side modes are visible near 400 Hz. Finally, a positive or negative sign (0° or 180° phase) in the flat region of the response is expected, which indicates the PZT's displacement in its primary direction of motion is compressive/expansive. The responses are fairly flat, so the frequency response for each PZT taken at 200 Hz informs the transformation for each ping test given the locations of applied forces relative to the center interfaces are known.

For some tests and PZT-to-force responses, the gain is very small and additionally the frequency response phase is far from 0° or 180°. If these small gain responses are used as is, the transformation distorts reactions predictions, however, the predictive power is improved if the PZT is assumed to act purely compressively/expansively. *In summary,* $\boldsymbol{H}$ *is computed for each test by projecting the response at a single frequency onto the real axis.*

The calibration procedure is completed at $n = 21$ different locations, as seen in Fig-

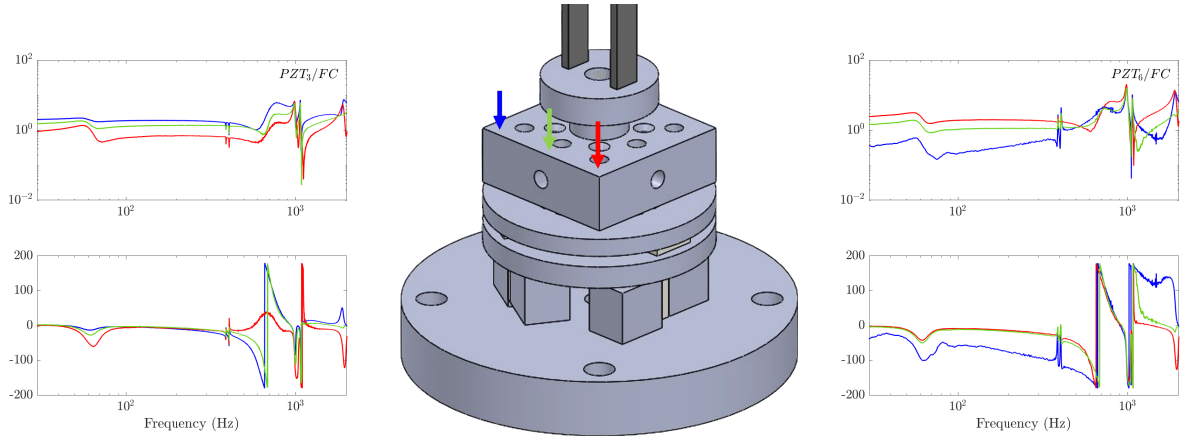

Figure 5.15: Representative diagram (center) of superposition check for vertically applied forces. PZT-to-force frequency responses for horizontally (left) and vertically (right) facing PZTs.

ure 5.12. At each location, a mount with a pliable spring turns the impact hammer into a pendulum such that the rubber tip strikes the same desired forcing location consistently. For the impact tests performed, Table 5.1 below highlights the six element vectors v_i for each test.

The vectors in this table are listed as rows, where each row corresponds to a different forcing location on the calibration block. This table yields matrix $\mathbf{V}$ with condition number

$$\boxed{\bar{\sigma}(\mathbf{V})/\underline{\sigma}(\mathbf{V}) = 2.69.}$$

Two checks ensure a properly accurate transformation after projecting the PZT-to-force-cell responses onto the real axis for each impact test location. First, the singular values of $\mathbf{H}$ are computed as a function of frequency, seen in Figure 5.16.

For the usable frequency region of the transducer, singular values are constant, and thus a condition number of the matrix $\mathbf{H}$ can be computed at a single frequency in this usable range to ensure minimal error in the computation of the transformation matrix T, i.e.

$$\boxed{\bar{\sigma}(\mathbf{H})/\underline{\sigma}(\mathbf{H}) = 3.83.}$$

Table 5.1: Associated force/torque reactions at stem for impact tests from kinematics. Each test yields a six element column vector. The first three elements show the direction and sign of the force, with line of action constrained to a single Cartesian axis. The last three elements yield the moment arms for each moment rectangular component.

$F_x(N/N)$	$F_y(N/N)$	$F_z(N/N)$	$M_x(cm\text{-}N/N)$	$M_y(cm\text{-}N/N)$	$M_z(cm\text{-}N/N)$
0	0	-1	-1.55	-1.55	0
0	0	-1	-1.55	-0.85	0
0	0	-1	-1.55	0.85	0
0	0	-1	-1.55	1.55	0
0	0	-1	0	-1.55	0
0	0	-1	0	1.55	0
0	0	-1	1.55	-1.55	0
0	0	-1	1.55	-0.85	0
0	0	-1	1.55	0.85	0
0	0	-1	1.55	1.55	0
0	1	0	-0.953	0	-1.133
0	1	0	-0.953	0	0
0	1	0	-0.953	0	1.133
-1	0	0	0	-0.953	0
-1	0	0	0	-0.953	1.133
0	-1	0	0.953	0	-1.133
0	-1	0	0.953	0	0
0	-1	0	0.953	0	1.133
1	0	0	0	0.953	-1.133
1	0	0	0	0.953	0
1	0	0	0	0.953	1.133

Second, once T is computed, the predictive power of the matrix is checked. The relative error between $\mathbf{V}$ and $T\mathbf{H}$ for all cases used for the calibration is checked, i.e.

$$\boxed{||\mathbf{V} - T\mathbf{H}||_2/||\mathbf{V}||_2 < 0.08,}$$

which is sufficient in terms of predictive power. With the calibration complete and the transformation matrix obtained, the F/T transducer can now be used to effectively measure stem reactions.

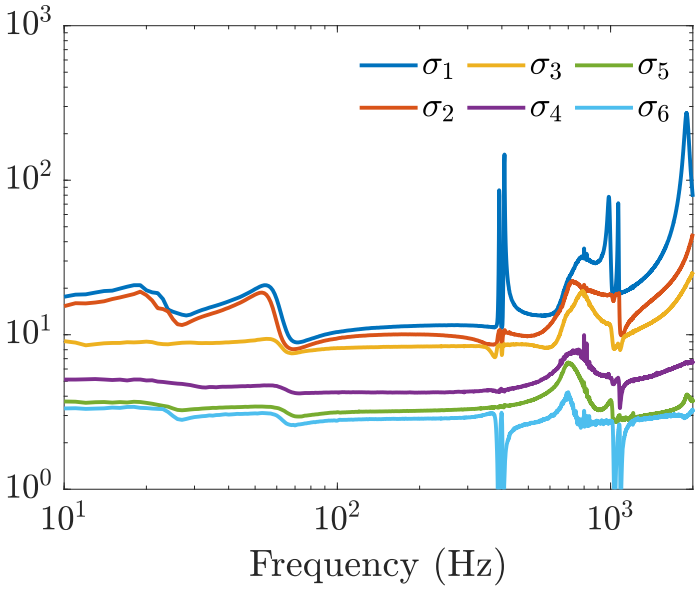

Figure 5.16: The singular values of **H** are plotted for the tuning fork/transducer setup. The usable frequency range for calibration is roughly between 100/,Hz and 300/,Hz. The condition number (σ_1/σ_6)in this usable frequency range is small. Base isolation modes and tuning fork modes are apparent.

5.7 Measuring Stem Reactions in Tuning Fork

With the F/T transducer, regardless of being calibrated or not, coupling coefficients between the transducer and resonator are computed. This section derives coupling coefficients for the full resonator/transducer system using the transient ring-down technique discussed in Chapter 3 and the observability Gramian.

Although the full system with the macro-scale resonator couldn't be calibrated, an ad-hoc study is performed in which masses are added to the resonator. Coupling coefficients between the resonator and the individual PZTs are computed for the nominal and mass perturbed states of the system.

With the F/T calibration achieved for the tuning fork system, coupling coefficients can be computed between the tuning fork resonator and the transducer reactions obtained using the calibration transform matrix. In essence, for both systems the energy associated with each PZT or stem reaction is normalized by the energy contained in the motion of the resonator,

standardizing the notion of a "coupling coefficient".

5.7.1 Obtaining Stem Reaction Coupling Coefficients with the Observability Gramian

For the full coupled resonator/transducer system, a transient ring-down test local to a pair of vibrational modes yields a discrete-time state space model, denoted by the triplet $\{A, x_o, C\}$, as seen previously in Chapter 3. In order to obtain coupling coefficients for each vibrational mode in the pair, the model is transformed such that the dynamic matrix A is now block diagonal, i.e. each mode has an A matrix expressed such that the state space model can be decoupled into two models for each mode. More specifically, there exists a transformation T, such that

$$\tilde{A} = T^{-1}AT = \begin{bmatrix} \tilde{A}_1 & 0 \\ 0 & \tilde{A}_2 \end{bmatrix} \in \mathbb{R}^{4x4},\ \tilde{C} = \begin{bmatrix} \tilde{C}_1 \\ \tilde{C}_2 \end{bmatrix},\ \tilde{x}_0 = \begin{bmatrix} \tilde{x}_{0,1} & \tilde{x}_{0,2} \end{bmatrix}. \tag{5.9}$$

In the transformed coordinates, coupling coefficients are calculated by first computing signal energies contained in the transients from each PZT pick-off channel and from the vibrometer pick-off for each mode using the controllability Gramian as seen below.

$$\tilde{A}_i G_{i,j} - G_{i,j} = -\tilde{C}_{i,j}^T \tilde{C}_{i,j}, \tag{5.10}$$

$$||y_{i,j}||_2^2 = \tilde{x}_{0,i,j}^T G_{i,j} \tilde{x}_{0,i,j}, \quad i = 1, 2; \quad j = 1, \ldots, 6, \tag{5.11}$$

where N is the number of total pick-offs in the combined systems, where the first six signal energies are associated with either the PZTs or stem reactions respective to the full resonator/transducer systems discussed below.

For the **tuning fork/transducer system**, the laser vibrometer is the single resonator pick-off, so the computation proceeds as follows: The resonator pick-off energy is computed

as

$$\tilde{A}_i G_{i,res} - G_{i,res} = -\tilde{C}_{i,res}^T \tilde{C}_{i,res}, \tag{5.12}$$

$$||y_{i,res}||_2^2 = \tilde{x}_{0,i,res}^T G_{i,res} \tilde{x}_{0,res}, \quad i = 1, 2. \tag{5.13}$$

The resonator pick-off energy is computed first using Equation 5.12. For this system, $\tilde{C}_{i,res}$ and $\tilde{x}_{0,i,res}$ are the constant coefficients C and x_0 associated with the vibrometer for the i^{th} vibrational mode. The PZT signal energies are then normalized by the this vibrometer energy using Equation 5.14, yielding coupling coefficients for each PZT and each vibrational mode. To reiterate the transformed PZT signals take the stem reaction sextuplet $\{f_x, f_y, f_z, m_x, m_y, m_z\}$. For instance y_{1,rxn_2} corresponds to the transient associated with the f_y reaction for the 1st vibrational mode.

$$||y_{i,pzt_k}||_2^2 = ||y_{i,k}||_2^2 / ||y_{i,res}||_2^2, \quad i = 1, 2; \quad k = 1, \ldots, 6 \tag{5.14}$$

5.8 Results of Transient Ring-down Modeling for TF Setup

5.8.1 Tuning Fork/Transducer Experimental Setup

The full tuning fork/transducer setup is below. A solenoid actuator operates as a single input, a vibrometer is the single resonator pick-off, and the transducer contains six PZT pick-offs.

A 5 second burst chirp actuates the tine in a roughly small bandwidth about 400 Hz, close to the tuning fork modal frequency. The input sent to the solenoid actuator and the resulting vibrometer are shown for the nominal state of the tuning fork. The significant beating in the pick-off data for the nominal system is indicative of the significant coupling present in both the side-to-side and tuning fork modes, however, in the perturbed system the beating is diminished in the reactions but remains in the vibrometer pick-off, indicating

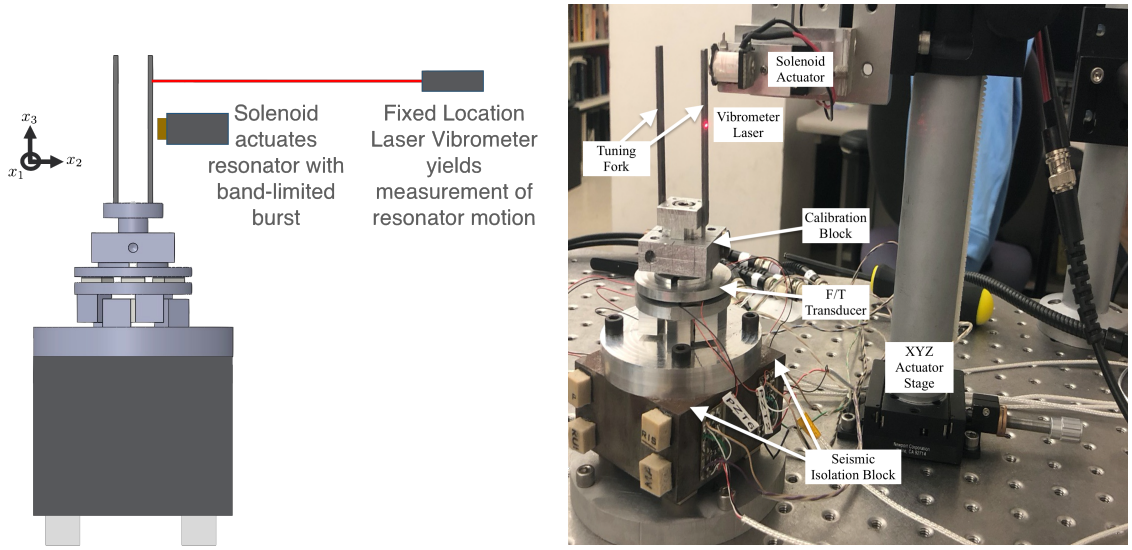

Figure 5.17: Tuning Fork/Transducer Experimental Setup Diagram (left) and Snapshot (right). The laser vibrometer remains in a fixed location for all experiments, and the solenoid pings the tuning fork. A solid block of steel with epoxied erasers as pliable springs act as a vibration isolation from the surface the entire system is sitting on. In the snapshot, proto-boards contain PZT charge amplifiers.

that the coupling has been reduced in one of the vibratory modes, which ends up being the tuning fork mode.

From these time-domain plots, a portion of the transient data is used to fit a system model, which is then used to calculate coupling coefficients, the results of which are seen in Table 5.2. The dominant F_y and M_z are highlighted in red to show the significant coupling decrease in the system. The mass perturbed tuning fork's time constant is longer as an effect of this decreased coupling.

Table 5.2: Coupling Coefficients for Transducer Reactions in Nominal and Mass Perturbed Tuning Fork

Force/Torque (F/T) Reactions	Nominal System Coupling Coefficients	Perturbed System F/T Coupling Coefficients
$F_x\,(N/V)^2$	0.0196	2.45e-5
$F_y\,(N/V)^2$	0.15	1.65e-4
$F_z\,(N/V)^2$	0.0053	6.57e-6
$M_x\,(N\text{-}cm/V)^2$	5.871	6.028e-3
$M_y\,(N\text{-}cm/V)^2$	0.0146	9.49e-7
$M_z\,(N\text{-}cm/V)^2$	0.0032	5.87e-6

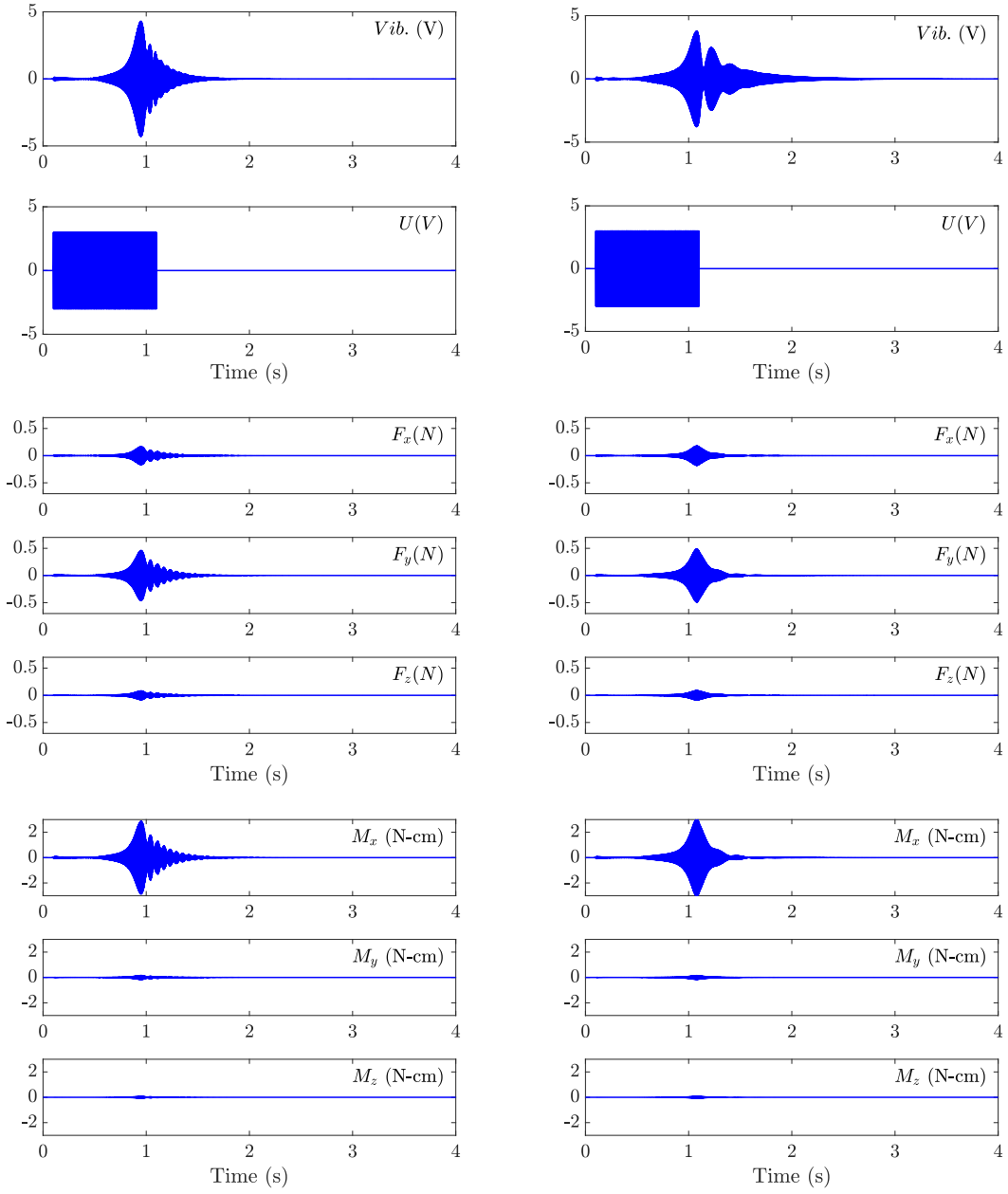

Figure 5.18: Time Domain plots of vibrometer output, input burst, and reaction forces and torques for nominal (left) and mass perturbed (right) cases. For both states of the tuning fork, F_y and M_z are unsurprisingly the dominant stem reactions detected by the transducer. Both the side-to-side and tuning fork modes are apparent.

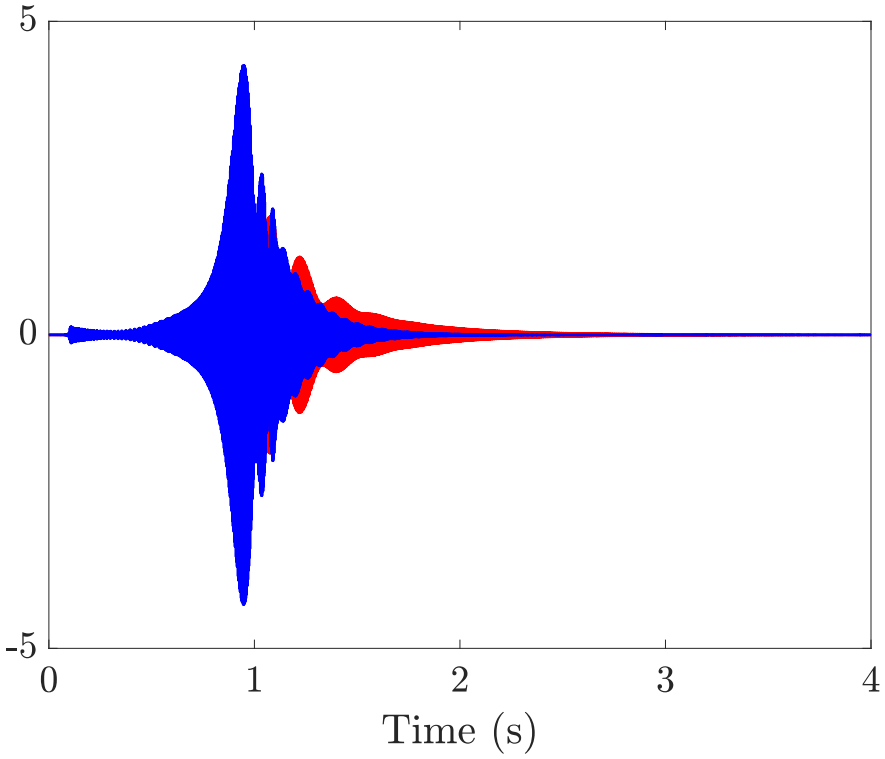

Figure 5.19: Enlarged time-domain plot of vibrometer responses for nominal (blue), where $\sigma = 0.18s^{-1}$, and mass perturbed (red), where $\sigma = 0.34s^{-1}$, tuning fork. The longer time constant, i.e. less motional damping, is quite apparent.

5.9 Ring-down Models for Macro-DRG

5.9.1 Coupling Coefficients

For the **steel macro ring-resonator/transducer system**, there are two resonator pick-offs. The computation proceeds as follows after applying Equation 5.10. The resonator pick-off energy is computed using Equation 5.12, however, $\tilde{C}_{i,res}$ and $\tilde{x}_{0,i,res}$ are now the block C and x_0 matrices associated with two resonator pick-offs for the i^{th} vibrational mode. The PZT signal energies are then normalized by this resonator pick-off energy yielding coupling coefficients for each PZT and vibrational mode using Equation 5.14.

5.9.2 Experimental Setup

The experimental setup is almost identical to that described in [SKM09] in that the same solenoid forcers and brass capacitive pick-offs are used to actuate and sense motion respectively in the steel ring resonator, however, the transducer is mounted underneath the resonator providing six additional pick-offs corresponding to PZT output voltages, a scrambled version of the stem reactions. The experimental setup in Figure 5.20 shows the two forcers and two pick-offs in the resonator, ensuring both $n = 2$ vibrational modes are actuated and observation of each mode-shape in terms of its orientation and modal frequency.

5.9.3 Obtaining Point Mass Sensitivities

The effect of point masses on the coupling coefficients needs is measured. To ensure that the $n = 2$ frequency split remains for consistent coupling coefficient comparisons, pairs of one and two point masses are placed 45° apart. Single pair and dual pairs of point mass are placed in 15° increments around the outer layer of the steel resonator to quantify the point mass sensitivity on coupling coefficients for both vibrational modes, which in turn informs where to place point masses to balance both modes in the steel resonator. θ refers to the

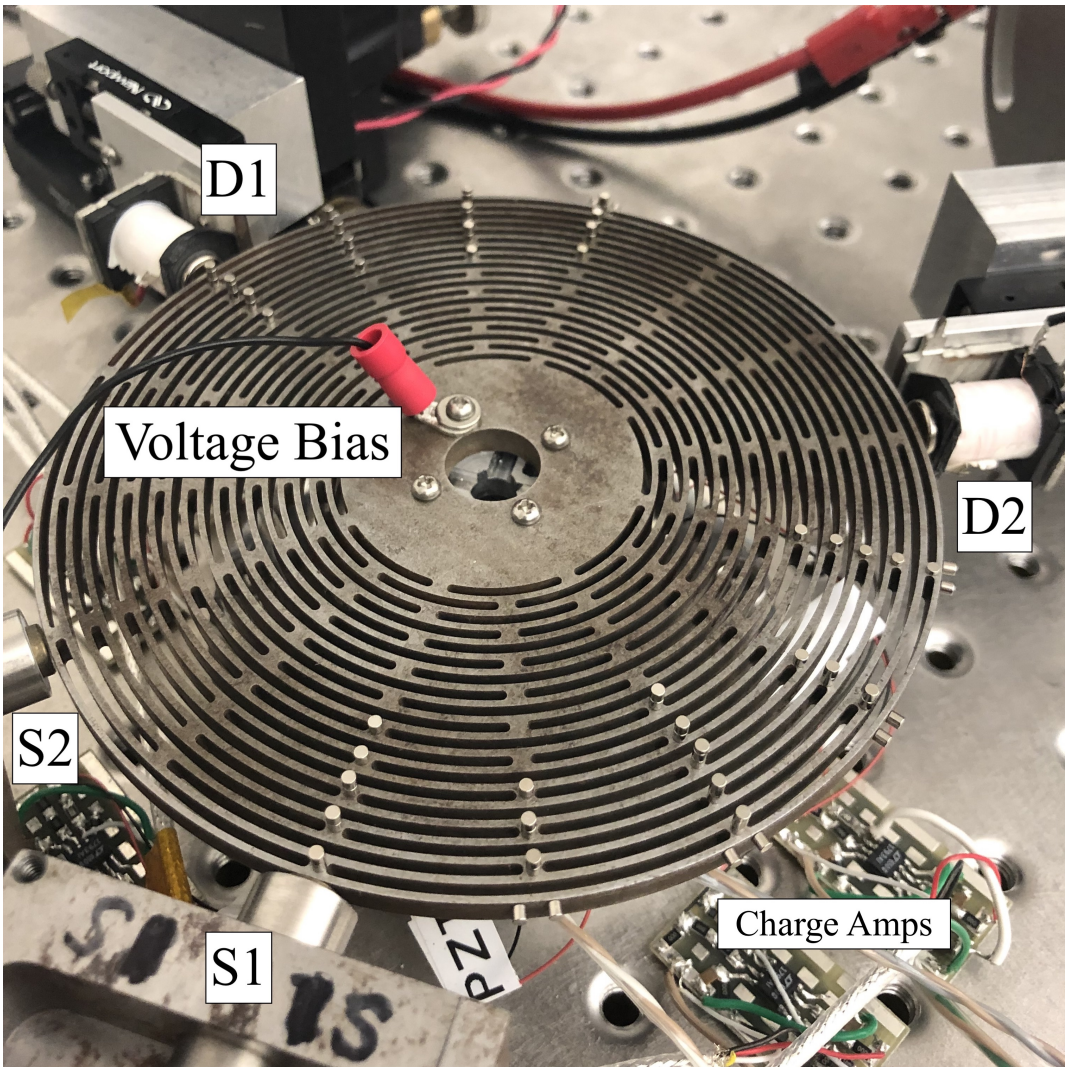

Figure 5.20: Experimental setup for transient tests with an 11.6 cm diameter steel Macro-DRG. Resonator forcers, labeled D_1 and D_2, are electromagnetic actuators, and resonator capacitive pick-offs, labeled S_1 and S_2, are used to measure radial deflection. A significant amount of small magnets are intentionally placed, creating reversible perturbations in the resonator mass distribution and thus reducing coupling between the resonator and transducer motion for both $n = 2$ vibratory modes. The resonator is mounted on top of the F/T transducer.

angle that is in between the pair of masses, and tables below show the results of these tests in terms of perturbations to coupling coefficients.

Table 5.3: Single and Dual Mass Pair Coupling Coefficient Sensitivities, Mode 1

θ, Pair Type	PZT_1	PZT_2	PZT_3	PZT_4	PZT_5	PZT_6
0°, single	1.643	0.254	-1.868	1.658	3.195	0.746
0°, dual	2.957	0.624	-3.406	2.682	6.369	1.541
45°, single	0.684	0.184	0.028	2.980	1.682	0.093
45°, dual	0.948	0.462	-0.016	5.842	3.420	0.145
90°, single	-1.462	0.202	1.747	4.240	0.293	-0.624
90°, dual	-3.028	0.519	3.638	8.813	0.498	-1.189
135°, single	-2.096	0.047	1.454	1.006	-0.960	-0.696
135°, dual	-4.000	0.123	3.372	2.398	-1.994	-1.318
180°, single	-1.671	-0.115	1.990	-1.823	-2.604	-0.700
180°, dual	-3.344	-0.114	4.146	-3.755	-4.817	-1.312
225°, single	0.355	-0.128	0.760	-2.427	-1.906	-0.012
225°, dual	0.571	-0.051	1.389	-4.895	-3.561	-0.053
270°, single	1.801	-0.120	-1.372	-3.594	-0.584	0.859
270°, dual	3.643	-0.097	-2.655	-6.879	-1.073	1.892
315°, single	1.487	0.010	-1.908	-1.537	1.147	0.800
315°, dual	2.888	0.029	-3.644	-3.084	2.477	1.749

Table 5.4: Single and Dual Mass Pair Coupling Coefficient Sensitivities, Mode 2

θ, Pair Type	PZT_1	PZT_2	PZT_3	PZT_4	PZT_5	PZT_6
0°, single	0.983	0.921	1.323	0.697	-0.059	1.518
0°, dual	1.934	1.800	2.662	1.580	-0.126	3.029
45°, single	2.390	-0.002	2.645	0.474	0.647	3.164
45°, dual	4.718	-0.151	5.595	1.010	1.508	6.406
90°, single	1.834	-0.761	1.154	-0.206	0.708	1.829
90°, dual	3.453	-1.559	2.403	-0.384	1.613	3.497
135°, single	0.097	-2.024	0.154	-0.695	0.862	0.032
135°, dual	0.364	-3.805	0.220	-1.053	2.012	0.165
180°, single	-1.419	-1.483	-0.629	-0.500	0.220	-1.509
180°, dual	-2.920	-2.880	-1.207	-0.846	0.449	-3.074
225°, single	-2.387	-0.106	-2.036	-0.270	-0.472	-3.136
225°, dual	-4.644	-0.231	-3.698	-0.488	-0.809	-6.033
270°, single	-1.066	1.458	-1.662	0.158	-0.606	-1.677
270°, dual	-2.102	2.963	-3.054	0.350	-0.955	-3.301
315°, single	0.019	2.375	-0.357	0.896	-0.629	0.053
315°, dual	0.031	4.941	-0.681	2.100	-0.977	0.090

5.9.4 Ad-Hoc Mass Balancing Results

The $n = 2$ modes are located near 1650 Hz and thus a 10 second burst chirp is applied to both inputs, each staggered relative to the other. Experimental results with and without mass perturbations intentionally placed to mass balance the structure are discussed. A transient data set, shown in Figure 5.21 is captured for all PZTs and resonator pick-offs to inform a full system state space mode from which coupling coefficients for each mode are extracted. This is repeated after 100 point masses are placed on the structure to reduce the coupling coefficients for each mode in all PZTs.

Because the setup with the steel resonator cannot be effectively calibrated, it is impossible to relate the PZTs to prescribed forces, and the coupling coefficients here are kept in terms units from the raw I/O data of $(V/V)^2$. The table and time domain plots highlight that a significant reduction in imbalance for both $n = 2$ vibrational modes can be achieved, however, a lot of point masses need to be placed because balancing the structure with regards to both modes simultaneously is extremely difficult, i.e. most placement locations increase the coupling coefficients in one mode while increasing that of the other mode.

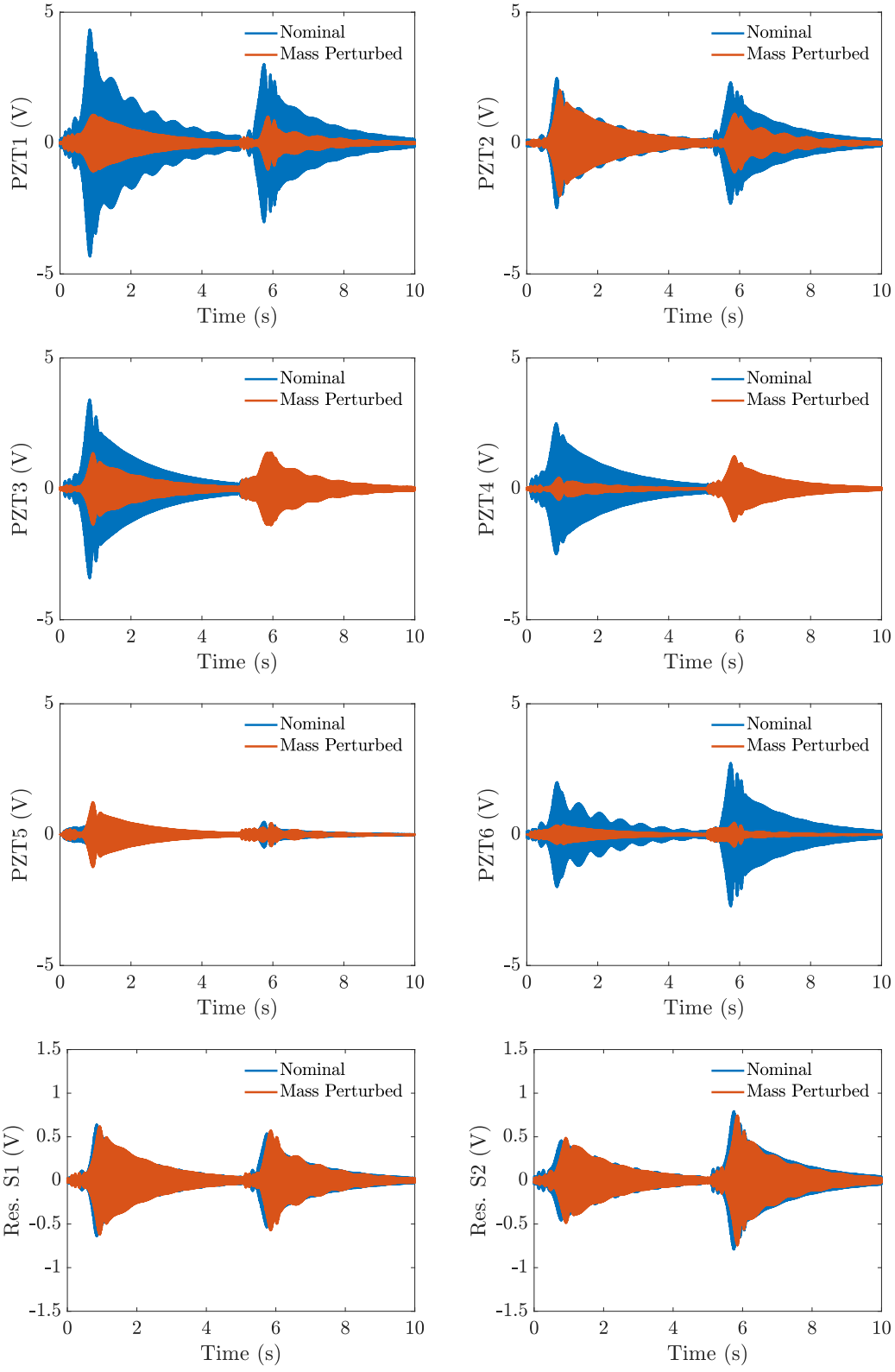

Figure 5.21: Pickoff voltages are shown with resonator pick-offs (bottom) having similar signal energy between nominal and mass perturbed tests. The reduction in system coupling is most apparent when looking at PZTs 1 and 6.

5.10 Conclusion

This chapter highlighted the use of a vibrometer to observe motion in a resonator die for its $n = 1$ and $n = 2$ modes, highlighting coupling between the motion of the MEM-DRG and its substrate. A PZT based, six DOF F/T transducer design is informed by a simple single axis coupled oscillator model, and characterizes reaction forces and moments that exist due to this coupling.

By using transient data to fit a Hankel based state model combined with computing specific observability Gramians for each pick-off, coupling coefficients are computed for a resonator vibrational mode pair.

Design and use of a lightweight tuning fork assists in yielding a full system where the transducer can be calibrated, and, as a result, the PZT responses can be unscrambled into stem reactions. Coupling coefficients are then quantified in the tuning fork mode for all 6 stem reactions. Intentionally applied masses to a single tine dramatically reduces this coupling and increases the time constant for this mode.

The transducer cannot be calibrated for the steel DRG, although an ad-hoc approach reduces these coupling coefficients in each PZT for both $n = 2$ modes simultaneously, albeit with significant mass loading.

CHAPTER 6

Conclusion

From the study of ring-type and tuning fork resonators in this thesis, the following remarks can be made as a summary.

- MEM-DRGs can be manufactured efficiently, however, small fabrication errors are introduced which break the symmetry of the structure. To recover the symmetry of the structure, post-fabrication processing is required, adding mass being the focus of this work.

- A model is developed for imperfect thin rings using the weak Galerkin method, a method suited for extracting mass and stiffness matrices for a vibrational system. First, mass and stiffness matrix perturbations local to a mode pair are computed, relative to small point mass and ring width perturbations. Second, these point mass perturbations yield changes to the ring center of mass, which motivates the need for the design and testing of a force-torque transducer for resonators to measure stem reaction forces.

- The DRG vibrational modes must first be identified. A transient based system identification method yields accurate models localized to a single mode pair. This model captures modal frequencies in the $n = 1$, $n = 2$, and $n = 3$ mode pairs precisely while simultaneously yielding orthogonal mode orientations. In a MEM-DRG with turned $n = 2$ modes, the model measures large changes in modal properties when small stiffness perturbations in the form of an electrostatic bias are applied.

- A zoom method for this model is also developed, which shifts the transient data to a base-band with decimation and a base-band modulation frequency, identifies a base-band model, and then shifts the base-band model to the frequency range of interest using that same modulation frequency. This method significantly reduces computational time for the modeling technique.

- A predictive model is developed for ring type resonators which includes stiffness and mass matrix components. A linear matrix inequality based optimization fits this model from the transient state space model developed for a nominal state of the resonator. The Galerkin based model for imperfect rings is extended to ring-like resonators. Experiments with single mass perturbations placed on multiple ring layers are completed, showing the predictive capabilities of the model. The model is quite effective for predicting the effect of single point masses on the outer ring layers, however, the effectiveness diminishes when trying to predict the effect of multiple mass perturbations and/or of placing a point mass on an inner ring layer.

- The design, construction, and testing of a six DOF F/T transducer is first motivated by rudimentary experiments where a laser vibrometer measures base motion when resonator vibrational modes are actuated. The creation of a transducer on the micro scale is a huge technical challenge, so a transducer is made and tested on resonators at the macro scale.

- A simple 4 state, coupled oscillator system with a resonator, transducer, and vibration isolation base is analyzed informing relative stiffness and mass parameters in the transducer design.

- A PZT based F/T transducer is built which exhibits properties similar to those seen in the simple model, however, the usable frequency range of the transducer is limited as the lowest transducer mode is near 2 kHz.

- For a lightweight steel tuning fork with vibrational mode near 400 Hz, the transducer is calibrated using impact tests. Stem reactions are measured via the PZT pick-offs using a similar transient modeling approach. A laser vibrometer measures the tine motion.

- Coupling constants are computing using transients from the transducer and vibrometer via an observability Gramian approach. Coupling constants associated with the dominant stem reactions are decreased using intentionally placed point masses.

- For a macro steel DRG with two capacitive resonator pick-offs, where the $n = 2$ mode pair is located near 1.6 kHz, the transducer cannot be calibrated. Coupling constants between PZTs and resonator pick-offs are calculated using the same observability Gramian approach.

- An ad-hoc approach enables a significant decrease in coupling constants. Coupling constants are measured when individual point masses are placed around the DRG, informing placement of multiple point masses to decrease coupling for both $n = 2$ vibrational modes.

Bibliography

[ABS98] Scott G Adams, Fred M Bertsch, Kevin A Shaw, and Noel C Macdonald. "Independent Tuning of Linear and Nonlinear Stiffness Coefficients." Technical Report 2, 1998. 8

[App84] "Inertial Technology for the Future." Technical report, 1984. 2

[AW11] K. J. Åström and B. Wittenmark. *Computer Controlled Systems: Theory and Design*. Dover Publications, third edition, 2011. 29, 82

[BBC13] J. J. Bernstein, M. G. Bancu, E. H. Cook, M. V. Chaparala, W. A. Teynor, and M. S. Weinberg. "A MEMS diamond hemispherical resonator." *Journal of Micromechanics and Microengineering*, **23**(12), 2013. 1

[Beh18] Amir H. Behbahani. *Toward Perfection of Gyros! Modeling, Analysis, and Modification of Ring-Type Resonators*. PhD thesis, 2018. 13, 77

[BKS17] Amir H Behbahani, Dennis Kim, Philip Stupar, Jeffrey Denatale, and Robert T M'closkey. "Tailored etch profiles for wafer-level frequency tuning of axisymmetric resonators." *JOURNAL OF MICROELECTROMECHANICAL SYSTEMS*, **26**(2):10, 2017. 3, 5, 37, 42

[BM17] Amir H. Behbahani and Robert T. M'Closkey. "Frequency analysis of a uniform ring perturbed by point masses and springs." *Journal of Sound and Vibration*, **397**:204–221, jun 2017. 3, 10

[BM19] Amir H. Behbahani and Robert T. M'Closkey. "Multimodal Tuning of an Axisymmetric Resonator." *Journal of Dynamic Systems, Measurement and Control, Transactions of the ASME*, **141**(9), sep 2019. 3, 10, 27, 73, 77, 78, 80

[Bro90] J. T. Broch. *Principles of Experimental Frequency Analysis*. Springer, Dordrecht, 1990. 64

[CFH94] C Cabuz, K Fukatsu, H Hashmoto, S Shoji, T Kurabayashi, K Minami, and M Esashi. "FINE FREQUENCY TUNING IN RESONANT SENSORS." In *Proceedings IEEE Micro Electro Mechanical Systems An Investigation of Micro Structures, Sensors, Actuators, Machines and Robotic Systems*, p. 6, 1994. 8

[CGL14] Anthony D Challoner, Howard H Ge, and John Y Liu. "Boeing Disc Resonator Gyroscope." Technical report, 2014. 1, 3

[Fox90] C H J Fox. "A SIMPLE THEORY FOR THE ANALYSIS AND CORRECTION OF FREQUENCY SPLITTING IN SLIGHTLY IMPERFECT RINGS." Technical Report 2, 1990. 2, 5

[GBG18] Howard H. Ge, Amir H. Behbahani, James Steve Gibson, and Robert T. M'Closkey. "Adaptive Cancellation of Parasitic Coupling." *J. Microelectromech. Sys.*, **27**(5):844–853, 2018. 32

[HBW99] Seon Han, Haym Benaroya, and Timothy Wei. "DYNAMICS OF TRANSVERSELY VIBRATING BEAMS USING FOUR ENGINEERING THEORIES." *Journal of Sound and Vibration*, **225**:935–988, 1999. 117

[HK66] B. Ho and R. Kalman. "Efficient construction of linear state variable models from input/output functions." *Regelungstechnik*, **14**:545–548, 1966. 29

[Jon84] E. Jonckheere. "Principal component analysis of flexible systems–Open-loop case." *IEEE Transactions on Automatic Control*, **29**(12):1095–1097, December 1984. 56

[KBK15] Michael Kanik, Punnathat Bordeenithikasem, Dennis Kim, Nate Selden, Amish Desai, Robert M'Closkey, and Jan Schroers. "Metallic glass hemispherical shell resonators." *Journal of Microelectromechanical Systems*, **24**(1):19–28, 2015. 1

[KM06] Dong Joon Kim and Robert T. M'Closkey. "A systematic method for tuning the

dynamics of electrostatically actuated vibratory gyros." *IEEE Transactions on Control Systems Technology*, **14**(1):69–81, jan 2006. 8, 9, 27

[KM14] Dennis Kim and Robert M'Closkey. "A MEM vibratory gyro with mode-matching achieved by resonator mass loading." *Record - IEEE PLANS, Position Location and Navigation Symposium*, pp. 499–503, 2014. 10

[LC97] Ki Bang Lee and Young Ho Cho. "Frequency tuning of a laterally driven microresonator using an electrostatic comb array of linearly varied length." *International Conference on Solid-State Sensors and Actuators, Proceedings*, **1**:113–116, 1997. 8

[PHA03] Siavash Pourkamali, Akinori Hashimura, Reza Abdolvand, Gavin K. Ho, Ahmet Erbil, and Farrokh Ayazi. "High-Q single crystal silicon HARPSS capacitive beam resonators with self-aligned sub-100-nm transduction gaps." *Journal of Microelectromechanical Systems*, **12**(4):487–496, 2003. 8

[PZT11] Igor P. Prikhodko, Sergei A. Zotov, Alexander A. Trusov, and Andrei M. Shkel. "Microscale glass-blown three-dimensional spherical shell resonators." *Journal of Microelectromechanical Systems*, **20**(3):691–701, 2011. 1

[RMF01] A. K. Rourke, S. Mcwilliam, and C. H.J. Fox. "Multi-mode trimming of imperfect rings." *Journal of Sound and Vibration*, 2001. 3

[SKM09] David Schwartz, Dong Joon Kim, and Robert T. M'Closkey. "Frequency tuning of a disk resonator gyro via mass matrix perturbation." *Journal of Dynamic Systems, Measurement and Control, Transactions of the ASME*, **131**(6):1–12, nov 2009. 9, 27, 128

[SKS15] David Schwartz, Dennis Kim, Philip Stupar, Jeffrey DeNatale, and Robert T. M'Closkey. "2015_JMEMS_mass_tune." *JOURNAL OF MICROELECTROMECHANICAL SYSTEMS*, **24**(3):545–555, 2015. 3, 5, 10, 27, 42, 79

[SMG14] Peng Shao, Curtis L. Mayberry, Xin Gao, Vahid Tavassoli, and Farrokh Ayazi. "A polysilicon microhemispherical resonating gyroscope." *Journal of Microelectromechanical Systems*, **23**(4):762–764, 2014. 1

[TLI13] Toshiyuki. Tsuchiya, Gwo-Bin Lee, and Institute of Electrical and Electronics Engineers. "EPITAXIALLY-ENCAPSULATED POLYSILICON DISK RESONATOR GYROSCOPE." In *IEEE 26th International Conference on Micro Electro Mechanical Systems (MEMS 2013) : January 20-24, 2013, Taipei International Convention Center, Taipei, Taiwan*, pp. 625–628. IEEE, 2013. 2

[TPZ11] Alexander A. Trusov, Igor P. Prikhodko, Sergei A. Zotov, and Andrei M. Shkel. "Low-dissipation silicon tuning fork gyroscopes for rate and whole angle measurements." *IEEE Sensors Journal*, **11**(11):2763–2770, 2011. 1

[TSH14] P. Taheri-Tehrani, T. H. Su, A. Heidari, G. Jaramillo, C. Yang, S. Akhbari, H. Najar, S. Nitzan, D. Saito, L. Lin, and D. A. Horsley. "Micro-scale diamond hemispherical resonator gyroscope." *Technical Digest - Solid-State Sensors, Actuators, and Microsystems Workshop*, (April 2015):289–292, 2014. 1

[YM96] J J Yao and N C Macdonald. "A micromachined, single-crystal silicon, tunable resonator." Technical report, 1996. 8

[ZM74] H. Zeiger and A. McEwen. "Approximate linear realizations of given dimension via Ho's algorithm." *IEEE Trans. Autom. Control*, **19**(2):153–153, 1974. 31

[ZTS12] Sergei A. Zotov, Alexander A. Trusov, and Andrei M. Shkel. "Three-dimensional spherical shell resonator gyroscope fabricated using wafer-scale glassblowing." *Journal of Microelectromechanical Systems*, **21**(3):509–510, 2012. 1